
Electronic Theses and Dissertations, 2004-2019

2019

A Study of Organo-phosphorous Simulants Thermal Destruction Using Shock Tube/Laser Diagnostics Techniques and Chemical Kinetics Modeling

Sneha Neupane
University of Central Florida



Part of the [Mechanical Engineering Commons](#)

Find similar works at: <https://stars.library.ucf.edu/etd>

University of Central Florida Libraries <http://library.ucf.edu>

This Doctoral Dissertation (Open Access) is brought to you for free and open access by STARS. It has been accepted for inclusion in Electronic Theses and Dissertations, 2004-2019 by an authorized administrator of STARS. For more information, please contact STARS@ucf.edu.

STARS Citation

Neupane, Sneha, "A Study of Organo-phosphorous Simulants Thermal Destruction Using Shock Tube/Laser Diagnostics Techniques and Chemical Kinetics Modeling" (2019). *Electronic Theses and Dissertations, 2004-2019*. 6543.

<https://stars.library.ucf.edu/etd/6543>

A STUDY OF ORGANO-PHOSPHOROUS SIMULANTS THERMAL DESTRUCTION USING
SHOCK TUBE/LASER DIAGNOSTICS TECHNIQUES AND CHEMICAL KINETICS MODELING

by

SNEHA NEUPANE
M.S. Auburn University, 2015
B.S. Tribhuvan University, Institute of Engineering, 2006

A dissertation submitted in partial fulfillment of the requirements
for the degree of Doctor of Philosophy
in the Department of Mechanical and Aerospace Engineering
in the College of Engineering and Computer Science
at the University of Central Florida
Orlando, Florida

Summer Term
2019

Major Professor: Subith S. Vasu

© 2019 Sneha Neupane

ABSTRACT

High-fidelity chemical kinetic models are critical in predictive modeling during design and optimization of next generation energy systems. Shock tube provides an ideal tool to investigate high-temperature chemical kinetics. Non-intrusive laser absorption diagnostics provide in-situ measurements of quantitative, time-resolved species concentration data in this complex chemically reacting system. In this work, shock tube and laser absorption spectroscopy were utilized to measure species concentration time-histories during pyrolysis and oxidation of organo-phosphorous compounds (OPCs). The experiments data obtained were used as benchmark to develop an improved kinetic model of OPCs combustion.

Interest in combustion chemistry of OPCs is associated to their use as fire suppressants and as chemical weapons. Pyrolysis and oxidation of OPCs were carried out behind reflected shock wave and laser absorption spectroscopy utilizing quantum cascade laser at mid-IR wavelength region was used to measure time resolved intermediate CO concentration produced during the process. Utilizing the experiments data, an improved chemical kinetic model for combustion of an OPC – Triethyl Phosphate (TEP) was developed. Various steps taken to develop the improved model include: calculation of thermochemical properties; updating hydrocarbon kinetics; calculation of reaction rates and addition of alternative TEP decomposition pathways. The prediction of TEP combustion, in terms intermediate CO concentration yield during its pyrolysis and oxidation, made by the improved model is in much better agreement with the experiments. Such an accurate kinetic model is critical in predicting the effectiveness of OPCs as flame retardants when used as dopants in hydrocarbon fuels; and in devising counter weapon of mass destruction strategies to destroy chemical weapons.

To my mom and dad

ACKNOWLEDGMENTS

I would like to thank my advisor and mentor, Dr. Subith Vasu, for the guidance and assistance throughout my years of study. I am grateful to him for his willingness to take me on as a student, and his continuous support and motivation throughout my graduate studies. I also would like to thank to my dissertation committee members, Dr. Robert Peale, Dr. Louis Chow, and Dr. Alain Kassab for their willingness to be in my thesis committee, their time and effort to serve on my dissertation. I am thankful to Dr. Robert Peale for guiding me during FTIR experiments and to Dr. Artem Masunov for helping me with the quantum chemistry calculations of reaction rates. I learned a lot from them and I will be ever thankful for the opportunity to do research with them.

I am also grateful to Dr. William J. Pitz (LLNL), Dr. Mani Sarathy (KAUST) and Dr. Pierre-Alexandre Glaude (University of Lorraine) for feedback regarding chemical kinetic model development of TEP. I also thank Dr. Su Peiris (AFRL, Eglin FL) and Mr. Neeraj Sinha (CRAFT-TECH) for helpful comments and suggestions regarding the work. This work would not have been possible without the help of my many coworkers and friends in the Vasu Lab, both past and present. Finally, I would like to thank my family for their constant encouragement and support. My parents and sister have been a constant motivation throughout and I am very grateful to my husband Anup Thapa for his love, patience and support.

This project is sponsored by the Department of the Defense, Defense Threat Reduction Agency (grant number: HDTRA1-16-1-0009). The content of the information does not necessarily reflect the position or the policy of the federal government, and no official endorsement should be inferred.

TABLE OF CONTENTS

LIST OF FIGURES.....	ix
LIST OF TABLES.....	xiv
CHAPTER 1: INTRODUCTION.....	1
1.1 Motivation.....	1
CHAPTER 2: INFRARED ABSORPTION CROSS SECTIONS OF ORGANO-PHOSPHOROUS CHEMICAL-WEAPON SIMULANTS	4
2.1 Introduction.....	4
2.2 Methods.....	8
2.2.1 Experimental Setup	8
2.3 Data Analysis.....	11
2.4 Result and Discussion.....	15
2.5 Uncertainty Analysis.....	21
2.6 Conclusions.....	22
CHAPTER 3: SHOCK TUBE AND KINETIC MODELLING STUDY OF TRI-ETHYL PHOSPHATE (TEP).....	24
3.1 Introduction.....	24
3.2 Experimental Setup and Procedure.....	26
3.2.1 Shock Tube Facility	26
3.2.2 Fuel/oxidizer Mixture Preparation	27

3.2.3	CO Mole Fraction Measurements and Comparison with Model Prediction	28
3.3	Kinetic Modeling	29
3.4	Thermochemistry	32
3.5	Results and Discussions	34
3.6	Conclusions	43
CHAPTER 4: THEORETICAL CALCULATION OF REACTION RATES AND COMBUSTION KINETIC MODELING STUDY OF TRI-ETHYL PHOSPHATE (TEP).....		
		45
4.1	Introduction	45
4.2	Methods	50
4.2.1	Computational Methods	50
4.2.2	Chemical Kinetic Mechanism	51
4.2.3	Simulations	54
4.3	Results	55
4.3.1	Quantum Chemical and Kinetics Calculations	55
4.3.2	Comparison of Experimental Data in Literature with Model Predictions	59
4.3.2.1	CO Time-histories Measured in Shock Tube	59
4.3.2.2	Ignition Times Measured in Shock Tube	63
4.4	Effect of Addition of H-abstraction Pathway	68
4.5	Conclusions	73

CHAPTER 5: CO TIME-HISTORIES MEASUREMENTS DURING DMMP PYROLYSIS AND OXIDATION IN SHOCK TUBE.....	75
5.1 Introduction.....	75
5.2 Experimental methods.....	75
5.2.1 Fuel/oxidizer Mixture Preparation	78
5.2.2 Shock tube experiments	80
5.2.3 Laser absorption spectroscopy to measure CO concentration	82
5.3 Results and discussions.....	85
5.3.1 DMMP pyrolysis: CO concentration time-histories	85
5.3.2 DMMP oxidation: CO concentration time-histories	86
5.3.3 Comparison with model predictions	88
5.3.4 Sensitivity and reaction path analysis:	95
5.4 Conclusions.....	101
CHAPTER 6: SUMMARY.....	103
APPENDIX A: THERMODYNAMIC PROPERTIES OF PHOSPHOROUS SPECIES FROM CBS-QB3 CALCULATION.....	106
APPENDIX B: SPECIES DICTIONARY.....	108
LIST OF REFERENCES	112

LIST OF FIGURES

Figure 1-1: Molecular structure of OPC (Organo Phosphorous Compound) simulants and Sarin-GB.....	3
Figure 2-1: Absorption cross section (at STP) of major combustion products (C ₂ H ₄ and CH ₄) along with interfering species during decomposition of OPC. Cross section data are taken from PNNL's FTIR database [12].....	6
Figure 2-2: Schematic of FTIR experimental setup.....	9
Figure 2-3: Normalized absorbance plot taken over time for DMMP.....	12
Figure 2-4: Integrated absorbance vs time for DMMP in two different wavenumber range. The uncertainties in integrated absorbance based on the placement of baseline was less than 2.27%.14	
Figure 2-5: Cross section of Dodecane at 295 K and 1 atm: comparison between PNNL's results [12] and current study.....	15
Figure 2-6: Absorption cross section of OPC simulants in low frequency region (650-1500cm ⁻¹) at 295 K and 1 atm (broadening gas: N ₂).....	17
Figure 2-7: Absorption cross section of OPC simulants in high frequency region (2800-3100 cm ⁻¹) at 295 K and 1 atm (broadening gas: N ₂).....	18
Figure 3-1: Absorbance vs pressure plot for TEP test mixture showing a linear trend.....	28
Figure 3-2: TEP decomposition mechanism as suggested in Zegers and Fisher[33] and Glaude et. al.[35], showing six-center (Red) and four-center (blue) elimination reactions to eliminate C ₂ H ₄ and C ₂ H ₅ OH respectively.	31
Figure 3-3: CO formation pathway during pyrolysis and oxidation of TEP after 1μs test time using reaction path analyzer tool in Chemkin Pro.....	32

Figure 3-4: Measured CO time history during TEP pyrolysis and comparison with model predictions. For clarity, the CO mole fraction traces have been smoothed using 100 point moving average. 35

Figure 3-5: Measured CO time history during TEP oxidation and comparison with model predictions. For clarity, the CO mole fraction traces have been smoothed using 100 point moving average. 36

Figure 3-6: Sensitivity coefficients to CO formation showing top 10 most sensitive reactions during TEP pyrolysis. 37

Figure 3-7: Measured vs predicted CO yield during 0.25% TEP pyrolysis after decreasing the A-factor of Rxn.3 by two order of magnitude (to 2.5×10^{11}). 40

Figure 3-8: C₂H₅OH sensitivity coefficient during TEP pyrolysis at 1462 K and 1.473 atm using the improved model (model iii) 41

Figure 3-9: CO sensitivity coefficient during TEP oxidation at 1508 K and 1.17 atm using the improved model (model iii) 42

Figure 4-1: Triethyl phosphate (TEP)..... 45

Figure 4-2: Experiment and predicted CO time-histories during TEP pyrolysis and oxidation. **Solid line:** Experiments; **Dashed line:** LLNL OPC incineration mechanism with addition of TEP pyrolysis sub-mechanism from Glaude et. al [35]; **Dot line:** TEP mechanism proposed in our Chapter 2 [51]. 47

Figure 4-3: Sensitivity coefficients of important phosphorous reactions in TEP sub-mechanism. Sensitivity analysis was carried out for 0.25% TEP pyrolysis at 1462 K and 1.47 atm using TEP kinetic model from Neupane et al [51]. Only top phosphorous containing reactions are shown. 48

Figure 4-4: Reaction pathway for TEP consumption via molecular elimination and H-abstraction, radical decomposition and recombination reactions. Highlighted in red are molecular elimination reactions.	54
Figure 4-5: Structure of the Transition states for all reactions considered here. Dotted lines denote the chemical bonds being broken and formed, the bond lengths (\AA) are also shown.	57
Figure 4-6: Experimental and predicted CO yield during TEP pyrolysis (a-c) and oxidation (d-g)	60
Figure 4-7: CO sensitivity analysis for TEP pyrolysis (1462 K) and b. TEP oxidation (1213 K) using the proposed kinetic model.	61
Figure 4-8: ROP analysis of TEP oxidation at 1213 K.....	63
Figure 4-9: Ignition time calculation from predicted OH profile. OH profiles are simulated using proposed TEP mechanism showing two stage ignition	64
Figure 4-10: Ignition times comparison: experiments results by Mathieu et al (symbols) and model prediction (dashed lines)	65
Figure 4-11: Brute force sensitivity analysis (absolute) of important reactions to ignition times for a) first stage and b) second stage.....	67
Figure 4-12: Mole fraction vs time plot for important intermediates in TEP decomposition in a 0-D closed homogeneous reactor for a pyrolysis feed (0.1 mol% TEP and balance N_2) and a simplified feed containing 0.1 mol % TEP, 1 mol % each of O_2 , H, OH and balance N_2	70
Figure 4-13: Plots showing profiles of H- abstraction reaction products in the TEP decomposition pathway.	72

Figure 4-14: Plot showing the profiles of H, O ₂ and OH for 0-D closed homogenous reactor simulation for a mixture containing 0.1 mol % TEP, 1 mol % each of O ₂ , H, OH and balance N ₂	73
Figure 5-1: Plot of measured absorbance vs concentration-pathlength ‘burden’ of 0.1% DMMP/Ar mixture showing a linear trend.....	80
Figure 5-2: Absorption cross section of CO near 4.88μm and at 1500 K and 1.7 atm simulated using HITRAN database[39].	83
Figure 5-3: Measured pressure, P5 vs simulated pressure in Chemkin-Pro	84
Figure 5-4: CO formed during pyrolysis of 0.1% DMMP at the three temperatures indicated in the figure. P ~ 1.7 atm.....	85
Figure 5-5: CO formed during oxidation of 0.1% DMMP at different equivalence ratios.	88
Figure 5-6: Experiments vs. models: CO yield during pyrolysis of 0.1% DMMP pyrolysis	91
Figure 5-7: Experiments vs. models: CO yield during oxidation of DMMP $\phi=2$	92
Figure 5-8: Experiments vs. models: CO yield during oxidation of DMMP $\phi=1$	93
Figure 5-9: Experiments vs. models: CO yield during oxidation of DMMP $\phi=0.5$	94
Figure 5-10: Experiments vs. models: CO yield during oxidation of DMMP $\phi=0.23$	95
Figure 5-11: Sensitivity analysis on CO concentration yield during 0.1%DMMP pyrolysis 1405K (dashed lines) and 1619K (solid lines) showing top phosphorous reactions	97
Figure 5-12: ROP analysis on DMMP during its pyrolysis at 1619 K.....	98
Figure 5-13: Sensitivity analysis on CO concentration yield during 0.1%DMMP oxidation at $\Phi=0.5$ and 1352K (solid lines) and 1604K (dashed lines) showing top phosphorous reactions ..	99

Figure 5-14: Sensitivity analysis on CO concentration yield during 0.1%DMMP oxidation at

$\Phi=0.5$ at 1.5ms..... 100

LIST OF TABLES

Table 2-1: FTIR Spectrometer configuration	11
Table 2-2: Summary of important absorption bands, their position, and peak cross section	20
Table 2-3: Uncertainty in cross section measurements.....	22
Table 3-1: Dominant phosphorous reactions to CO mole fraction yield during TEP pyrolysis and their rates from LLNL's OPC incineration mechanism [35]	38
Table 4-1: TEP reactions chosen for CBS-QB3 analysis based on results of CO sensitivity analysis shown in Figure 4-3.	49
Table 4-2: Thermochemistry of new species calculated using group additivity method	53
Table 4-3: Experiments conditions – CO time-history measurement during TEP combustion in shock tube[51] from our prior work.....	55
Table 4-4: The Arrhenius expression for the rate constants calculated at CBS-QB3 level of theory (present work) and estimated by Glaude et. al.[35] Activation energy (Ea): kcal/mol.	58
Table 4-5: Comparison of reaction rates (CBS-QB3 calculations vs. Glaude et. al. estimation) at 1000, 1500 and 2000 K. Unit of k : R1 to R7 = s ⁻¹ ; R8 = cm ³ mol ⁻¹ s ⁻¹	59
Table 5-1: Experiments conditions (Pressures and Temperatures) during pyrolysis and oxidation of DMMP	82

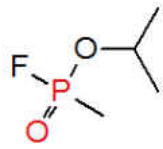
CHAPTER 1: INTRODUCTION

1.1 Motivation

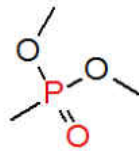
Design and optimization of successful counter weapon of mass destruction operation utilizing tailored explosives rely heavily on predictive capabilities of computational models. An enhanced understanding of decomposition pathways, reaction routes and associated kinetics at high temperature and high heating rate conditions will lead to better predictive capabilities of counter weapon of mass destruction strategies. Shock tubes are nearly ideal devices for studying gas-phase high-temperature chemical kinetics as they provide well-controlled step changes in temperature and pressure, a well-defined time zero, and for large diameter tubes, are generally not significantly affected by surface or transport phenomena. Laser-absorption-spectroscopy based diagnostic are non-intrusive, provide *in-situ* measurements (e.g., temperature and concentration of individual species including trace species) and have fast-time response (order of 1 to 10 microseconds). In this work, shock tube and laser absorption spectroscopy were utilized to measure species concentration time-histories during pyrolysis and oxidation of organo-phosphorous compounds (OPCs). The experiments data obtained were used as benchmark to develop an improved kinetic model of OPCs combustion.

Interest in combustion chemistry of OPCs is associated to their use as fire suppressants and as chemical weapons. Montreal protocol in 1990s prohibited the use of halons as fire suppressants due to their damaging effect on ozone layer[1]. Since then phosphorous containing compounds such as dimethyl methyl phosphonate (DMMP) and tri-methyl phosphate (TMP) have been identified as replacements of halons in fire suppressants. When used in gas-phase as dopants, these

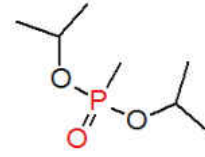
organo-phosphorous compounds (OPCs) interfere with normal combustion reactions to effectively reduce flame speed of hydrogen and hydrocarbon fuels[2]. OPCs are also used as chemical warfare (CW) agents such as Sarin, GB which is an extremely toxic nerve agent. Due to extreme toxicity of CW agents, experiments to study their combustion behavior are carried out using simulants. The chemical structures of simulants are similar to those of CW agents, and knowledge of their high temperature decomposition pathways is useful for predicting combustion behavior of CW agents. Figure 1-1(a) presents the molecular structure of sarin, and Figure 1-1(b) – (f) show the molecular structure of the five CW simulants. As seen in Figure 1-1, DMMP, DEMP and DIMP contain C-PO(OR)₂ group and are known as “alkyl phosphonate” compounds. On the other hand, TMP and TEP are “alkyl phosphate” compounds in which the center phosphorous atom is not directly bonded to a carbon atom. Hence, an accurate kinetic model of OPC simulants is critical in predicting their effectiveness as flame retardants when used as dopants in hydrocarbon fuels; and in devising counter weapon of mass destruction strategies to destroy chemical weapons.



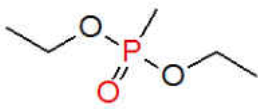
a. Sarin, GB



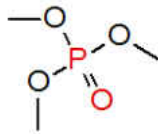
b. Dimethyl methyl phosphonate (DMMP)



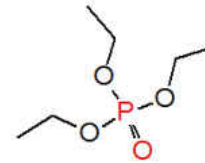
c. Diisopropyl methyl phosphonate (DIMP)



d. Diethyl methyl phosphonate (DEMP)



e. Trimethyl phosphate (TMP)



f. Triethyl phosphate (TEP)

Figure 1-1: Molecular structure of OPC (Organo Phosphorous Compound) simulants and Sarin-GB

CHAPTER 2: INFRARED ABSORPTION CROSS SECTIONS OF ORGANO-PHOSPHOROUS CHEMICAL-WEAPON SIMULANTS¹

2.1 Introduction

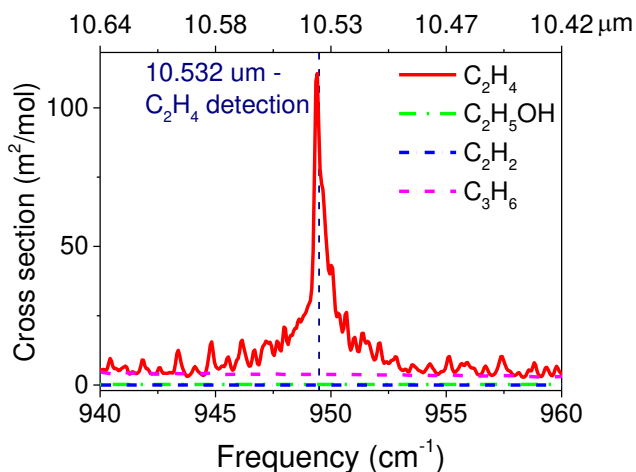
Incineration is effective at destroying chemical warfare (CW) agents, including G-agents (e.g., sarin - GB) and V-agents (e.g., VX), which are chemical weapons of mass destruction (WMD). Due to extreme toxicity of CW agents, experiments to study their combustion behavior are carried out using simulants [3]. The chemical structures of simulants are similar to those of CW agents, and knowledge of their high temperature decomposition pathways is useful for predicting combustion behavior of CW agents. Figure 1-1(a) presents the molecular structure of sarin, and Figures 1-1 (b) – (f) show the molecular structure of the five CW simulants studied here. As seen in Figure 1-1, DMMP, DEMP and DIMP contain C-PO(OR)₂ group and are known as “alkyl phosphonate” compounds. On the other hand, TMP and TEP are “alkyl phosphate” compounds in which the center phosphorous atom is not directly bonded to a carbon atom. In this paper, quantitative absorption cross section of DMMP, TMP, TEP, DEMP and DIMP at 295 K and 1 atm (broadening gas: N₂) are reported in mid IR region (750-3500 cm⁻¹) using FTIR spectroscopy.

Shock tube and laser diagnostics are promising tools for study and validation of chemical kinetics models. To measure species time histories during fuel breakdown at high temperatures (1000-2500 K) using laser absorption spectroscopy, accurate lines positions and absorption cross sections are required. For example, cross sections of common combustion products (C₂H₄, CH₄,

¹ Published in *Journal of Molecular Spectroscopy* 355 (2019): 59-65

CO₂, C₂H₅OH) at STP formed during decomposition of OPCs are plotted in the Figure 2-1(a and b), which also show laser wavelengths that have been utilized to measure C₂H₄ and CH₄ [4-6]. It has been reported in the literature that OPCs also have absorption feature within 9-11 μm and near 3.4 μm [7-10], which can interfere with C₂H₄ and CH₄ measurements, respectively. However due to lack of quantitative cross section data, the extent of interference from the parent compounds is unknown. To infer accurate intermediate products time histories, peak and valley method [5, 11] can be utilized if the differential cross section of interfering species is negligible at the chosen wavelengths pair. Similarly, to set up laser diagnostic scheme for OPCs detection in a shock tube, it is necessary to know the exact positions of absorption lines in their IR spectrum and cross sections. Although, high temperature cross section data are required to measure the decay of OPCs during a combustion process, knowledge on room temperature cross section provides a starting point during laser wavelength selection and diagnostics set up.

a.



b.

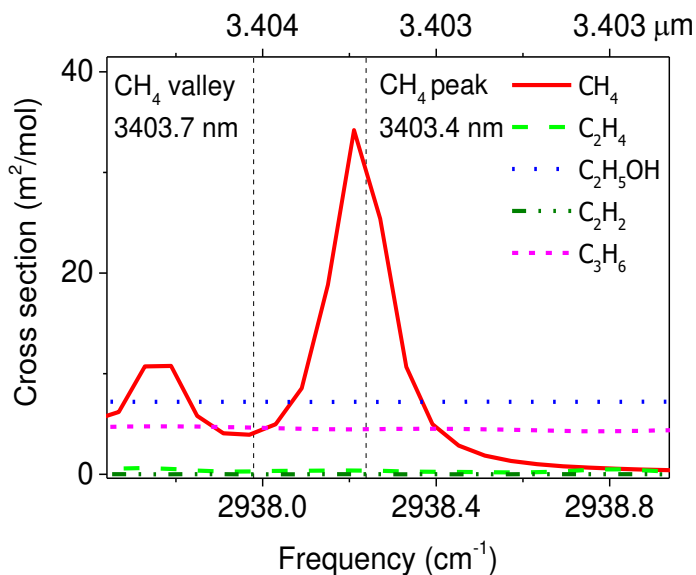


Figure 2-1: Absorption cross section (at STP) of major combustion products (C_2H_4 and CH_4) along with interfering species during decomposition of OPC. Cross section data are taken from PNNL's FTIR database [12]

There have been studies on absorption spectra of OPC simulants in the literature. DMMP (Dimethyl methyl phosphonate) is the most widely studied simulant of sarin and is also used as flame retardant. A number of studies have used FTIR spectroscopy to study its molecular structure

[13], assign its vibrational bands [14], and investigate its adsorption on different substrates [7-10]. TMP (Trimethyl phosphate) is also used as CW simulant. Its structure [15], vibrational bands [14] and adsorption [9, 16] have also been studied extensively using FTIR spectroscopy, and measured spectra have been compared to theoretical ab – initio calculated predictions [14, 17]. Cuisset et al [14] compared room temperature FTIR gas phase lines positions of DMMP, TMP, and TEP (Triethyl phosphate) measured at a resolution of 0.5cm^{-1} with numerical calculations within $50\text{-}5000\text{ cm}^{-1}$. They also report calculated line intensities (km/mol) for these compounds, however for experimental measurement only transmission spectra were reported, and no information is available on the cross-section data. Another study [13] from the same group extended their work to THz and far IR ($20\text{-}600\text{ cm}^{-1}$) regions to allow unambiguous discrimination between the different alkyl phosphonate and alkyl phosphate compounds. Fewer studies are available for larger OPCs like DEMP (Diethyl methyl phosphonate) [17] and DIMP (Diisopropyl methyl phosphonate) [17, 18]. Mott et. al. [17] used quantum chemistry method to simulate spectra of DEMP and DIMP and reported line positions of the prominent peaks in mid IR region ($400\text{-}3200\text{ cm}^{-1}$). Wilmsmeyer et. al. [18] measured gas phase absorption spectra of DIMP (at 298 K , resolution = 4 cm^{-1} , range = $700\text{-}4000\text{cm}^{-1}$) to study its adsorption in amorphous silica. Phillips and Taubman [19] reported cross section of DIMP (at 295 K and 1 atm) within $950\text{-}1050\text{ cm}^{-1}$. To the best of our knowledge, there is no information on quantitative absorption cross section of the remaining OPCs in the literature. In this chapter, quantitative absorption cross section of DMMP, TMP, TEP, DEMP and DIMP at 295 K and 1 atm (broadening gas: N_2) are reported in mid IR region ($750\text{-}3500\text{ cm}^{-1}$) using FTIR spectroscopy. The measurements are carried out at a resolution of 4cm^{-1} . In addition, different vibrational bands have been identified and compared with literature.

2.2 Methods

2.2.1 Experimental Setup

Transmittance spectra were collected using Bomem DA8 Fourier Transform Infrared spectrometer, which was described in our earlier work on oxygenated hydrocarbons [20]. The FTIR is equipped with IR light source (globar), KBr beam splitter, and HgCdTe (MCT) detector. The schematic of the setup is shown in Figure 2-2. The IR beam from the source, after being collimated, was modulated by a scanning Michelson interferometer. The modulated and collimated beam exited an external port of the spectrometer through a KBr window, where it was intercepted by a beam-folding flat mirror as shown in Figure 2-2. The beam then passed through a glass sample cell with heated anti-reflection-coated Ge windows. An off-axis paraboloid mirror converged the collimated beam to one focus of an off-axis ellipsoidal mirror. The MCT detector was placed at the other focus. Both flat and parabolic mirrors were mounted with push-pull screws that allowed complete alignment flexibility. The optical system was aligned initially using visible light source (quartz-halogen) and quartz beam splitter. A purge box with continuous flow of dry N₂ was used in between the external port of the spectrometer and the detector to obtain a slightly positive pressure within the beam path.

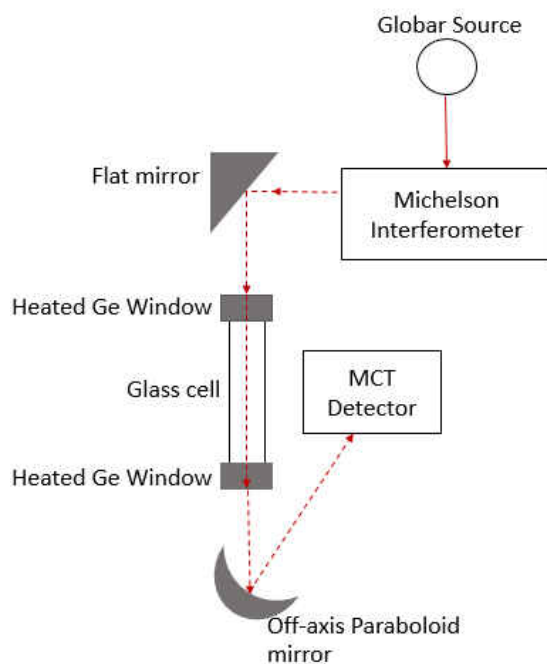


Figure 2-2: Schematic of FTIR experimental setup

Home-built vapor cells (path-lengths of 40.3 and 101.3 cm) were used. Research grade TMP, TEP, DEMP (purity ~ 99%), DMMP, and DIMP (purity ~ 96%) were purchased from Acros Organics. Approximately 0.5 ml of sample in an aluminum boat was placed at the center of the glass cell. The sample cell was closed at both ends with stainless steel flanges equipped with Ge-windows that provided airtight seal. To eliminate contamination from CO₂ and H₂O in ambient air, the cell was purged with dry N₂ for several minutes using fill ports in the stainless-steel flanges. The pressure was measured using a Baratron capacitance gauge (1000 Torr full-scale range) and was ~ 1 atm (758 ± 1 Torr). OPCs have low vapor pressure (<1 torr) at ambient temperature and tend to condense and stick to the wall of sample cell and the windows. To prevent condensation on the windows and to obtain a true gas-phase spectrum, the Ge-windows of the sample cell were heated above ambient to ~27°C using circumferential heaters. The temperature of windows and

flanges were monitored using an IR temperature sensor. The spectra reported in this paper were collected after the concentration of the analyte inside the cell reached a stable value, i.e. its vapor pressure at ambient condition, as determined by the stability of the spectra.

Each spectrum was calculated by Fourier transform of 1000 co-added interferograms. The measurements were taken in the spectral range of 400-4000 cm^{-1} , however due to limitation in Ge-windows and MCT detector, data below 650 cm^{-1} were not useful. To determine the resolution (defined as the inverse of mean optical path difference (MOPD) of the spectrometer [21]) required, measurements were taken at three unapodized resolutions, namely 4, 2, and 0.5 cm^{-1} . Each twofold improvement in resolution requires four-fold longer measurement time to obtain the same SNR. The spectra of the large OPC molecules comprises broad peaks at atmospheric pressure and ambient temperature, such that a resolution of 4 cm^{-1} sufficed to resolve all features. The integrated cross sections obtained using different resolution measurements were within the reported uncertainties. The accuracy of line peak positions is at least \pm half of resolution used in measurement ($\pm 2 \text{ cm}^{-1}$) and it can be improved by fitting the data points in the line to a standard line shape function. Cells of two different path-lengths were used for the measurements. The experimental conditions for different OPCs are summarized in Table 2-1. The reference spectrum was taken before putting the sample inside the cell, with all other parameters held same.

Table 2-1: FTIR Spectrometer configuration

FTIR spectrometer configuration	
Aperture	10mm
Resolution	4 cm ⁻¹
Optical path length	TMP, DMMP, DIMP: 43.18 cm
	TEP, DEMP: 101.3 cm
Apodization	Boxcar

2.3 Data Analysis

Spectral processing (baseline correction for offset and slope) was done using Origin 2016 software. A slight baseline offset and slope were present in spectra which shifted the baseline by a maximum of 0.04 absorbance units (from the zero value). This can be attributed to instrument drift caused by voltage and temperature fluctuations inside the instrument over the duration of measurement. To correct for the baseline offset and bring back the baseline to zero absorbance units, minimum absorbance in the spectrum was subtracted from absorbances at all the frequencies. To correct for baseline slope, a function that closely parallels the baseline of a spectrum was drawn and subtracted from the entire spectrum. The Beer-Lambert law given by Equation 2-1 was used to calculate the absorption cross section $\sigma_i(\nu, T)$ according to

$$\alpha_\nu = -\ln\left(\frac{I}{I_o}\right)_\nu = n_i \sigma_i(\nu, T)L = \frac{P_i}{R_u T} \sigma_i(\nu, T)L \quad (2-1)$$

In Eq. 1, α_ν is the absorbance at frequency ν , I and I_o are the spectral intensity of sample and reference measurements, respectively; n_i [mol/m³] is the concentration of absorbing species 'i'; σ [m²/mol] is the cross section, P_i [Pa] is the partial pressure of the analyte inside the cell; L

[m] is the length of the cell; R_u [J/mol-K] is the universal gas constant; T [K] is the temperature (295 K).

Due to nonlinearities associated with FTIR absorption measurement at low transmittance, ($T(v) = I/I_0 \leq 0.025$) [12], the optical depth was limited to $T(v) \geq 0.15$. To convert the σ [m²/mol] to conventional unit of cross section [cm²/mlc.],

$$\sigma \left[\frac{\text{m}^2}{\text{mol}} \right] = 6.022 \times 10^{-19} \times \sigma \left[\frac{\text{cm}^2}{\text{mlc.}} \right]$$

Spectra were collected immediately after the analyte was placed inside the cell and at subsequent times thereafter until the absorption strength stabilized. Figure 2-3 presents four sequential spectra for DMMP following sample insertion into the cell, with measurement time indicated. Each curve is offset by 0.2 absorbance units from the previous spectrum for clarity. These spectra are normalized to better compare their line shapes. The figure demonstrates that the spectral line shape does not depend on time.

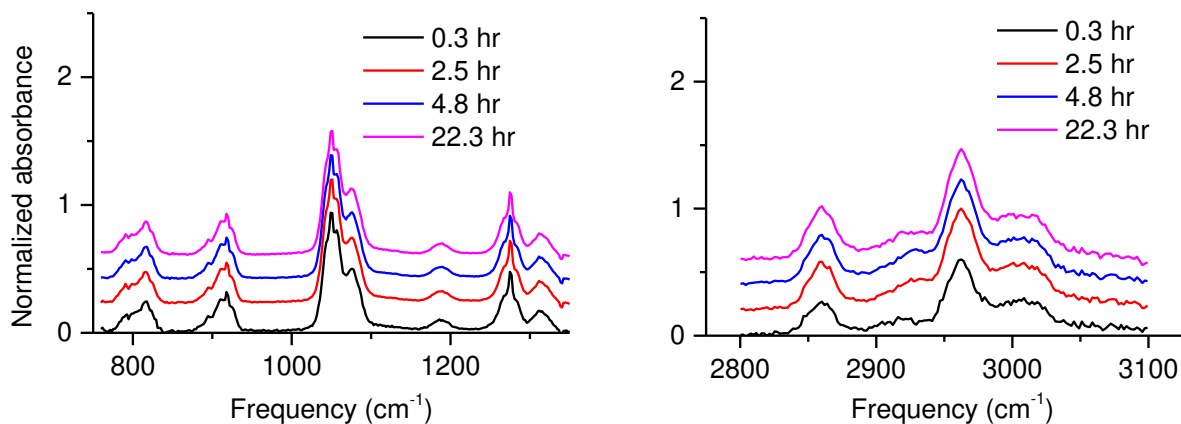


Figure 2-3: Normalized absorbance plot taken over time for DMMP

Figure 2-4 presents the integrated absorbance (of the un-normalized spectra) as a function of time. The time to obtain a stable spectrum varied within 2-5 hours depending on the vapor pressures of the OPCs, hence spectra were also taken for a time longer than 22 hours to verify saturation. The saturation vapor pressure at ambient temperature (295K) has the value [22-24] 89.29, 100, 44.47, 35.56 and 11.31 Pa for DMMP, TMP, DEMP, DIMP and TEP, respectively.

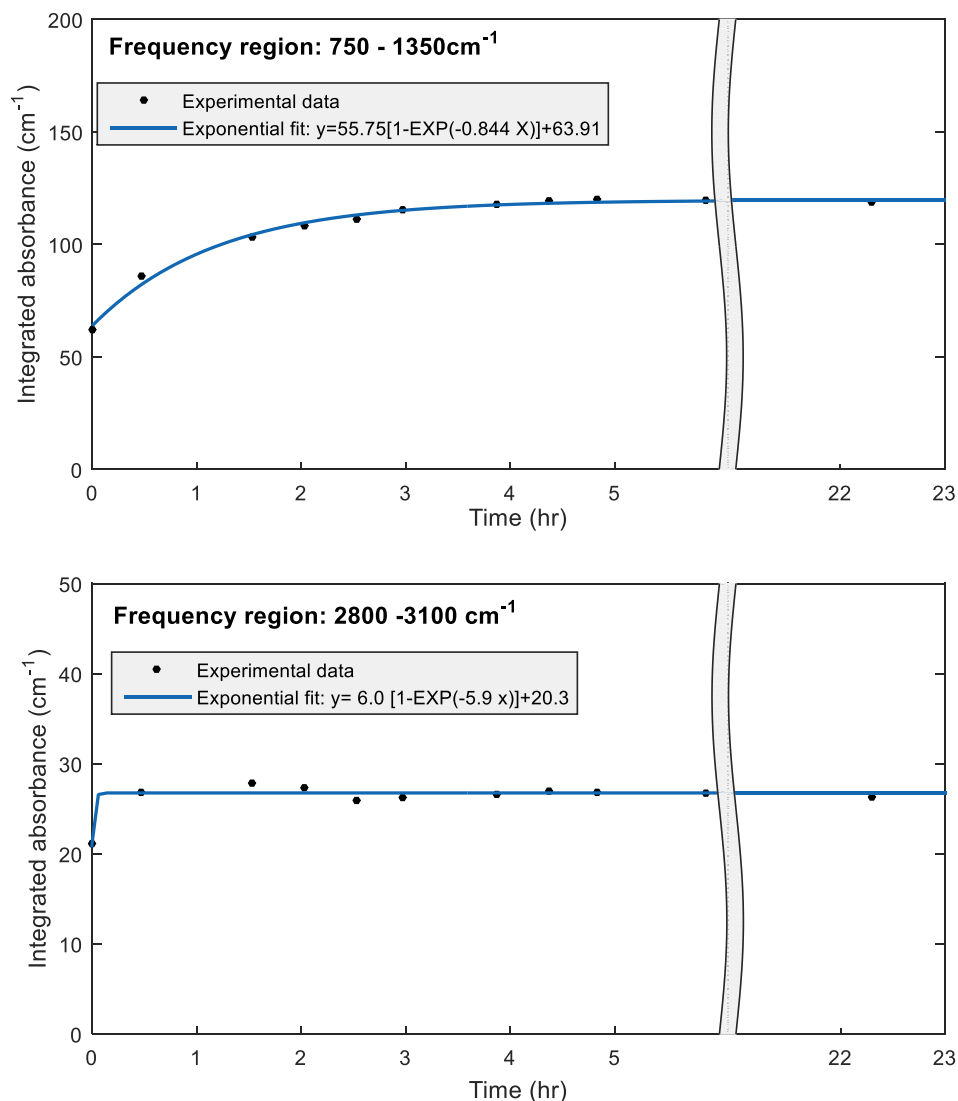


Figure 2-4: Integrated absorbance vs time for DMMP in two different wavenumber range. The uncertainties in integrated absorbance based on the placement of baseline was less than 2.27%.

The OPC compounds are liquid at room temperature and have a very low vapor pressures making manometric measurements of their concentration extremely difficult. One way to measure FTIR spectra of low vapor pressure compounds is to use a calibrated flow method [25], but this is difficult to implement. The method used in this study utilizes a static cell and equilibrium vapor pressure of OPCs at STP for cross section calculations from measured absorbance. To verify the

accuracy, we measured the cross section of Dodecane using our set up and compared it to PNNL data (Figure 2-5). PNNL's measurement was taken at 295 K and 1 atm (broadening gas: Nitrogen) and the resolution used was 0.1 cm^{-1} [12]. The difference in the integrated cross section ($2800\text{-}3000 \text{ cm}^{-1}$) using current study and PNNL's measurement is less than 5%, which is within the uncertainty of our measurement. The vapor pressure of Dodecane (18 Pa at 295K) falls within the range of values for the OPCs studied here. The quantitative difference $[(P_{\text{OPC}} - P_{\text{Dodecane}})/P_{\text{OPC}}]$ for TMP, TEP, DMMP, DEMP and DIMP are 0.82, -0.59, 0.79, 0.59 and 0.49 respectively. Also, to rule out the effect of wall adsorption, we repeated the measurement of one of the OPCs (DMMP) with a cell of different internal surface area (internal surface area was increased by $\sim 25\%$), and the integrated cross section was the within the reported uncertainty (Table 2-3).

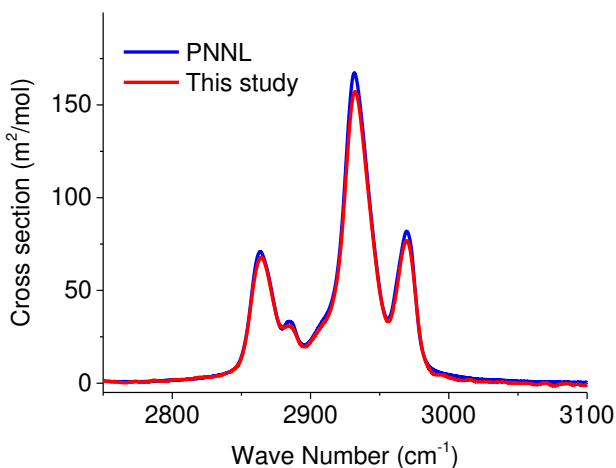


Figure 2-5: Cross section of Dodecane at 295 K and 1 atm: comparison between PNNL's results [12] and current study

2.4 Result and Discussion

Vibrational bands in mid-IR spectra of the five OPC compounds are concentrated in two regions: low frequency region ($650\text{-}1500 \text{ cm}^{-1}$) and high frequency region ($2800\text{-}3100 \text{ cm}^{-1}$). The

intermediate region $1500\text{-}2800\text{ cm}^{-1}$ has no absorption bands. Plots of absorption cross section ($\sigma_{v,T}$) of the OPC compounds in high and low frequency regions are shown in Figure 2-6 and Figure 2-7 respectively and the cross section data is included in the supporting information.

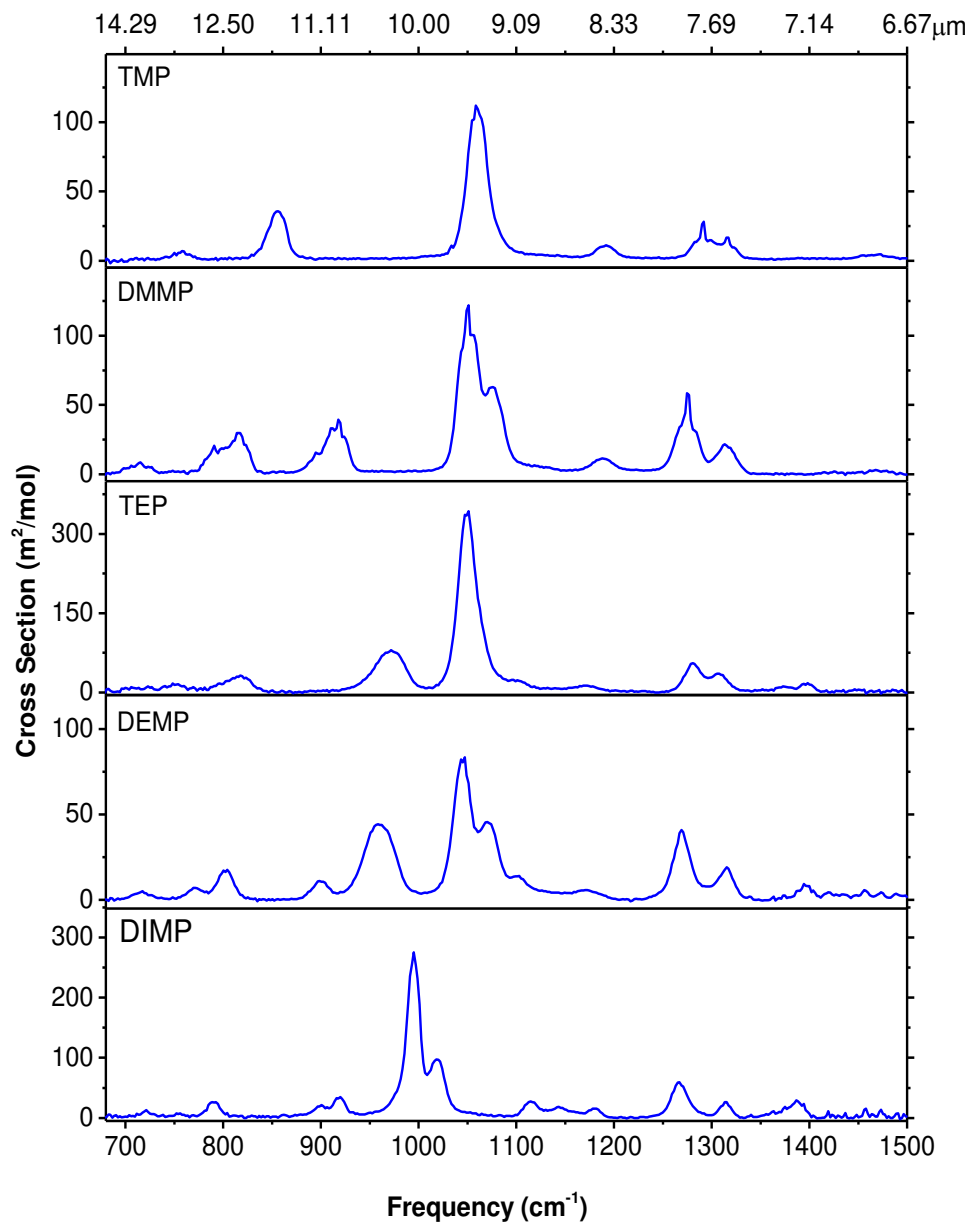


Figure 2-6: Absorption cross section of OPC simulants in low frequency region (650-1500cm⁻¹) at 295 K and 1 atm (broadening gas: N₂).

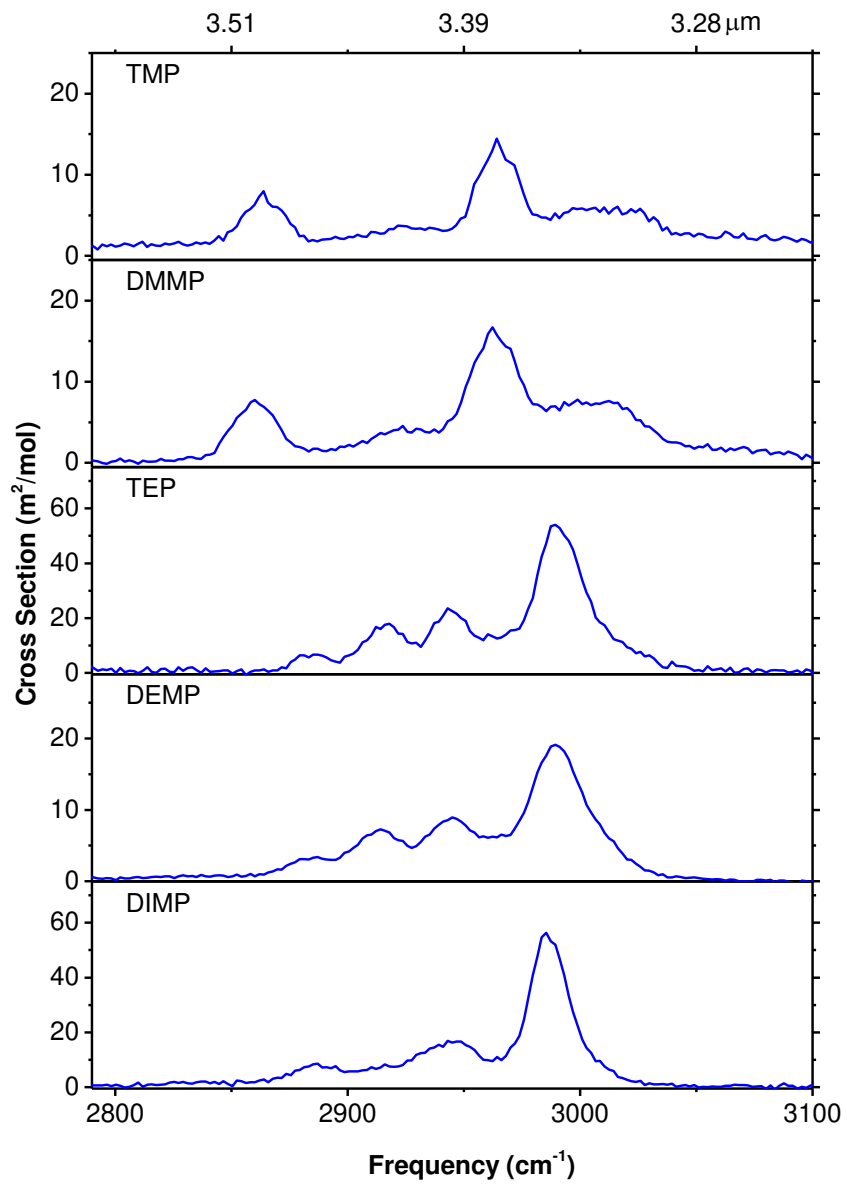


Figure 2-7: Absorption cross section of OPC simulants in high frequency region (2800-3100 cm⁻¹) at 295 K and 1 atm (broadening gas: N₂).

Table 2-2 summarizes important absorption bands, along with their position and cross section values in the five OPC simulants. Vibrational bands in low frequency region ($650 - 1500 \text{ cm}^{-1}$ – shown in Figure 2-6) are due to motion of the center phosphorous atom relative to its neighbors. One of the bands common in all the OPC simulants is due to stretching of the P=O bond, the position of which varied within $1267 - 1292 \text{ cm}^{-1}$ among the five OPC simulants measured in this study. The position of this band strongly depends on electronegativity of the surrounding atoms. Mott et al. [17] simulated spectra of several OPC simulants and CW agents (including Sarin GB and V-agents) and reported that the P=O frequency can vary within $1228-1335 \text{ cm}^{-1}$ range depending on the local environment of P atom.

Table 2-2: Summary of important absorption bands, their position, and peak cross section

	TMP	TEP	DMMP	DEMP	DIMP
Strongest band	$\nu_a(\text{P-O-C})$	$\nu_a(\text{C-C-O})$	$\nu_a(\text{P-O-C})$	$\nu_a(\text{P-O-C})$	$\nu_a(\text{P-O-C})$
Position (cm^{-1})	1058.7	1051.07	1050.1	1047.2	995.1
Peak Cross section (m^2/mol)	111.86	343.15	121.75	83.5	275.12
$\nu(\text{P=O})$					
Position (cm^{-1})	1292.0	1280.6	1274.8	1269.0	1267.07
Peak Cross section (m^2/mol)	28.17	55.04	58.49	41.01	59.49
C-H stretches (2800-3100cm^{-1})					
Integrated (total cross section) $\text{cm}^{-1}\text{m}^2/\text{mol}$	1182.32	2903.52	1272.63	1219.48	2390.06

The most prominent line in the OPCs is located in vicinity of 1050 ($\pm 8 \text{ cm}^{-1}$), except in DIMP, in which it was centered at 995.1 cm^{-1} . In TMP, the strongest absorption band in region 1000 – 1100 cm^{-1} has been previously attributed to anti-symmetric stretching of P-O-C group [17, 18], asymmetric stretch of O-P-O group[14], and P-O-C “antiphase” stretching[15]. Similarly, there is discrepancy in vibrational band assignment for peak in region 800 - 900 cm^{-1} as well, which has been described as P–O–(C) stretching, (P–O)–C vibration, or asymmetric P–O–(C) stretching [15]. This discrepancy shows the complicated nature of vibrations in TMP and is a result of highly mixed vibrations like stretching of the P–O and O–C bonds and deformations of the

O=P-O, P-O-C and O-P-O angles [15]. Fewer studies are available on vibrational band assignments of TEP and DEMP. The most prominent line in TEP (centered at 1051.07 cm^{-1} in this study) has been attributed to asymmetric stretching of ethoxy O-C-C group [14]. In phosphonate molecules (DMMP, DIMP, DEMP) the strongest line is due to asymmetric stretching P-O-C group. It exists as a doublet due to presence of two such bonds. Phosphonate molecules have an additional peak around 900 cm^{-1} due to rocking of P-CH₃ group which is absent in phosphate molecules. This absorption band forms a basis for distinguishing between phosphate and phosphonate compounds. A few weak lines that occur in the range $1350\text{-}1500\text{ cm}^{-1}$ are due to rocking of P-CH₃ and O-CH₃ groups.

Lines in high frequency region ($2800\text{ - }3100\text{ cm}^{-1}$) are relatively weaker and are purely due to C-H stretches. Total integrated cross section in the low frequency region varied from $1182\text{ m}^2\text{cm}^{-1}\text{mol}^{-1}$ (in TMP) to $2903.5\text{ m}^2\text{cm}^{-1}\text{mol}^{-1}$ (in TEP). Within this region, the individual C-H stretches occur at lowest frequency, followed by symmetric C-H stretches, and then asymmetric C-H stretches at the highest frequency [17].

2.5 Uncertainty Analysis

The results of uncertainty analysis are shown in Table 2-3. Measurements were carried out at room temperature 295 K and $\sim 1\text{ atm}$ (758 torr) of ambient air. Since there was temperature gradient in the cell due to heated windows, uncertainty in gas temperature was taken as $\pm 5\text{ K}$. The pressure was measured using a Baratron capacitance gauge (1000 Torr full-scale range) and was $\sim 1\text{ atm}$ ($758 \pm 1\text{ Torr}$). Aggregate uncertainty in the measured vapor pressure for DMMP, DEMP and DIMP was reported to be 1.9% [23] and that in TEP was 1.7% [24]. The uncertainties in gas

temperature and saturation vapor pressure data resulted in uncertainty in calculated molar density n_i , which is also shown in the table. The uncertainty in absorbance varies at each wavenumber therefore the reported uncertainty is the average of uncertainties (inverse of signal to noise ratio) in peak absorbance values in the given frequency range. Finally, the relative uncertainty in cross section, $\sigma_{(v, T)}$ is root mean square (RMS) of relative uncertainties in path-length, molar density, absorbance. The maximum uncertainty in cross section at high and low frequency range is 8.8 % and 11.6%, respectively for TMP. The major contributor for the high uncertainty is the uncertainty in measured absorbance. Most absorption lines in TMP are weak and have low signal to noise ratio, thus contributing to the high uncertainty in absorbance.

Table 2-3: Uncertainty in cross section measurements

Parameters		Uncertainty					
		TMP	DMMP	TEP	DEMP	DIMP	
Measured variables	T[K]	±5	±5	±5	±5	±5	
	Total Pressure (Torr)	±1	±1	±1	±1	±1	
	Vapor Pressure	5%	1.90%	1.77%	1.90%	1.90%	
	Path length	0.58%	0.58%	0.25%	0.25%	0.58%	
	Absorbance: 650-1500cm ⁻¹	7.04%	3.33%	8.14%	2.30%	5.92%	
	Absorbance: 2800-3150cm ⁻¹	10.36%	5.53%	7.03%	5.65%	6.08%	
Calculated variable	n_i	5.28%	2.55%	2.45%	2.55%	2.55%	
	Cross section (σ)	650-1500cm-1	8.82%	4.23%	8.51%	3.44%	6.47%
		2800-3150cm-1	11.64%	6.12%	7.45%	6.20%	6.62%

2.6 Conclusions

Absorption cross sections of five organo phosphorous simulants were measured in mid IR region (650 - 3500 cm⁻¹) using FTIR. To the best of our knowledge, this is the first quantitative absorption spectra of OPC compounds reported in literature. The IR lines were concentrated in

regions $650 - 1500 \text{ cm}^{-1}$ and $2800 - 3100 \text{ cm}^{-1}$ (low and high frequency regions). The most prominent line was located within $995.1 - 1058.7 \text{ cm}^{-1}$ and the peak cross section varied from $83.5 \text{ m}^2/\text{mol}$ (DEMP) to $343.15 \text{ m}^2/\text{mol}$ (TEP). Lines in high frequency region were relatively weaker. The cross section and lines position data reported in this study are critical in development of quantitative absorption diagnostic schemes for detection of CW simulants during combustion.

CHAPTER 3: SHOCK TUBE AND KINETIC MODELLING STUDY OF TRI-ETHYL PHOSPHATE (TEP)²

3.1 Introduction

Incineration is an effective method for destruction of chemical warfare (CW) agents such as G-agents (e.g., sarin - GB) and V-agents (e.g., VX). An increased threat of CW stockpiles has renewed interest in combustion chemistry of these highly toxic chemical agents. In order to design effective incinerator furnaces and afterburners and to predict the destruction rates of CW agents, it is critical to develop an accurate chemical kinetic model that incorporates their destruction chemistry[3]. However, due to high toxicity of these agents, laboratory experiments are carried out using organo-phosphorous compound (OPC) simulants which contain C, H, O, and P atoms. Chemical structure and properties of simulants are similar to that of the toxic CW agents and knowledge on their combustion chemical kinetics can be used to predict the destruction of CW agents.

In the literature, there have been studies on combustion of OPCs, trimethyl phosphate (TMP) and dimethyl methyl phosphonate (DMMP) being the most common because of their use as flame retardants. Hence combustion studies on these chemicals have been focused mainly on their influence as an additive in transformation, structure and propagation of hydrogen and hydrocarbon flames[2, 26-30]. Decomposition of these OPCs takes place via H-abstraction of methyl group by H or OH radical, which is a slow process, compared to six-center molecular eliminations that take place during decomposition of larger OPCs including sarin-GB. Hence, Zegers and Fisher [31-33]

² Published in *The Journal of Physical Chemistry A* 122.15 (2018): 3829-3836

conducted pyrolysis studies of three larger OPC simulants: TEP (Triethyl phosphate), DIMP (Diisopropyl methyl phosphonate) and DEMP (Diethyl methyl phosphonate) in a flow reactor and used gas-chromatography / mass-spectrometry along with FTIR for products identification and quantification[31-33]. These experiments were carried within 700 to 900 K and pyrolysis products time histories were measured within 15 to 90 ms residence time. Based on these measurements, unimolecular decomposition rates and reaction pathways during pyrolysis of these OPC simulants were proposed. These measurements and thermochemical kinetics estimations have enabled the development of LLNL's OPC incineration mechanism[34, 35]. However, predictive capabilities of this model have not been fully assessed against different combustion temperature and pressure conditions mainly due to lack of such experimental data. TEP (structure in Figure 3-1) has been identified as one of the simulants for sarin-GB based on its chemical structure and activation energy barrier[36]. As understood from the literature review, TEP pyrolysis has been conducted only in flow reactor at lower temperatures and slower heating rate.

In this chapter, we measured CO concentration time-histories during pyrolysis and oxidation of an OPC simulant - TEP, using shock tube and laser absorption techniques. This is the first shock tube study on kinetics of TEP decomposition at high concentrations and the experiments provide the first laser-based time history measurements of CO during its pyrolysis and oxidation. LLNL's OPC incineration mechanism[34, 35] created in the early 2000s was used with the Chemkin Pro software[37] to predict the experimental results. The model did not adequately predict the CO time histories during TEP pyrolysis and oxidation at current experimental conditions. Thus an improved kinetic model has been developed which is built upon the recently validated AramcoMech2.0[38] mechanism's C₀-C₂ base chemistry and LLNL sub-mechanism for phosphorous chemistry.

Thermochemistry of the P-containing species were updated which led to further improvement in the model in terms of predicting experimental CO time history. Sensitivity analysis has been carried out using the improved model and key reactions were identified for further refining the model.

3.2 Experimental Setup and Procedure

3.2.1 Shock Tube Facility

Experiments were performed in the reflected shock region of high purity, double-diaphragm, stainless steel shock tube at UCF shock tube facility with ID=14.17cm (details in our previous work[5]). Since TEP has a very low vapor pressure (11.16 Pa at STP) [24], heating prevents condensation of test mixture on the walls of the shock tube. The driven section of the shock tube was heated to $T_1 = 373$ K using eight sections of a custom-made heating jacket with temperature controlled using four benchtop PID temperature controllers to ensure temperature uniformity along the length of shock tube. Before each experiment, the driven section was evacuated to < 5.3 Pa using a rotatory vane pump (Agilent DS102) before filling with 3.3 - 8.7 kPa of test mixtures (pre-shock pressure, P_1).

Incident shock velocity was measured using five piezoelectric pressure transducers and extrapolated to obtain the incident shock velocity at the end wall. 5 mm diaphragm was used in current work to get the desired P_5 (pressure behind reflected shock wave) of ~ 1.3 atm (131,722 Pa). Conditions behind the reflected shock wave (P_5 and T_5 with uncertainties 1.8% and 2%, respectively) were calculated based on the measured velocity, P_1 , T_1 , and one-dimensional normal shock equations. The shock tube configuration and use of driver inserts allowed to obtain a

constant P_5 behind the reflection shock region for test times of ~ 3 ms (P_5 was also monitored using Kistler type 603B1 sensor).

3.2.2 Fuel/oxidizer Mixture Preparation

Research grade TEP ($> 99\%$ pure; Acros Organics) and gases (O_2 , Ar, $> 99.999\%$ purity; nexAir) were used to prepare test gas mixture manometrically in a high purity, 33 L, Teflon coated, stainless steel, heated mixing facility (heated to 423 K) designed specifically to accommodate low vapor pressure OPC compounds. The temperature of mixing manifold and transfer line to the shock tube was maintained at 392 ± 5 K. The entire mixing system was well insulated to avoid cold spots that can allow fuel condensation. Before injecting liquid TEP, the tank was evacuated to $P < 2.67$ Pa with a rotary vane pump (Agilent DS102). Partial pressures were measured with 100 Torr and 10,000 Torr full scale range baratrons (MKS Baratron E27D and 628D). The mixtures were let to mix for at least 3 hours before the first shock tube experiments using magnetically driven stirrer (to ensure homogeneity of the mixtures).

TEP has a low vapor pressure of 11.16 Pa at STP and increases to 15465 Pa at 423 K (temperature of the mixing tank)[24]. To minimize fuel condensation, the partial pressure of TEP was kept less than 50% of its saturation vapor pressure at respective temperatures at all times. To verify the initial TEP concentration in the test section of the shock tube, cross section measurement of 1% TEP in argon bath gas was carried out using an external cell (path-length = 14.32 cm; ID = 23 mm) equipped with ZnSe windows at 373 K. Mixture was transferred directly to the heated external cell using a short, heated transfer line to minimize losses due to condensation and wall adsorption. TEP has a broad and strong absorption line centered at $9.54 \mu\text{m}$ due to asymmetric

stretching of ethoxy O-C-C group[14]. Hence, P22 line from a CO₂ gas laser (Access Laser) at 9.569 μm was used for the cross section measurement (laser diagnostics details in our recent work[4]). Cross section of 1% TEP in Ar (at T = 373 K and P_{total} = 0.72 atm) was measured to be 25.79 m²/mol with uncertainty of 2.01%. Thus, TEP mole fractions in test mixtures during shock tube experiments were verified using laser absorption with the measured cross section. Figure 3-1 shows measured absorbance of 0.075% TEP mixture at different pressures showing a linear trend (indicating no condensation). Uncertainty in measured initial TEP mole fraction was estimated to be ±2.29%.

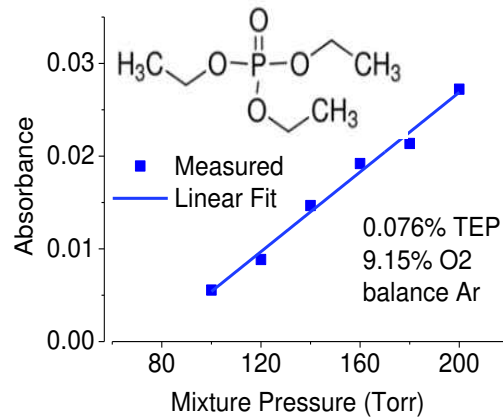


Figure 3-1: Absorbance vs pressure plot for TEP test mixture showing a linear trend

3.2.3 CO Mole Fraction Measurements and Comparison with Model Prediction

A quantum cascade laser (QD4580CM1) operating at 4580.4 nm was employed to probe the R(10) transition line for CO. A 50/50 beam splitter was used to split the laser light into two beams: transmitted (I_{tr}) and reference (I_{ref} to monitor laser power fluctuation). Transmitted beam was directed through the test section via two sapphire windows and a narrow band pass filter (Thorlabs model #FB4500-500) was used to filter out emissions from hot gasses and was collected

in a thermoelectrically cooled MCT (HgCdTe) Vigo Systems PVI-2TE-5.0 photovoltaic detector.

The CO mole fraction was obtained from the Beer–Lambert law:

$$\alpha = -\ln\left(\frac{I_{tr}}{I_{ref}}\right)_v = \sigma(\nu, T, P) \frac{P_{tot}}{RT} \chi L \quad (3-1)$$

where α_v is absorbance, σ [cm²/molecule] is absorption cross section, P [atm] is pressure, and T [K] is temperature, L [cm] is path length, and χ is the mole fraction of the absorbing species. The CO cross section (σ [cm²/molecule]) at T₅ and P₅ were taken from the HITRAN database[39] (assuming self-broadening), which were validated in UCF shock tube experiments performed with pure CO and Ar for pressures up to 10 atm (maximum deviation of $\pm 6.8\%$). Major pyrolysis products during TEP pyrolysis (C₂H₄, C₂H₅OH, CH₄, C₃H₆, C₂H₂) identified using the LLNL's kinetic model showed no absorption feature near 4.6 μm allowing for interference free detection of CO at the chosen wavelength. For oxidation experiments, interference from CO₂ formation were calculated to be within uncertainty in measured absorbance due to experiments signal-to-noise. The uncertainty in measured CO mole fraction was estimated to be 7.2% (due to combined uncertainty in spectroscopic parameters: P₅, T₅, path length and CO cross section) or ± 123 ppm (experimental uncertainty due to noise in the measured absorbance signal), whichever is greater.

3.3 Kinetic Modeling

Improved kinetic model for TEP was developed and was based upon the recently validated AramcoMech2.0[38] for C₀-C₂ hydrocarbon chemistry. Phosphorous reactions were taken from LLNL's OPC incineration mechanism with addition of TEP sub-mechanism from Glaude et. al.[35]. TEP decomposition pathway in the current kinetic model is same as described

previously in Zegers and Fisher[33] and Glaude et. al.[35], consisting of seven unimolecular decomposition reactions that take place by forming six-center or four-center cyclic complexes as shown in Figure 3-2. The first step is unimolecular decomposition of TEP that takes place when an H atom of an ethyl group is abstracted by the O atom of P=O group to form a six-center cyclic transition state. This leads to formation of diethyl phosphate and ethylene as products. Diethyl phosphate can either undergo similar six-center elimination to form mono-ethyl phosphate and ethylene or form a four-center transition state by abstraction of H atom in the OH group leading to elimination of ethanol as a product. The rest of the reactions proceed in similar way by six-center and four-center concerted reactions eliminating ethylene and ethanol, respectively.

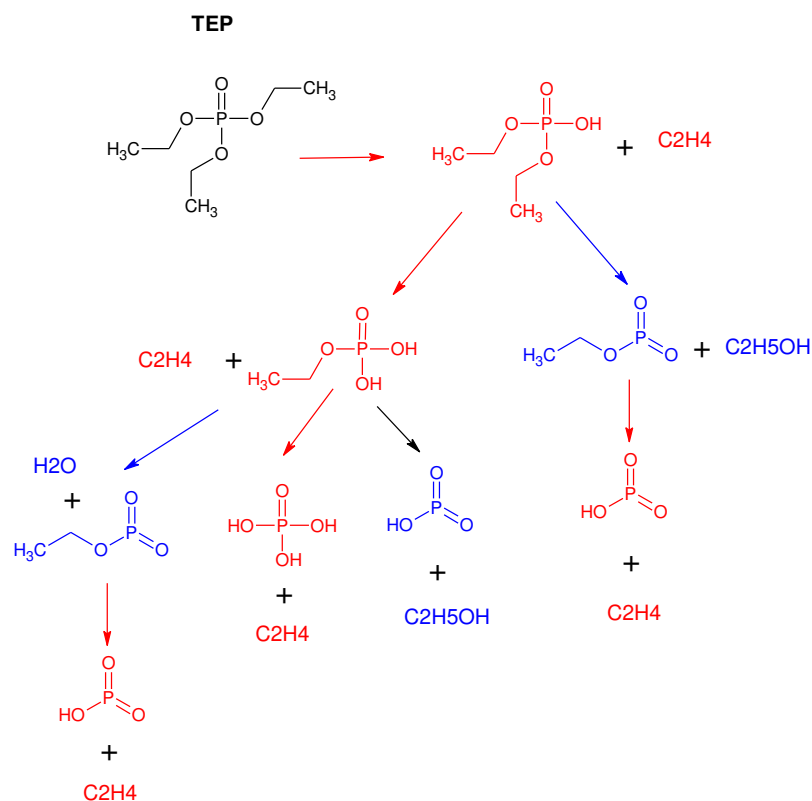


Figure 3-2: TEP decomposition mechanism as suggested in Zegers and Fisher[33] and Glaude et al.[35], showing six-center (Red) and four-center (blue) elimination reactions to eliminate C_2H_4 and $\text{C}_2\text{H}_5\text{OH}$ respectively.

Since ethylene (C_2H_4) is one of the major intermediate products in TEP decomposition, we attempted to measure its mole fraction yield at $10.532\mu\text{m}$ using a tunable CO_2 laser, the setup which was previously used in C_2H_4 measurement during n-heptane oxidation[4]. However, a good C_2H_4 signal was not obtained at given experimental conditions and TEP compound loading, possibly due to interference from the parent compound and initial decomposition products containing O-P-O groups. TEP has a strong and broad absorption feature centered at $10.28\mu\text{m}$ due to asymmetric stretching of O-P-O group[14] and hence interferes with C_2H_4 measurement. Also, cross section of C_2H_4 is 15-20 times lower than CO at the experiments conditions (T5 and P5)

which makes it difficult to detect C_2H_4 (compared to CO). We tried using high concentration TEP mixture (up to 2%) in an attempt to measure C_2H_4 but due to condensation and other losses, such experiments were extremely difficult to implement and resulted in high uncertainty in initial TEP mole fraction. Hence, kinetic modelling and reaction rate recommendations in the current study have been based on the measured CO time history during TEP oxidation and pyrolysis. Figure 3-3 shows the pathways for CO formation from C_2H_5OH and C_2H_4 during TEP pyrolysis and oxidation.

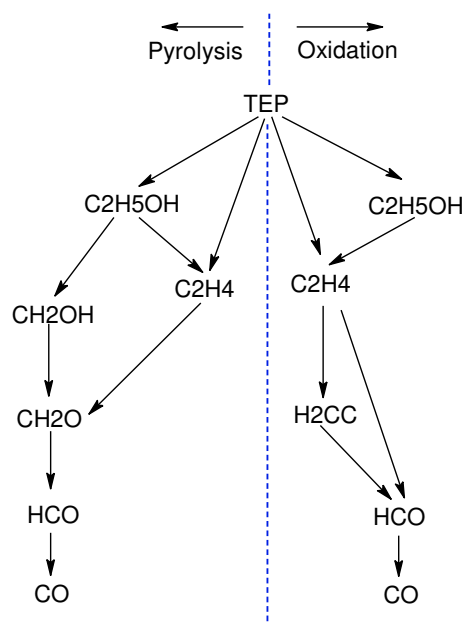


Figure 3-3: CO formation pathway during pyrolysis and oxidation of TEP after $1\mu s$ test time using reaction path analyzer tool in Chemkin Pro.

3.4 Thermochemistry

Accurate thermochemical data is important in chemical kinetics modeling to predict mixture temperatures and rates of reversible reactions. Thermochemical data of 27 phosphorous containing species were re-evaluated using group additivity method in THERM software[40] and remaining 13 species for which group values were not available, theoretical calculation (CBS-

QB3) was used to calculate thermochemical data. For group additivity method, new group values proposed by Khalifa et. al.[41] as a result of their extensive quantum chemistry calculations (CBS-QB3 level of theory) were used. OPC compounds contains heavy atoms like C, P and O and are fully branched and gauche interactions among various groups are possible. However, for smaller P-species (containing less than 4 carbon atoms – like DMMP, TMP and their derivatives), no gauche interactions were taken into account. This method resulted in most accurate estimation of enthalpies of formation (less than ± 1 kcal/mol deviation) when compared to the results of theoretical calculations of available species in Khalifa et. al.[41]. For highly branched alkane (with number of C atoms greater than 4), alkane gauche (AG) interaction exists which adds 0.8 kcal to the heat of formation of the species. Thus, for TEP and their derivatives, up to two alkane gauche interaction groups were also taken into account depending on the geometry of the molecules. One optical isomer (OI) group was added for every chiral center, adding $R \ln(2)$ to entropy of the species, which affects the equilibrium constant of a chemical reaction. The new NASA polynomial was used to evaluate properties at different temperatures and were compared with results of CBS-QB3 calculations for selected species in Khalifa et. al.[41] and agreement was within ± 2 kcal/mol for enthalpy of formation and ± 3 cal/mol for entropy. For those species whose group values were not available, theoretical calculation using CBS-QB3 level of theory in Gaussian 09 software was carried out to evaluate the thermochemical data. Computational method used was same as described in Khalifa et. al.[41] for calculations of group values of P-containing species using CBS-QB3 method. To check the accuracy of our method, thermochemical data of DMMP was calculated using the same level of theory and was compared to the results of Khalifa et. al.[41] and agreement

was within ± 2.2 kcal/mol. Appendix A contains the results of CBS-QB3 calculations for 13 P-containing species.

3.5 Results and Discussions

Carbon monoxide mole fraction yields during pyrolysis of TEP at temperature range 1462-1673 K and at pressure ~ 1.3 atm are shown in Figure 3-4. Experiments were also carried out at lower temperature (1300 K and 1atm), however CO was not detected and the results are not included in this paper. In a flow reactor study of TEP pyrolysis at temperature 700-900K[33], C_2H_4 and C_2H_5OH were identified as the major pyrolysis products; CO was used as a tracer gas in initial gas mixture and was not identified as a pyrolysis product. In the current study, shock tube experiments were carried out at higher temperatures and CO was a major product, as seen in Figure 3-4, which also shows the predicted CO yield using three different kinetic models:

Model i. LLNL's original OPC incineration mechanism;

Model ii. Updated HC (hydrocarbon chemistry) model - contains C_0 - C_2 chemistry from AramcoMech.2.0 and phosphorous chemistry from LLNL; and

Model iii. Thermochemistry (Therm) updates to all P-containing species from current work to model (ii)

All simulations were carried out using constant pressure model in CHEMKIN PRO software. As shown in Figure 3-4, LLNL model (model i) significantly underpredicts CO formation during TEP pyrolysis. After updating the hydrocarbon chemistry (model ii), predicted CO yield increased and using the updated thermochemical data (model iii) for P-containing species

further improved the predicted CO yield. However, the predicted CO yield is still lower than the experimental values.

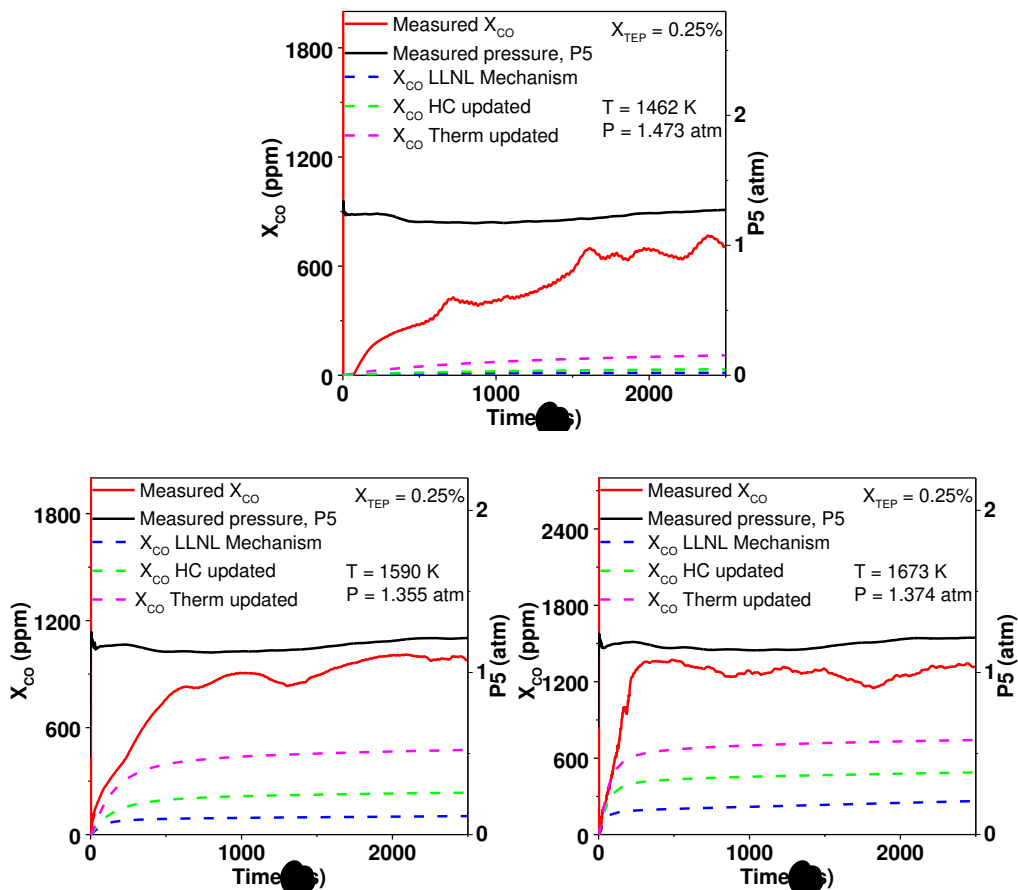


Figure 3-4: Measured CO time history during TEP pyrolysis and comparison with model predictions. For clarity, the CO mole fraction traces have been smoothed using 100 point moving average.

Figure 3-5 compares measured and predicted CO yield during TEP oxidation at temperatures 1213 - 1508 K and pressure ~ 1.3 atm. At all three temperatures, LLNL model predicted slower rate of CO formation as compared to experimental data. Updating the hydrochemistry from AramcoMech2.0 improved the time scale of CO formation and are in very good agreement with the experimental yields for temperatures 1213 and 1387 K. However, at

higher temperature (1437 and 1508 K), the updated model is still slow in predicting CO time history (model iii did not have significant difference from model ii).

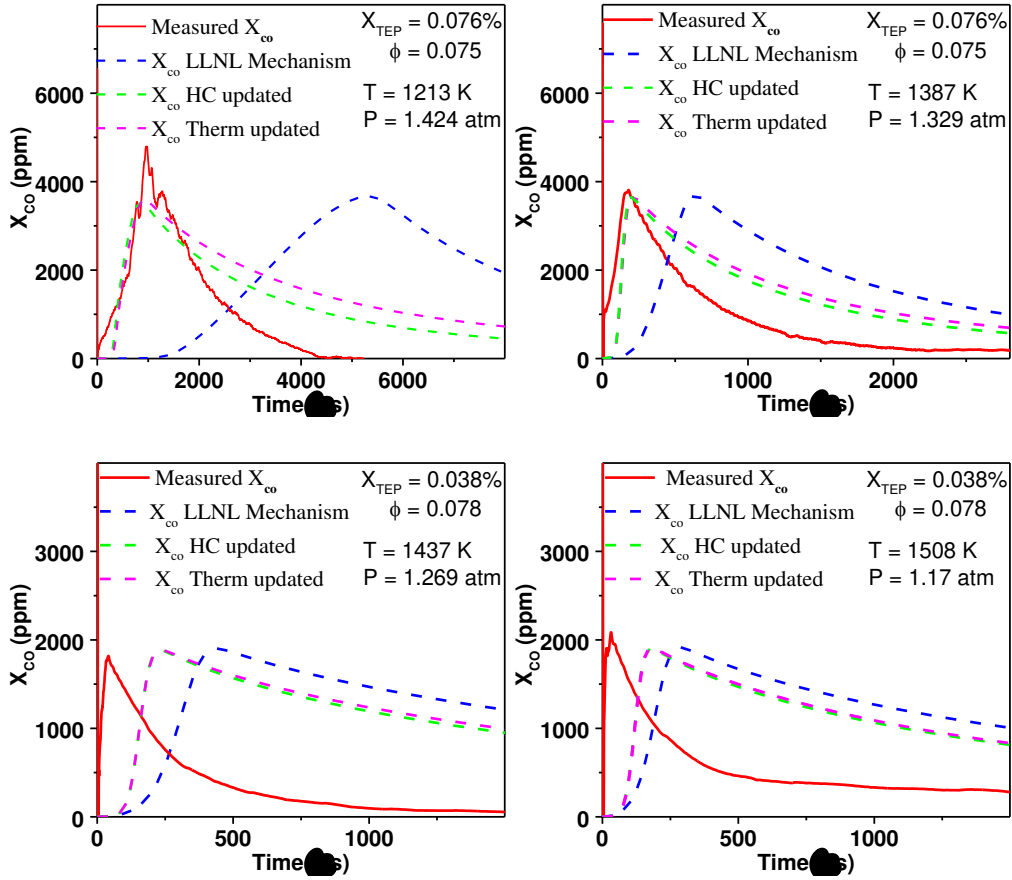


Figure 3-5: Measured CO time history during TEP oxidation and comparison with model predictions. For clarity, the CO mole fraction traces have been smoothed using 100 point moving average.

To further understand the disagreement between predicted and measured CO yield, sensitivity analysis was carried out in Chemkin Pro. Sensitivity coefficient (S) for i th reaction rate (k_i) for a species is defined as

$$S(X_{species}, k_i, t) = \left(\frac{d X_{species}(t)}{d k_i} \right) \left(\frac{k_i}{X_{species}(t)} \right) \quad (3-2)$$

CO sensitivity coefficients for of top ten reactions during 0.25% TEP pyrolysis at 1462 K and 1.473 atm is shown in Figure 3-6. Sensitivity analysis was carried out using model iii, which has more accurate C/H/O chemistry (from the recent AramcoMech2.0 and updated thermochemical data for P-containing species (from current work). Hence the purpose of sensitivity analysis was to identify important phosphorus reactions (listed in Table 3-1) that have significant effect on CO time history yield.

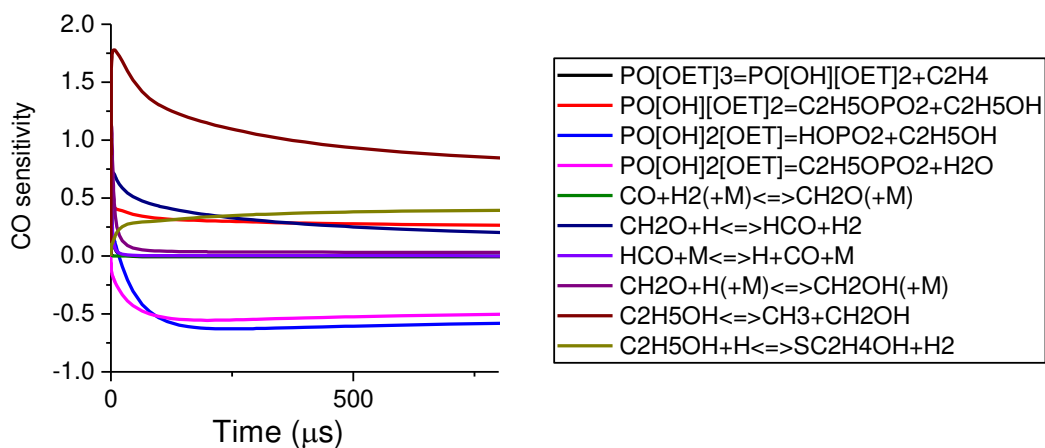


Figure 3-6: Sensitivity coefficients to CO formation showing top 10 most sensitive reactions during TEP pyrolysis.

Table 3-1: Dominant phosphorous reactions to CO mole fraction yield during TEP pyrolysis and their rates from LLNL's OPC incineration mechanism [35]

RXN #	RXN	A (s ⁻¹)	n	E _a (cal mol ⁻¹)
1	PO[OET]3=PO[OH][OET]2+C2H4	2.80E+13	0	45300
2	PO[OH][OET]2=C2H5OPO2+C2H5OH	2.50E+13	0	44000
3	PO[OH]2[OET]=HOPO2+C2H5OH	2.50E+13	0	44000
4	PO[OH]2[OET]=C2H5OPO2+H2O	5.00E+13	0	45000

Rxn.1 is the first step in TEP decomposition, which proceeds via formation of six-center transition state as described in Section 3. Zegers and Fisher[33] measured this unimolecular decomposition by following decay of TEP during its pyrolysis in a flow reactor within a narrow T range of 706-854 K. Based on Zegers and Fisher's experimental measurement and using analogy with ester[42] and DEMP[31] decomposition reactions that involve same kind of transition state, Glaude et. al.[34, 35] estimated the rate in LLNL's kinetic model (given in Table 1). More recently, Hahn et. al.[43] used ab initio calculations to compute kinetic parameters for the reaction at temperature 570-940 K using two levels of theory - CVT/SCT and VTST-ISPE/SCT. Results from CVT/SCT calculations were more in agreement with experiment/estimated values (k_{cal}/k_{expt} at 700 K < 6.2) than VTST-ISPE/SCT calculations (k_{cal}/k_{expt} > 20). The authors also computed reaction rates at 1000, 1500 and 2000 K using CVS/SCT method and the calculated rates were in very good agreement with Glaude's estimation (k_{cal}/k_{expt} = 2.2, 1 and 0.7 respectively). Changing the pre-exponential factor (A-factor) of this reaction up to two orders of magnitude (10^{11} - 10^{15}) did not have significant effect on CO concentration yield during TEP pyrolysis.

Rxns. 2, 3 and 4 are four-center decomposition reactions in which OH group bonded to P atom is abstracted to eliminate ethanol molecule as a product. No experimental measurements or theoretical calculations of kinetic parameters for these reactions has been reported. Glaude et al.[35] made estimation of the rate given in Table 1 based on Zegers and Fisher's[31-33] experimental measurement of alcohol and alkene yield during pyrolysis of DIMP, DEMP and TEP. Although A-factors for majority of four-center elimination reactions fall within $10^{13.5\pm 1}$, a wider spread ranging from $10^{10.8}$ to $10^{14.7}$ has also been reported in the literature[44]. Accordingly, changes were made in A-factors of these reactions within two orders of magnitude (10^{11} to 10^{15}) to assess their effect on predicted CO yield. Increasing the A-factor for Rxn. 2 to 10^{15} increased CO yield – however the increase was not significant enough to match experimental data, and decreasing it to 10^{11} further decreased the CO yield. Change in the A-factor of Rxn. 4 did not make significant impact on predicted CO yield. On the other hand, when A-factor of Rxn. 3 was decreased by two order of magnitude (to 2.5×10^{11}), it significantly increased CO yield to match experimental values. The plots are shown in Figure 3-7 – at lower temperatures (1462 and 1590 K) the predicted CO yield increased to match the experimental data very well. However, at 1673 K the model still falls short in predicting the CO yield.

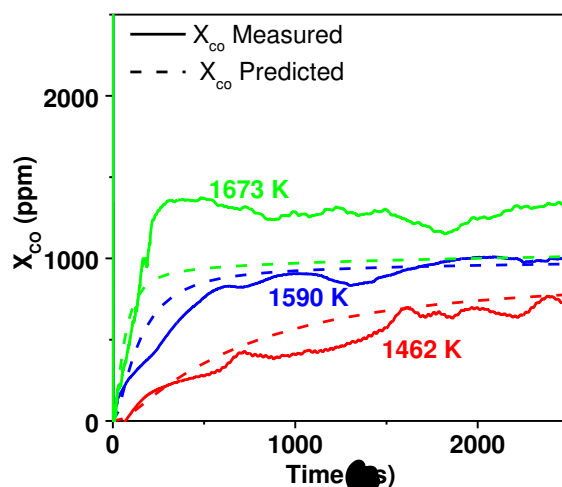


Figure 3-7: Measured vs predicted CO yield during 0.25% TEP pyrolysis after decreasing the A-factor of Rxn.3 by two order of magnitude (to 2.5×10^{11}).

In Rxn. 3, mono-ethyl phosphate ($\text{PO}[\text{OH}]_2[\text{OET}]$) decomposes via four-center concerted elimination to form HOPO_2 and ethanol. There are two additional pathways for $\text{PO}[\text{OH}]_2[\text{OET}]$ decomposition in the TEP sub-mechanism: six-center elimination to form C_2H_4 and orthophosphoric acid ($\text{PO}[\text{OH}]_3$); and another four-center elimination to form H_2O and $\text{C}_2\text{H}_5\text{OPO}_2$ as shown in Figure 3-2. By reducing the A-factor of Rxn. 3, the branching ratio of $\text{C}_2\text{H}_4/\text{C}_2\text{H}_5\text{OH}/\text{H}_2\text{O}$ elimination from $\text{PO}[\text{OH}]_2[\text{OET}]$ changes. According to the sensitivity analysis in Figure 3-6, ethanol bond scission ($\text{C}_2\text{H}_5\text{OH} = \text{CH}_3 + \text{CH}_2\text{OH}$) has the largest positive contribution to CO formation. As shown in reaction pathway diagram in Figure 3-3, CH_2OH formed as a result of ethanol bond scission dissociates to CH_2O ; CH_2O then can decompose to HCO and hence to CO. Sensitivity analysis on $\text{C}_2\text{H}_5\text{OH}$ formation during TEP pyrolysis was also carried out (shown in Figure 3-8) and Rxn. 3 was found to have the highest negative sensitivity for $\text{C}_2\text{H}_5\text{OH}$ formation. Hence, reducing the rate of Rxn.3 by two order of magnitude changed the

branching ratio of $\text{PO}[\text{OH}]_2[\text{OET}]$ decomposition to favor $\text{C}_2\text{H}_5\text{OH}$ formation, which then lead to increased CO formation.

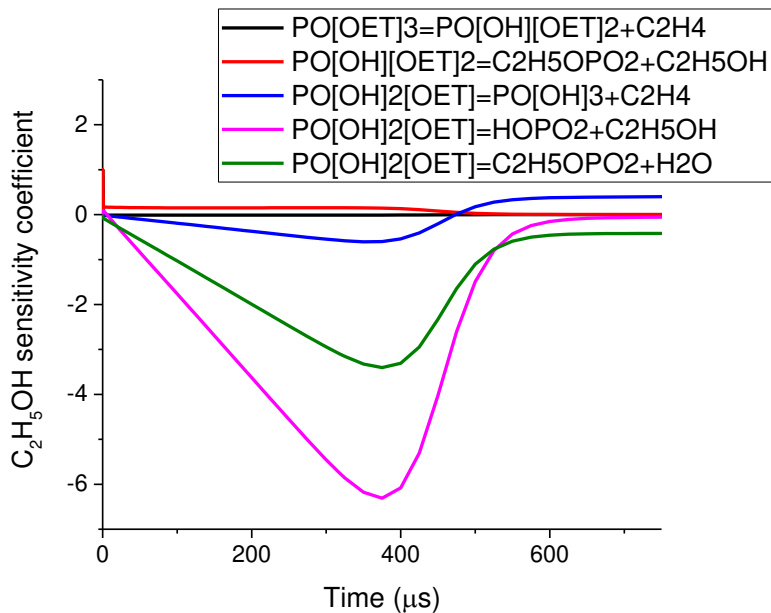


Figure 3-8: $\text{C}_2\text{H}_5\text{OH}$ sensitivity coefficient during TEP pyrolysis at 1462 K and 1.473 atm using the improved model (model iii)

Oxidation simulations were rerun using the updated A-factor for Rxn. 3 and resulted in negligible change in predicted CO yield. Sensitivity analysis for CO formation during TEP oxidation at 1508 K and 1.17 atm was carried out using model iii to identify important reactions in oxidation mechanism and the top ten most sensitive reactions are shown in Figure 3-9. It is clear from the figure that during TEP oxidation, CO mole fraction yield is mostly sensitive to base hydrocarbon chemistry (except for the first step in TEP decomposition).

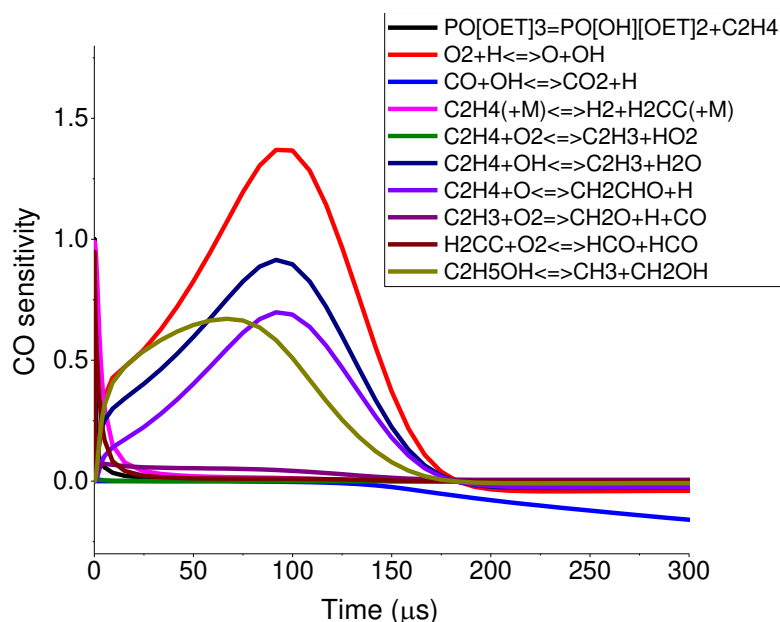


Figure 3-9: CO sensitivity coefficient during TEP oxidation at 1508 K and 1.17 atm using the improved model (model iii)

Due to a number of branching six-center and four-center reaction pathways involved in TEP decomposition mechanism, the final rate expression for these reactions cannot be made based on the results of current study. However, we show in Figure 3-7 that the discrepancies in predictions with experiments seen in Figure 3-4 could be traced to uncertainties in the rates of P-containing reactions. Experimental measurements and theoretical calculations to accurately estimate the rates of these reactions must be carried out in future. Nevertheless, the improved kinetic model for TEP proposed in this study is built upon C/H/O chemistry from AramcoMech2.0; phosphorous chemistry from LLNL mechanism; and with updated thermochemical data (current work) for P-containing species. The improved model better predicts the CO time history during TEP pyrolysis and oxidation. However, further study on kinetics parameters of four-center elimination reactions in TEP sub-mechanism is necessary to reduce uncertainty in the proposed kinetic model.

3.6 Conclusions

We provided the first CO time histories measured using laser absorption spectroscopy at 4580.4nm during pyrolysis and oxidation of a chemical warfare simulant – tri-ethyl phosphate (TEP) behind reflected shock waves. Measured CO yield during the experiments were compared with model predictions using the LLNL detailed kinetic mechanism, which under predicted CO yield during TEP pyrolysis. Also, for oxidation, the predicted CO production rate was slower than the data.

New improved model was proposed in the current study which uses C₀-C₂ hydrocarbon chemistry from AramcoMech2.0 and phosphorous chemistry from the LLNL mechanism, along with updated thermochemical data from current work for P-containing species. The predicted CO yield during TEP pyrolysis using improved kinetic model was better, however, the increase was not significant enough to match the experimental results. For TEP oxidation, updating H/C/O chemistry from AramcoMech.2.0 improved predicted CO production rate to match experimental data very well at temperatures 1213 and 1387 K. However, at higher temperatures (>1437 K) the improved model is still slow in predicting the CO yield.

From the results of sensitivity analysis, dominant phosphorus reactions that play important role in CO formation were identified. Due to involvement of a number of branching six-center and four-center elimination reactions, the rates for these reactions cannot be recommended yet based on the measured CO time history data. However, from the analysis of the experimental and kinetic modelling results, it is clear that the kinetic parameters of four-center elimination reactions in TEP sub-mechanism should be further investigated. Future experimental measurements

combined with theoretical calculations must be conducted for these reactions, which will minimize the uncertainty in the proposed kinetic model for TEP pyrolysis and oxidation.

CHAPTER 4: THEORETICAL CALCULATION OF REACTION RATES AND COMBUSTION KINETIC MODELING STUDY OF TRI-ETHYL PHOSPHATE (TEP)³

4.1 Introduction

The United Nations mandated destruction of all chemical warfare (CW) stockpiles for its Convention signatories and the preferred method adopted by the United States is incineration [3, 45-50]. Incineration involves heating the chemical agents to a high temperature in an enclosed reactor so that it decomposes completely into non-toxic products. A chemical kinetic model incorporating detailed chemistry of the CW agents is essential to predict their decomposition temperatures, pathways, end-products and to design an effective incinerator. Accuracy of chemical kinetic models can be determined by validating them against well calibrated experimental data. Since CW agents are too toxic for laboratory use, experiments are carried out using simulants. Once an accurate model for a simulant has been developed using theoretical and experimental approaches, the modeling techniques can be extrapolated to develop a kinetic model of CW agents. Tri-ethyl phosphate with the chemical formula PO[OET]₃ (see Figure 4-1) is an organophosphorous compound (OPC), commonly used as a simulant for Sarin, GB.

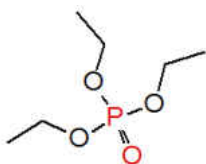


Figure 4-1: Triethyl phosphate (TEP)

³ Published in *The Journal of Physical Chemistry A* 123.22 (2019): 4764-4775

In the first report of our study on TEP kinetic mechanism construction (Chapter 2) [51], we developed a kinetic model for TEP combustion. It was based upon AramcoMech2.0[38, 52] mechanism for base hydrocarbon (C₀-C₂) chemistry and Lawrence Livermore National Lab (LLNL)'s OPC incineration mechanism[35]. TEP decomposition pathway consisting of seven molecular elimination reactions and their estimated rates coefficients were taken from Glaude et. al[35]. Thermochemistry of phosphorus containing species were updated using either theoretical calculations at CBS-QB3 level of theory, or by group additivity method. The proposed mechanism was used to predict CO time-histories during TEP pyrolysis and oxidation. The predicted yields were compared with experiments carried out using shock tube and laser absorption spectroscopy within 1200-1700K and near 1 atm. Although the proposed model showed some improvements in terms of predicting CO mole fraction yield, there were remaining discrepancies with experiments. For TEP pyrolysis, the predicted CO yield was lower and for oxidation predicted CO formation and destruction rates were slow as compared to experiments (Figure 4-2).

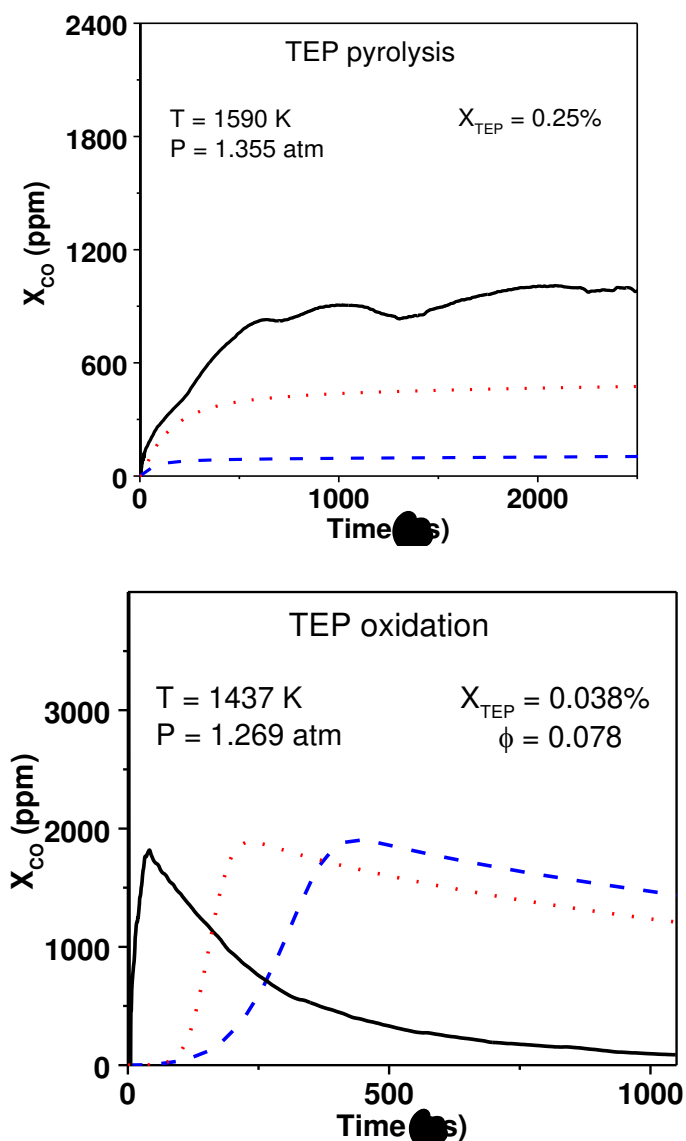


Figure 4-2: Experiment and predicted CO time-histories during TEP pyrolysis and oxidation. **Solid line:** Experiments; **Dashed line:** LLNL OPC incineration mechanism with addition of TEP pyrolysis sub-mechanism from Glaude et. al [35]; **Dot line:** TEP mechanism proposed in our Chapter 2 [51].

In this chapter, we aim to further improve our kinetic mechanism for TEP decomposition. We used conventional transition state theory based on CBS-QB3 quantum chemistry calculations to predict the reaction rates of eight phosphorous containing reactions, listed in Table 4-1. The

reactions were chosen based on the results of sensitivity analysis shown in Figure 4-3. Sensitivity coefficient (S) for i th reaction rate (k_i) for a species is defined as:

$$S(X_{species}, k_i, t) = \left(\frac{d X_{species}(t)}{d k_i} \right) \left(\frac{k_i}{X_{species}(t)} \right) \quad (4-1)$$

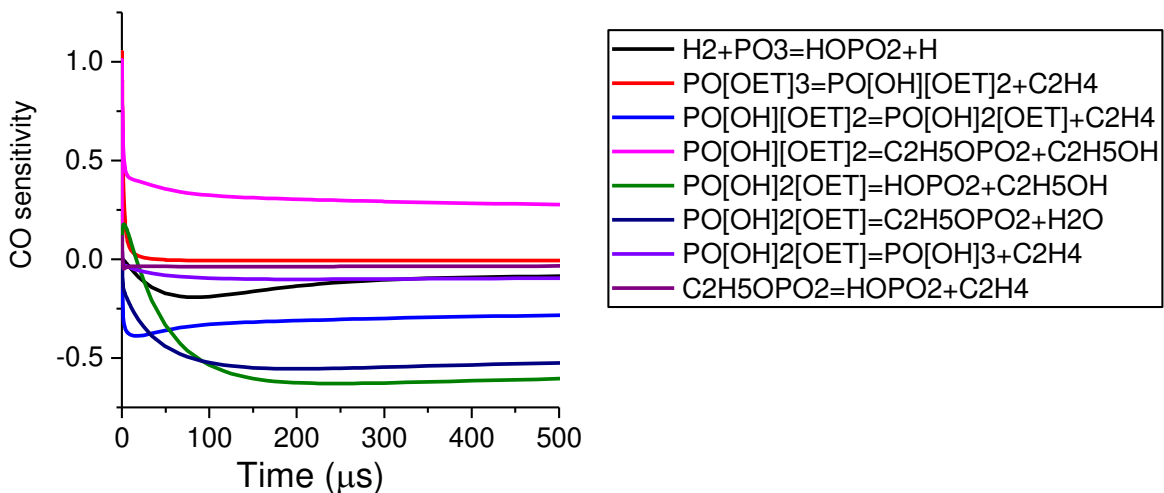


Figure 4-3: Sensitivity coefficients of important phosphorous reactions in TEP sub-mechanism. Sensitivity analysis was carried out for 0.25% TEP pyrolysis at 1462 K and 1.47 atm using TEP kinetic model from Neupane et al [51]. Only top phosphorous containing reactions are shown.

Table 4-1: TEP reactions chosen for CBS-QB3 analysis based on results of CO sensitivity analysis shown in Figure 4-3.

RXN #	RXN
R1	$\text{PO}[\text{OET}]_3 = \text{PO}[\text{OH}][\text{OET}]_2 + \text{C}_2\text{H}_4$
R2	$\text{PO}[\text{OH}][\text{OET}]_2 = \text{PO}[\text{OH}]_2[\text{OET}] + \text{C}_2\text{H}_4$
R3	$\text{PO}[\text{OH}][\text{OET}]_2 = \text{C}_2\text{H}_5\text{OPO}_2 + \text{C}_2\text{H}_5\text{OH}$
R4	$\text{PO}[\text{OH}]_2[\text{OET}] = \text{PO}[\text{OH}]_3 + \text{C}_2\text{H}_4$
R5	$\text{PO}[\text{OH}]_2[\text{OET}] = \text{HOPO}_2 + \text{C}_2\text{H}_5\text{OH}$
R6	$\text{C}_2\text{H}_5\text{OPO}_2 = \text{HOPO}_2 + \text{C}_2\text{H}_4$
R7	$\text{PO}[\text{OH}]_2[\text{OET}] = \text{C}_2\text{H}_5\text{OPO}_2 + \text{H}_2\text{O}$
R8	$\text{H}_2 + \text{PO}_3 = \text{HOPO}_2 + \text{H}$

The TEP decomposition mechanism proposed in the literature[35, 53] and hence used in our previous kinetic model (Chapter 2) [51] consists of seven unimolecular decomposition reactions (R1 - R7 listed in Table 4-1) that take place via six-center (R1, R5, R6 and R7) and four-center (R2, R3, R4) concerted eliminations of ethylene or ethanol/water respectively. The rates of these reactions were estimated by Glaude et. al.[35] using Zegers and Fisher's [32, 53, 54] experimental measurements (within temperature range of 706-854 K) and analogy with ester decompositions. The first step (R1) of TEP decomposition is via six center elimination to form ethylene and diethyl phosphate ($\text{PO}[\text{OH}][\text{OET}]_2$). Hahn et. al.[43] used results of ab initio calculations to predict rates of this reaction within temperatures 570-2000 K using CVT/SCT (canonical variational transition state theory/ small-curvature tunneling) and VTST-ISPE/SCT (variational transition state theory with interpolated single-point energies) levels of theory. To the

best of our knowledge, rates of the remaining six four-center and six-center eliminations reactions have not been quantitatively investigated in the literature.

The calculated rates at CBS-QB3 level of theory were used in the TEP kinetic model proposed in Chapter 2 [51]. For TEP oxidation case, these reactions were not very sensitive to CO formation and to further improve CO prediction using the mechanism, we explored an alternative decomposition pathway for TEP decomposition via H-abstraction, radical decomposition and recombination reactions. Rates of H-abstraction reactions are much slower as compared to the molecular elimination reactions[55] and most of the TEP is expected to decompose through the predominant molecular elimination pathway. However, in the presence of radicals such as H, O etc. or in a fuel lean combustion cases with high concentration of O₂, H-abstraction pathways can play an important role in predicting intermediate species concentration. The effect of addition of this alternative decomposition pathway via H-abstraction at different temperatures is discussed using sensitivity, rate of production and reaction path analyses.

4.2 Methods

4.2.1 Computational Methods

All quantum chemical calculations were performed using Gaussian 09[56] at CBS-QB3 level of theory,[57] which includes transition state optimization at B3LYP/6-311G(2d,d,p) level. The transition states were confirmed to be the first-order saddle points by vibrational analysis. The intrinsic reaction coordinate (IRC) method[58] was used to verify these transition states are connected to the reactants and products of the respective reactions by the minimum energy pathways (MEP). The reaction rates were predicted with conventional transition state theory (TST)

and the rigid-rotor harmonic oscillator approximation, as implemented in Python script CanTherm.[59] Frequencies obtained at the B3LYP/6-311G(2d,d,p) level have been scaled by 0.99 in rate constant calculations.[60] Asymmetric Eckart tunneling corrections[61] were employed to compute the effect of 1-D tunneling through the barrier. This correction is determined using three parameters: (i) the imaginary frequency of the transition state, (ii) the barrier height and (iii) the reaction exothermicity.

4.2.2 Chemical Kinetic Mechanism

Decomposition of TEP via molecular elimination reactions (R1 to R7, listed in Table 4-2) has been described in detail in Chapter 2 and also in the literature[35, 53]. In current study, alternative decomposition pathway via H-abstraction reactions followed by radical decomposition and recombination have been added to construct an updated kinetic model for TEP decomposition. The reactions were based on di-isopropyl methyl phosphonate (DIMP) proposed by Glaude et al [55]. Thermochemistry of new species were calculated by group additivity method utilizing recently proposed group values from Khalfa et. al.[41] The details on thermochemistry calculation via group additivity method is provided in Chapter 2. Radicals (containing P=O), whose bond dissociation energies are not known, were estimated using analogy with C=O groups. Table 4-2 shows the computed thermochemical data of the new species added in this Chapter. Figure 4-4 shows the reactions involved in unimolecular decomposition of TEP as well as added H-abstraction, decomposition and recombination reactions. Similar sets of H-abstraction, decomposition and recombination reactions for TEP intermediate products: diethyl phosphate $\text{PO}[\text{OH}][\text{OET}]_2$, monomethyl phosphate $\text{PO}[\text{OH}]_2[\text{OET}]$ are also included in the proposed kinetic

mechanism. Species dictionary containing the structure of phosphorous species and corresponding names is listed in Appendix B. The mechanism file with complete reactions and thermochemistry in CHEMKIN formation can be found in supplementary information of our journal publication related to this work [62].

Table 4-2: Thermochemistry of new species calculated using group additivity method

Species	ΔH_f Kcal.mol ⁻²	S cal.mol ⁻¹ .K	Cp cal/mol.K					
			300K	400K	500K	600K	800K	1000K
PO[OET]2[OsC2H4]	-233.83	137.24	50.84	63.42	74.36	82.84	94.19	102.39
PO[OET]2[OpC2H4]	-227.69	138.93	50.53	62.39	73.02	81.52	93.24	101.73
PO[OET]2O	-228.07	140.06	51.46	63.26	73.83	82.23	93.76	102.14
PO[OET]2	-223.92	134.71	52.19	63.43	74.05	82.56	94.43	103.01
PO[OH][OET][OsC2H4]	-233.45	119.58	41.57	51.35	59.50	65.62	73.54	79.05
PO[OH][OET][OpC2H4]	-227.31	121.27	41.26	50.32	58.16	64.30	72.59	78.39
PO[OH][OET]O	-227.69	122.41	42.19	51.19	58.97	65.01	73.11	78.80
PO[OH][OET]	-223.54	118.43	42.92	51.36	59.19	65.34	73.78	79.67
PO[OH]2[OsC2H4]	-231.47	101.93	32.30	39.28	44.64	48.40	52.89	55.71
PO[OH]2[OpC2H4]	-225.33	103.61	31.99	38.25	43.30	47.08	51.94	55.05
PO[OH]2O	-203.09	78.69	21.58	23.83	25.66	27.14	29.28	30.63

Not a lot is known about the kinetics of these phosphorous reactions and hence rate coefficients were estimated based on analogy with similar reactions in the literature. TEP has three CH₃ groups in β -site and three CH₂ groups in α -site. Rate constants for abstraction of H-atoms were determined by analogy with H-atom abstraction from primary and tertiary sites in DIMP, respectively with some modifications noted below. A-factor of the abstraction reactions were scaled according to the number of abstractable H-atoms and activation energies were corrected based on Evans-Polanyi principle proposed by Dean and Bozzelli[63]. For example, abstractable H-atoms in primary site of DIMP is 12 and that of TEP is 9. Hence, for primary H-abstraction reactions, A-factors of corresponding reactions were scaled by a factor of 0.75. Rate constants of decomposition and recombination reactions were assumed to be same as those of similar reactions in diisopropyl methyl phosphonate (DIMP), trimethyl phosphate (TMP) and diethyl carbonate (DEC) kinetic mechanisms[55].

Table 4-3: Experiments conditions – CO time-history measurement during TEP combustion in shock tube[51] from our prior work

Experiment	Mixture composition	Temperature (K)	Pressure (atm)
Pyrolysis	TEP = 0.247%; Ar =99.759%	1673	1.374
		1590	1.355
		1462	1.473
Oxidation	TEP = 0.038%; O2 = 3.381%; Ar=96.581%	1437	1.269
		1508	1.17
	TEP = 0.0757%; O2=9.105%; Ar= 90.8193%	1213	1.424
		1387	1.329

In addition, the new TEP chemical kinetic model is compared with data from Mathieu et al[65], who recently published shock tube ignition delay times for TEP combustion within 1100 to 2100 K and near 1.5 atm. The experiments were conducted at three equivalence ratios: 0.5, 1 and 2. Neat mixtures (TEP, Ar and O2) and hydrogen and methane mixtures seeded with TEP were investigated. The reported ignition times based on peak or maximum rising slope of the measured OH* signals are compared with corresponding model prediction results. Further, sensitivity and rates of production (ROP) analyses are carried out to explain the discrepancies between the measured and predicted values.

4.3 Results

4.3.1 Quantum Chemical and Kinetics Calculations

The structures of the transition states were optimized at B3LYP/6-311G(2d,d,p) theory level and their ball-and-stick models are shown on Figure 4-5. Four of the reactions considered

(R1, R2, R4, R6) present elimination of ethylene from $\text{PO}[\text{OET}]_3$, $\text{PO}[\text{OH}][\text{OET}]_2$, $\text{PO}[\text{OH}]_2[\text{OET}]$, and $\text{C}_2\text{H}_5\text{OPO}_2$ respectively. They correspond to intramolecular hydrogen transfer from the β -carbon atom of the ethoxy group to the terminal oxygen atom via six-membered ring transition states. Alternative mechanisms with hydrogen transfer to the oxygen of the same ethoxy group via four-membered ring transition states had considerably higher energy barrier due to the ring strain and were neglected. Elimination of ethanol (R3, R5) from $\text{PO}[\text{OH}][\text{OET}]_2$, and $\text{PO}[\text{OH}]_2[\text{OET}]$ respectively proceeds by hydrogen transfer from hydroxyl to the oxygen of the ethoxy group via four-membered ring transition states. Similar four-member ring transition state is observed in reaction of water elimination (R7) from $\text{PO}[\text{OH}]_2[\text{OET}]$. It is taking place by hydrogen transfer from one hydroxyl group to another oxygen. Finally, intermolecular hydrogen abstraction from H_2 molecule by PO_3 radical (R8) has a linear transition state.

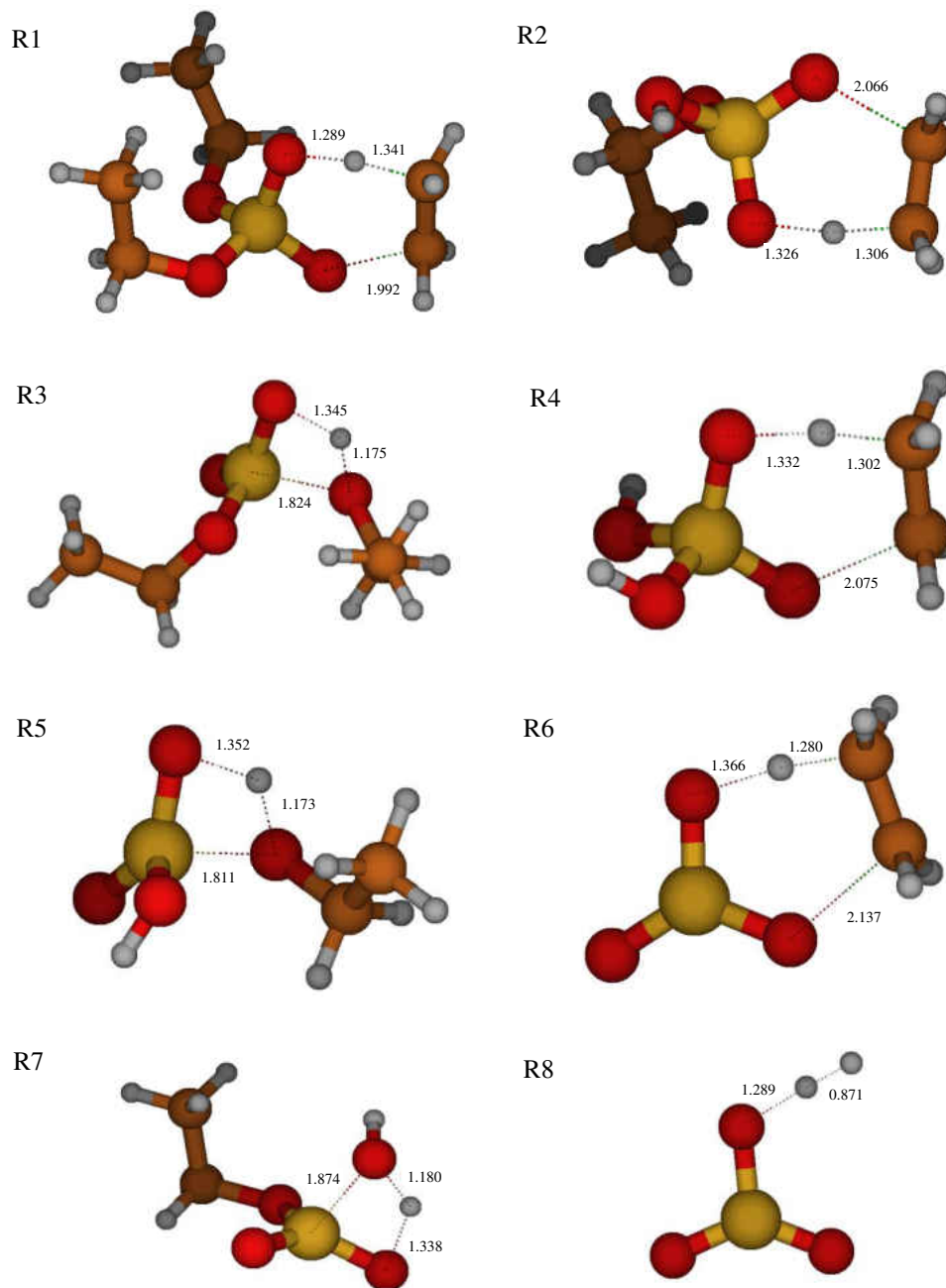


Figure 4-5: Structure of the Transition states for all reactions considered here. Dotted lines denote the chemical bonds being broken and formed, the bond lengths (\AA) are also shown.

The theoretical Arrhenius parameters of each reaction, obtained with TST, are compared with the literature values in Table 4-4, and predicted rate constants are compared in Table 4-5. The computed A-factors of all eight reaction were lower than estimated values in the literature by factor of 1.01 to ~ 50. The calculated activation energies of these reactions were 6-14% lower than Glaude et al.[35] estimations. The activation energy for R8, which involves intermolecular hydrogen abstraction from H₂ molecule by PO₃ radical by forming a linear transition state is calculated to be 16.890 kcal/mol. Table 4-5 compares the rates of all eight reactions within 1000 – 2000K.

Table 4-4: The Arrhenius expression for the rate constants calculated at CBS-QB3 level of theory (present work) and estimated by Glaude et. al.[35] Activation energy (E_a): kcal/mol.

RXN #	RXN	Glaude et. al.		CBS QB3 (Arrhenius)		CBS QB3 (Modified Arrhenius)		
		A	E _a	A	E _a	A	n	E _a
R1	PO[OET]3=PO[OH][OET]2+C2H4	2.8E+13	45.30	3.3E+12	41.51	4.8E+03	2.73	38.51
R2	PO[OH][OET]2=PO[OH]2[OET]+C2H4	1.9E+13	45.30	3.7E+12	42.11	2.8E+05	2.20	39.69
R3	PO[OH][OET]2=C2H5OPO2+C2H5OH	2.5E+13	44.00	4.1E+12	40.96	7.5E+07	1.36	37.50
R4	PO[OH]2[OET] = PO[OH]3+C2H4	9.6E+12	45.30	9.5E+12	42.12	1.2E+06	2.14	39.78
R5	PO[OH]2[OET]=HOPO2+C2H5OH	2.5E+13	44.00	1.3E+12	40.21	1.1E+06	1.87	38.16
R6	C2H5OPO2 = HOPO2+C2H4	1.9E+13	45.30	1.1E+13	38.67	4.4E+07	1.67	36.84
R7	PO[OH]2[OET]=C2H5OPO2+H2O	5E+13	45.00	9.8E+11	41.98	2.2E+05	2.05	39.73
R8	H2+PO3=HOPO2+H	2E+12	0.00	7.0E+11	16.89	2.4E+07	1.38	15.38

Table 4-5: Comparison of reaction rates (CBS-QB3 calculations vs. Glaude et. al. estimation) at 1000, 1500 and 2000 K. Unit of k : R1 to R7 = s⁻¹; R8 = cm³mol⁻¹s⁻¹

^aCBS-QB3 – present work; ^bGlaude et al[35]

Rxn #	k (T=1000K)			k (T=1500K)			k (T=2000K)		
	CBS-QB3	Glaude et. al.	ka/kb	CBS-QB3	Glaude et. al.	ka/kb	CBS-QB3	Glaude et. al.	ka/kb
1	3.16E+03	3.52E+03	0.90	5.06E+06	7.03E+06	0.72	3.03E+08	3.14E+08	0.96
2	2.56E+03	2.39E+03	1.07	4.27E+06	4.77E+06	0.90	2.36E+08	2.13E+08	1.11
3	5.74E+03	6.05E+03	0.95	5.38E+06	9.70E+06	0.55	1.85E+08	3.89E+08	0.48
4	6.44E+03	1.21E+03	5.34	1.07E+07	2.41E+06	4.44	6.05E+08	1.08E+08	5.62
5	2.25E+03	6.05E+03	0.37	2.51E+06	9.70E+06	0.26	1.10E+08	3.89E+08	0.28
6	4.17E+04	2.39E+03	17.46	3.68E+07	4.77E+06	7.72	1.34E+09	2.13E+08	6.28
7	7.29E+02	7.31E+03	0.10	1.11E+06	1.39E+07	0.08	5.94E+07	6.05E+08	0.10
8	1.51E+08	2.00E+12	0.00	3.19E+09	2.00E+12	0.00	1.78E+10	2.00E+12	0.01

4.3.2 Comparison of Experimental Data in Literature with Model Predictions

4.3.2.1 CO Time-histories Measured in Shock Tube

Plots in Figure 4-6 show the experimental CO time-histories during TEP pyrolysis and oxidation taken from our Chapter 2 and model predictions. The green dotted lines represent predictions using TEP kinetic model proposed in Chapter 2. This model contains the most up-to-date hydrocarbon chemistry (from AramcoMech2.0) and updated thermochemistry of phosphorous species. The TEP sub-mechanism in this model consists of seven molecular elimination reactions (R1 - R7 in Table 4-4) proposed by Glaude et al[35] and Zegers and Fisher[53] for decomposition of TEP during its pyrolysis. The red dashed lines are the CO predictions by TEP kinetic model proposed in this Chapter. In this model, the rate coefficients of the pyrolysis reactions (R1 - R7) are updated using calculated rates from CBS-QB3 (Table 4-4). In addition, alternative TEP decomposition pathway via H-abstraction, radical decomposition and molecular elimination reactions (Figure 4-4) are included. For TEP pyrolysis (Figure 4-6, a-c),

the current model predicts higher CO yield and for TEP oxidation (Figure 4-6, d-g), CO formation rate predicted by the present model is faster. Overall, better agreement with the literature experimental data is obtained from the new mechanism.

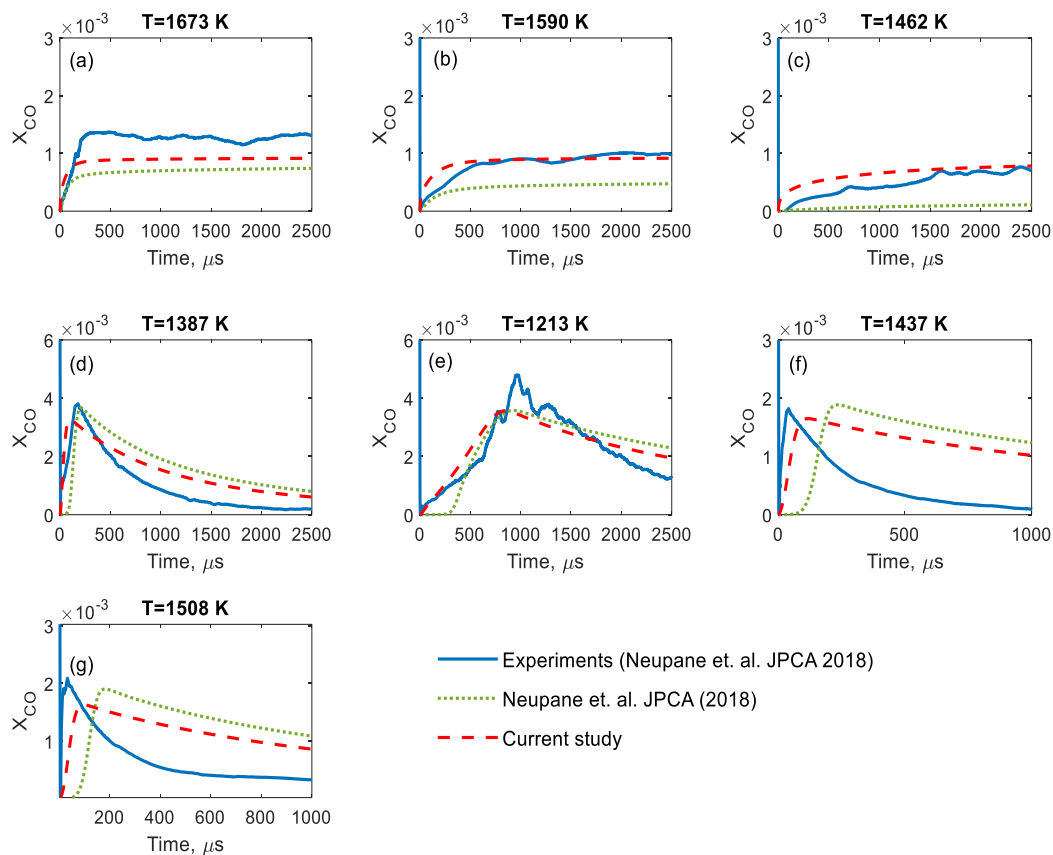


Figure 4-6: Experimental and predicted CO yield during TEP pyrolysis (a-c) and oxidation (d-g)

Sensitive reactions to CO formation

In order to understand CO formation during TEP pyrolysis and oxidation, sensitivity analyses (defined in eqn. 1) were performed using the proposed mechanism. The results for TEP pyrolysis (0.25% TEP in Ar; $T = 1462\text{ K}$ and $P = 1.473\text{ atm}$) and TEP oxidation (0.03% TEP in Ar; $\phi = 0.075$; $T = 1213\text{ K}$ and $P = 1.424\text{ atm}$) are shown in Figure 4-7. The first reaction is the six-

center elimination reaction of parent TEP molecule to form ethylene and diethyl phosphate (R1). At high temperatures (conditions studied here), the rate of this reaction is very fast and thus proceeds rapidly as compared to any H-abstraction reactions. As seen in Figure 4-7, CO formation has very high sensitivity to this reaction near time zero. The sensitivity is reduced to zero after ~20 μ s for TEP pyrolysis at 1462 K, this is when all TEP has decomposed into PO[OH][OET]₂ and C₂H₄.

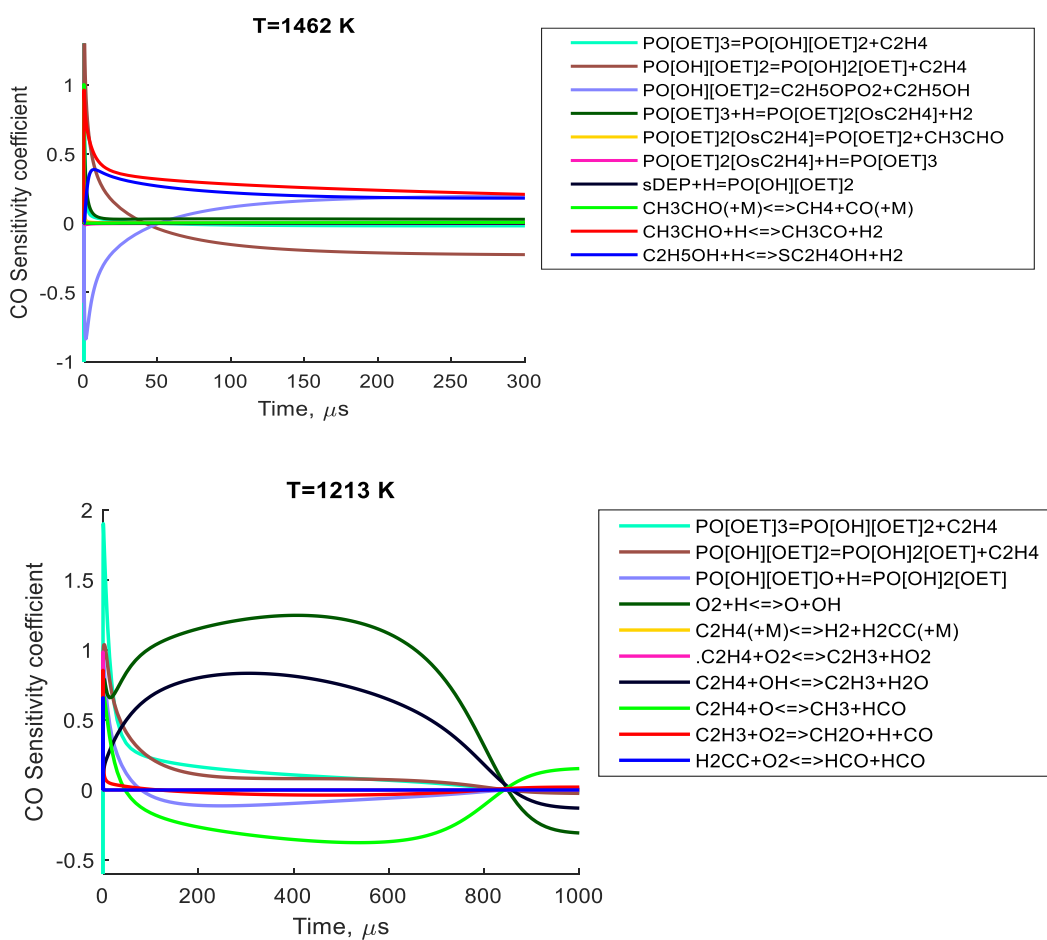
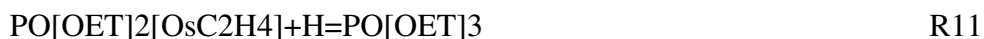
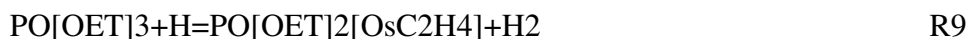


Figure 4-7: CO sensitivity analysis for TEP pyrolysis (1462 K) and b. TEP oxidation (1213 K) using the proposed kinetic model.

Diethyl phosphate (which is a direct product from six-center elimination of TEP) decomposition has three possible pathways: six-center molecular elimination of ethylene (R2); four-center molecular elimination of ethanol (R3) and via H-abstraction reactions. Both R2 and R3 are highly sensitive to CO formation during TEP pyrolysis. The rates of these reactions are very important in determining the ratio of ethanol to ethylene formed during TEP decomposition. Since CO formation pathway during TEP pyrolysis is via formation of ethylene or ethanol[51], the rates of these reaction show very high sensitivity to CO yield. Also, from ROP analyses of TEP (Figure 4-8), it was found that virtually 100% of TEP decomposes via molecular elimination pathway and H-abstraction channel does not play an important role in initial TEP decomposition (Figure 4-8). However, appearance of H-abstraction reaction (R9) of TEP by H-atom to form PO[OET]2[OsC2H4], radical decomposition reaction (R10) and recombination reaction (R11) in the top sensitive reactions show the importance of this pathway to accurately predict the intermediate product concentration during TEP pyrolysis. Further analyses on effect of addition of H-abstraction pathway in TEP mechanism is given in Section 4.



For oxidation, CO formation was found to be sensitive to six center elimination reactions (R1 and R2) that forms C₂H₄ and the subsequent C₂H₄ chemistry (Figure 4-7). At lower temperature (1213K), radicals recombination reaction as a result of H-abstractions was also among the sensitive reactions, while at higher temperatures, this reaction is not sensitive.

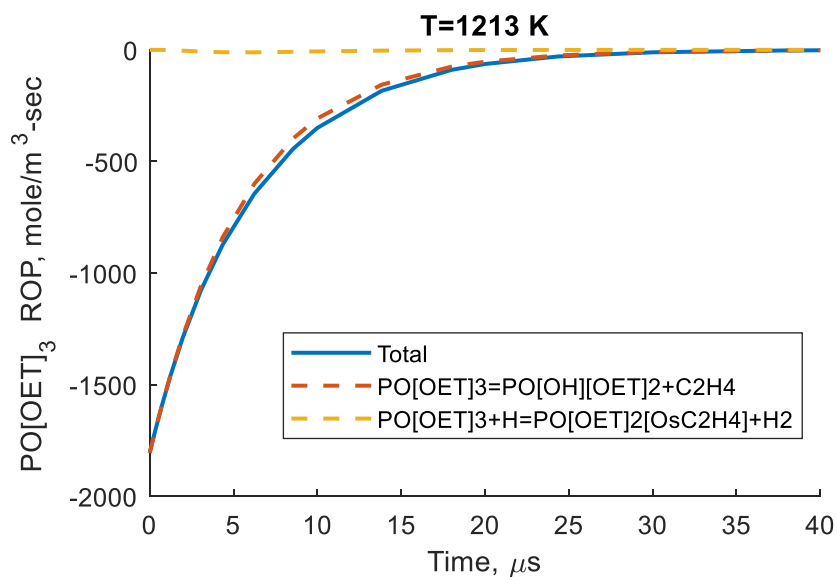


Figure 4-8: ROP analysis of TEP oxidation at 1213 K

4.3.2.2 Ignition Times Measured in Shock Tube

The proposed kinetic model was used to predict OH time-histories during TEP combustion at conditions reported by Mathieu et al[65]. The simulated OH profiles showed a two-stage ignition behavior (Figure 4-9). However, no such behavior was reported by Mathieu et al[65] in their shock tube study of TEP ignition. The model predicts the first stage rise time to be very fast (within 20 μ s) for the range of temperatures studied and in fuel lean and stoichiometric conditions, the first stage ignitions are weak. In Mathieu et al[65] study, for neat TEP mixture, ignition times based on peak OH* signals (τ_{\max}) are reported and for CH₄ and H₂ mixtures seeded with TEP, ignition delay times corresponding to maximum positive slope in OH* (τ_{ign}) signals are reported. To calculate ignition delay time using the proposed kinetic model, we used corresponding peak and maximum slope of predicted OH time-histories as shown in Figure 4-9.

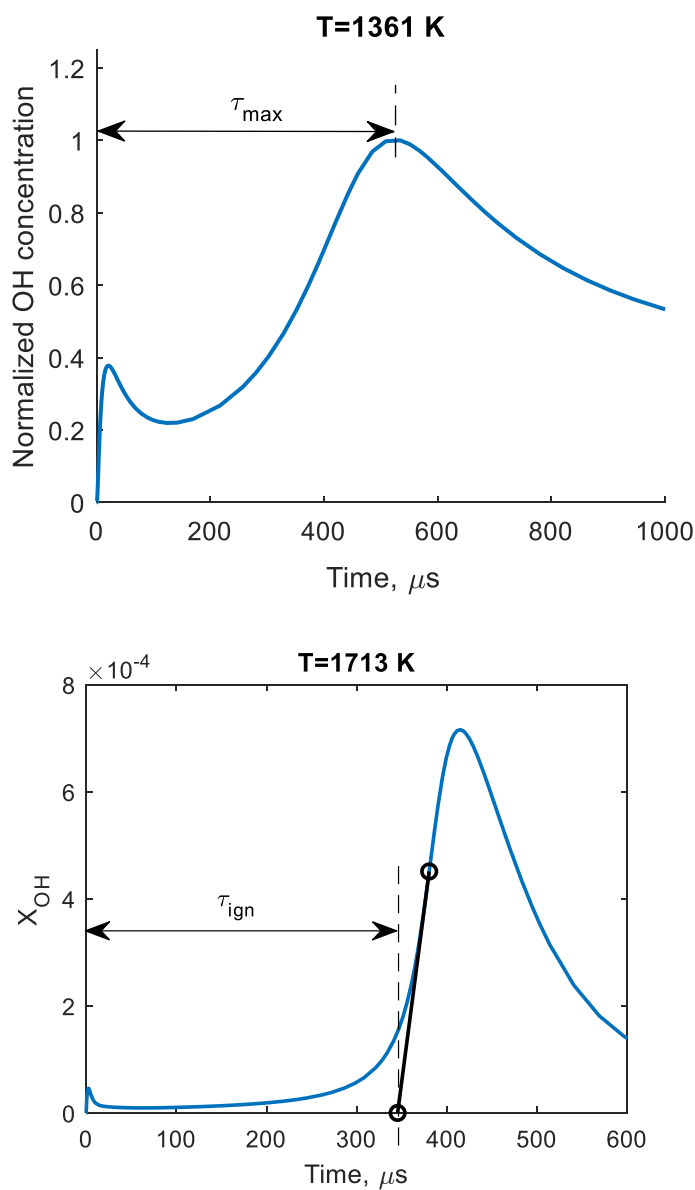


Figure 4-9: Ignition time calculation from predicted OH profile. OH profiles are simulated using proposed TEP mechanism showing two stage ignition

As seen in Figure 4-10 (a), predicted ignition delay time for rich TEP mixture ($\phi=2$) is in very good agreement with the experiments data. For stoichiometric mixture, fairly good agreement with experiments is observed. However, for lean mixture, the predicted ignition times are faster than the experiment. Model predictions show a clear trend of increasing ignition delay time with

equivalence ratio. However, no significant difference in ignition times for stoichiometric and lean mixtures were observed from the experiments. Similarly, Figure 4-10 (b) and (c) show the measured and predicted ignition delay times of H₂ and CH₄ mixtures seeded with 1% TEP. For H₂ mixture, while the model deviates from experiment at extreme temperatures (1132 K and 1522 K), fairly good agreement is obtained within temperature 1210 to 1425 K. However, for CH₄ mixture, the predicted ignition times is significantly lower than experiments at all three equivalence ratios.

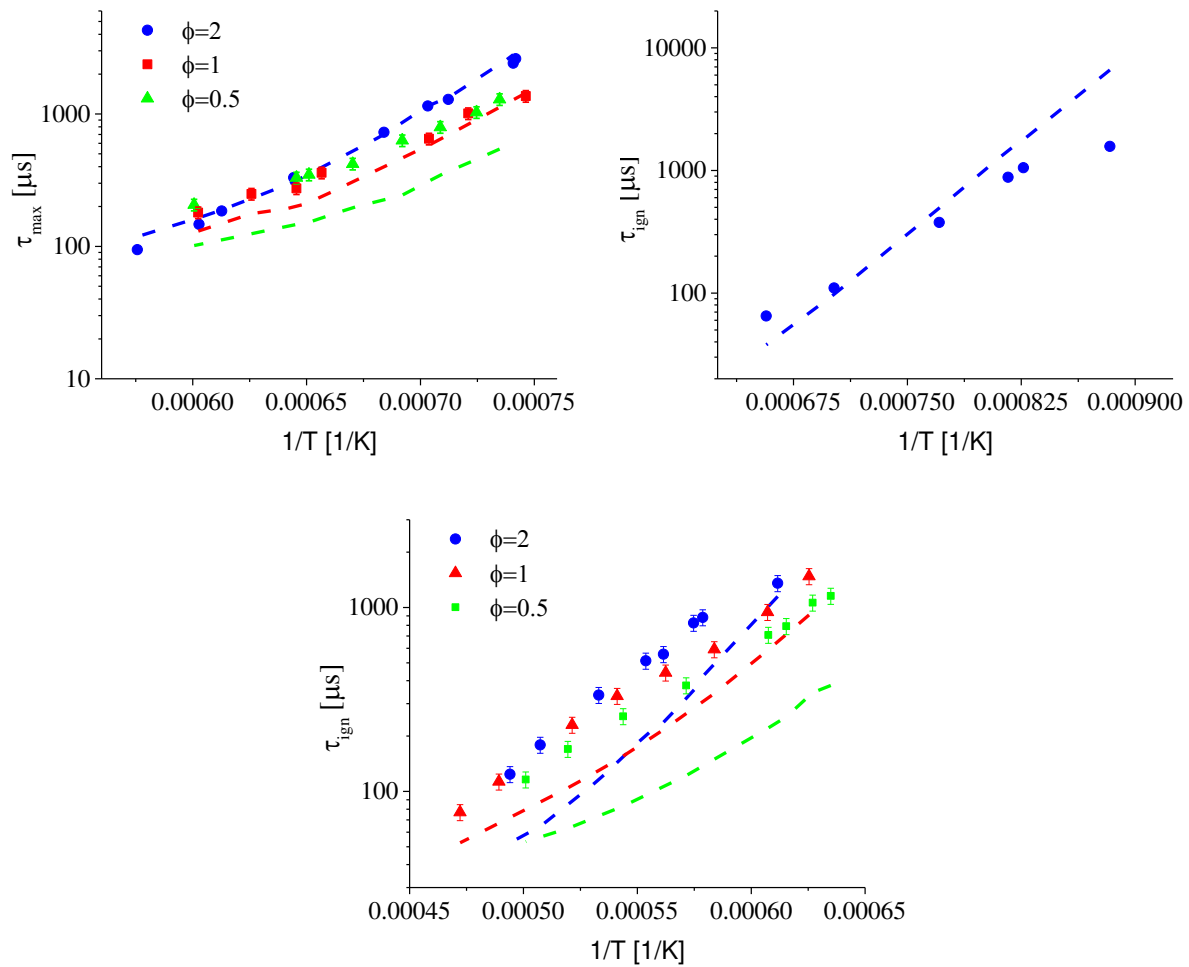


Figure 4-10: Ignition times comparison: experiments results by Mathieu et al (symbols) and model prediction (dashed lines)

Brute force sensitivity analyses of ignition delay time

Brute force sensitivity analysis of important reactions was carried out to further understand their effects on ignition delay time prediction and the results obtained are plotted in Figure 4-11. As evident from Figure 4-9, two-stage ignitions were observed for TEP. Thus, sensitivity analysis was carried out for first stage (Figure 4-11 (a)) and second stage ignition (Figure 4-11 (b)). The results of the brute force sensitivity analysis show that Reactions R2 and R3 have the highest sensitivity coefficients for the first stage ignition while the reaction “ $\text{O}_2 + \text{H} \rightleftharpoons \text{O} + \text{OH}$ ” has the highest sensitivity coefficient for the second stage ignition times. This indicates that first stage ignition is dominated by TEP decomposition reactions while second stage ignition was less sensitive to TEP decomposition reactions. For example, Reaction R1, the first step in TEP decomposition mechanism, showed a very low sensitivity coefficient to second stage ignition delay time at stoichiometric condition. Changing the rate of this reaction by a factor of two did not affect ignition delay time of TEP in rich and lean conditions.

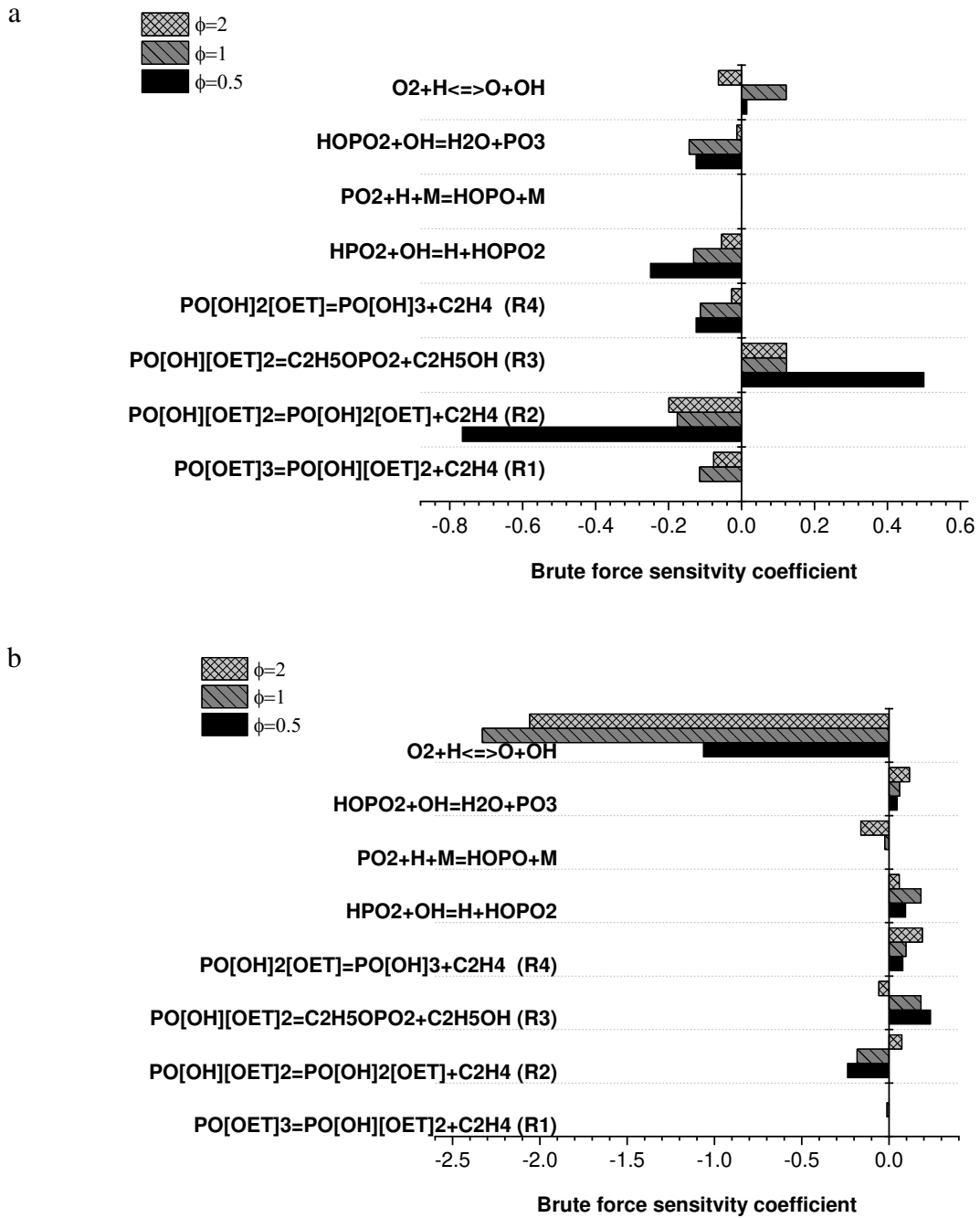


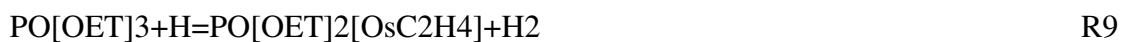
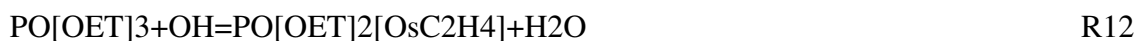
Figure 4-11: Brute force sensitivity analysis (absolute) of important reactions to ignition times for a) first stage and b) second stage.

Among the phosphorous reactions, reactions R2 and R3 show the highest brute force sensitivity coefficients for second ignition. The magnitude of sensitivity coefficient of these reactions is equal and in opposite direction to each other. Note that negative sensitivity means decreasing ignition delay time i.e. reaction promoting activity. For lean and stoichiometric conditions, R3, the four-center elimination reaction that forms C_2H_5OH showed positive sensitivity while the reaction R2 which involves elimination of C_2H_4 showed negative sensitivity. This trend was opposite for the rich mixture ($\phi=2$). Also, the absolute sensitivity coefficients of these reactions to ignition times decreased with increase in equivalence ratio. On the other hand, the sensitivity coefficient of reaction R4 involving decomposition of monoethyl phosphate ($PO[OH]_2[OET]$) to form C_2H_4 increased with increase in equivalence ratio. Reactions involving smaller phosphorous species such as $HOPO_2$, $HOPO$ and PO_2 were also among the sensitive reactions that significantly affects the ignition delay times of TEP.

4.4 Effect of Addition of H-abstraction Pathway

To understand the effects of H-abstraction pathway added in this work, the reaction pathway analyses were carried out using a 0-D closed homogeneous reactor simulation within the temperature range of 1200-1800 K for two cases, a) 0.1% TEP pyrolysis in N_2 bath gas b) 0.1% TEP oxidation, 1% each of O_2 , H, OH and balance N_2 . Former case helps in understanding the important reactions involved in TEP decomposition while latter helps in understanding the role of H, OH and O_2 in TEP decomposition. Kinetic model with only TEP sub-mechanism was used for this purpose. This provides a better understanding of the decomposition pathways by isolating the effects of hydrocarbon reactions and smaller phosphorous species reactions. Figure 4-12 shows

the concentration profiles of species PO[OET]₃, PO[OH][OET]₂ and C₂H₅OPO₂ for a residence time of about 10s. Here, TEP pyrolysis (case (a)) is shown by dotted lines while the solid lines show the TEP oxidation mixture in case (b). In general, TEP decomposition is highly sensitive to temperature and undergoes six-center molecular elimination to form PO[OH][OET]₂ and C₂H₄ (reaction R1). However, it can be observed that TEP decomposition is faster at low temperature (1200K) for mixture containing H, OH and O₂. This can be attributed to H-abstraction reactions of TEP with H or OH to form PO[OET]₂[OsC₂H₄] or PO[OET]₂[OpC₂H₄] along with H₂ or H₂O respectively. These reactions are shown below in the decreasing order of their influence on TEP decomposition.



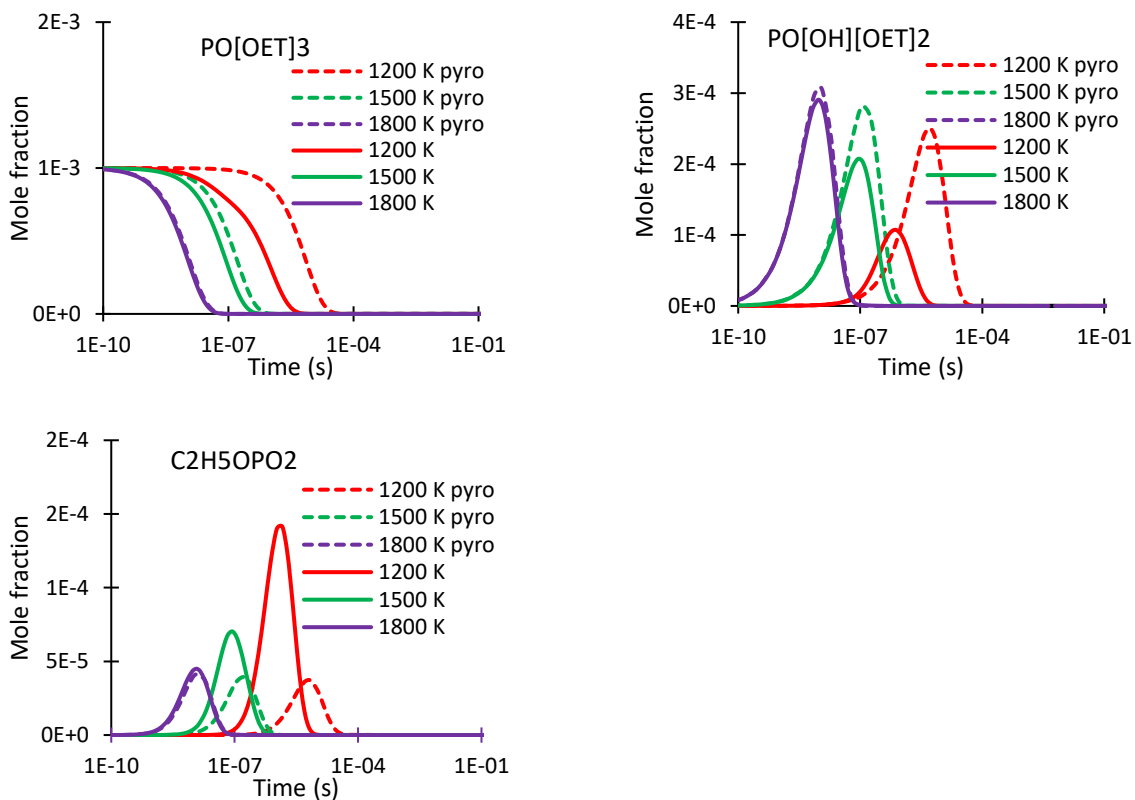
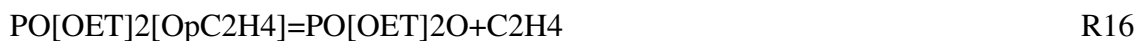


Figure 4-12: Mole fraction vs time plot for important intermediates in TEP decomposition in a 0-D closed homogeneous reactor for a pyrolysis feed (0.1 mol% TEP and balance N₂) and a simplified feed containing 0.1 mol % TEP, 1 mol % each of O₂, H, OH and balance N₂.

PO[OET]₂[OsC₂H₄], formed from reactions R12 and R9, decomposes to PO[OET]₂ which then forms C₂H₅OPO₂ as shown in reactions R10 and R15. This explains the increased formation of C₂H₅OPO₂ in oxidation mixture case (b) as compared to the pyrolysis mixture case (a) in Figure 4-12. PO[OET]₂[OpC₂H₄] decomposes to PO[OET]₂O, which undergoes H addition to form PO[OH][OET]₂ as shown in reaction R16 and R17:

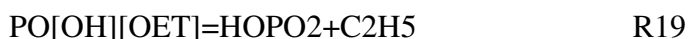




At high temperature, TEP decomposition reaction via molecular elimination of C₂H₄ (R1) dominates over H-abstraction reactions R9, R12-14. Hence the contribution of H-abstraction reactions by H and OH are insignificant at high temperatures, which explains the overlapping of TEP profiles at 1800K in both the cases.

Figure 4-12 indicates an increased formation of the intermediate product PO[OH][OET]₂ with temperature for both the cases. At 1200 K, the lower peak concentration for oxidation mixture compared to the pyrolysis mixture is because of H-abstraction pathway. Due to the formation of PO[OET]₂[OsC₂H₄] in reactions R12 and R9, less TEP is available for dissociation via molecular elimination reaction R1. As the temperature increases, PO[OH][OET]₂ concentration profile in oxidation case moves closer to the pyrolysis case indicating that H-abstraction pathway has decreased role at higher temperatures.

Figure 4-13 shows the major H-abstraction reaction products in the TEP dissociation pathway. It can be seen that all species except sDEP have concentrations above 1E-8 and hence can have a direct impact on the overall pathway. For sDEP, the reaction R18 is very fast in the reverse direction and decomposes to PO[OH][OET] rapidly which forms HOPO and HOPO₂ as per reactions R19 and R20. The trend on these species profiles also confirms that the role of H-abstraction reactions and its products decreases with increase in temperature.



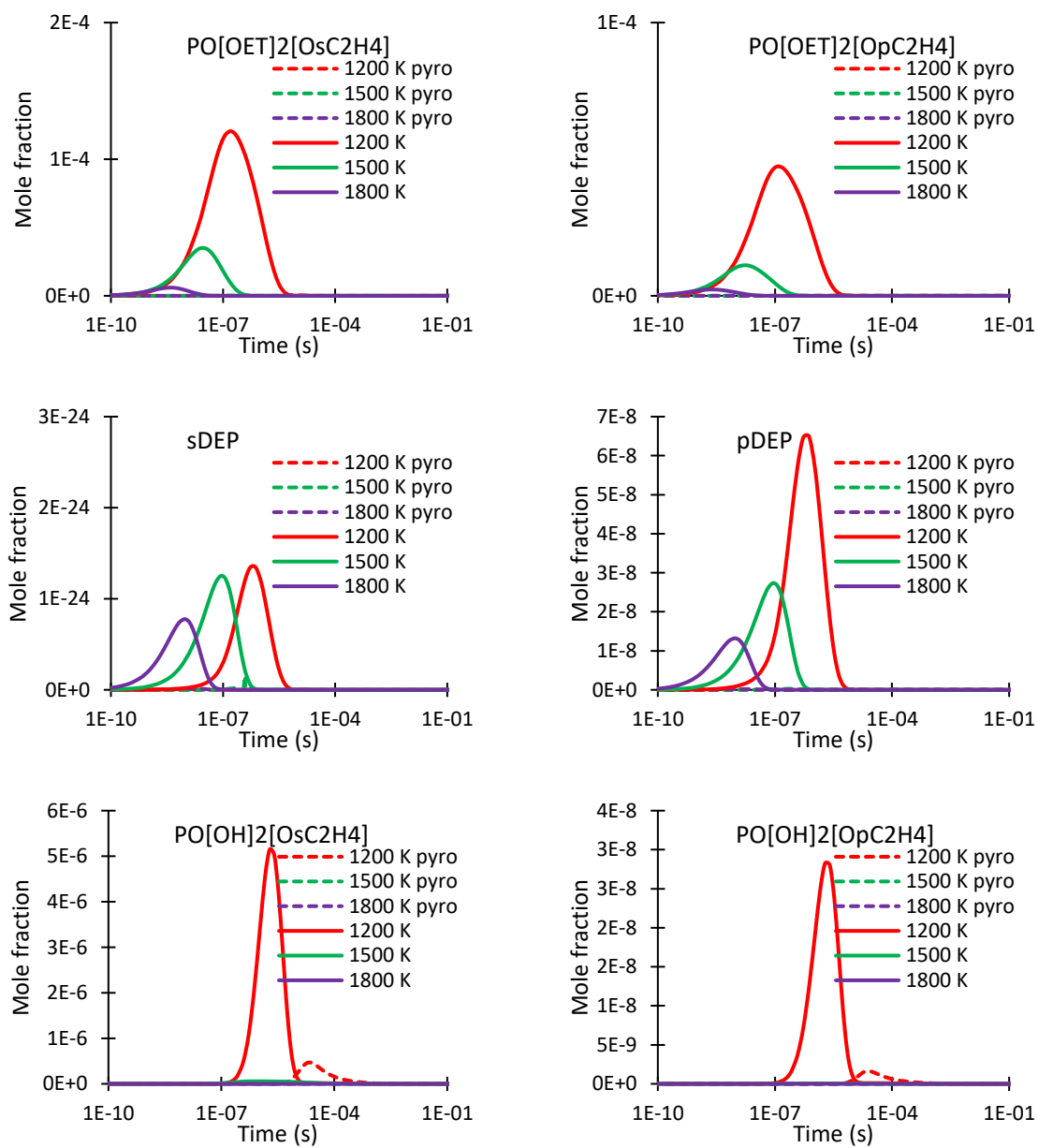


Figure 4-13: Plots showing profiles of H- abstraction reaction products in the TEP decomposition pathway.

Figure 4-14 displays the profiles of H, O₂ and OH atoms for the case (b) mixture. It can be observed that both H and OH atoms were consumed in considerable amount at 1200 K emphasizing the importance of H-abstraction reactions at low temperatures. However, O₂ profile maintains a constant trend indicating that neither H-abstraction nor oxidation of TEP or its intermediates takes place directly by O₂ molecules.

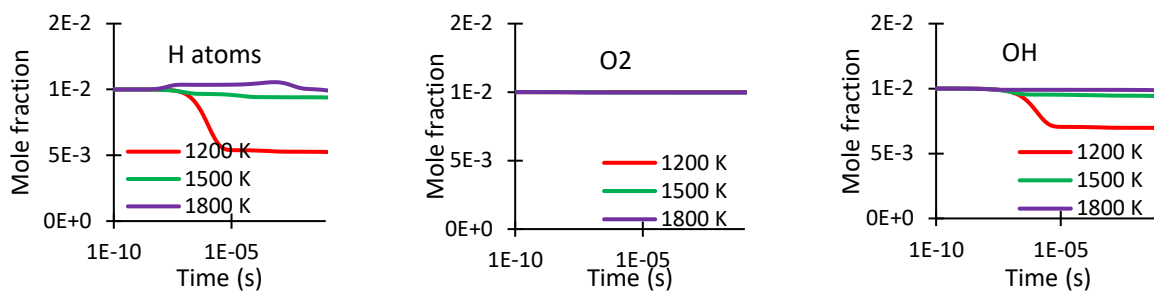


Figure 4-14: Plot showing the profiles of H, O₂ and OH for 0-D closed homogenous reactor simulation for a mixture containing 0.1 mol % TEP, 1 mol % each of O₂, H, OH and balance N₂.

4.5 Conclusions

This Chapter presents an improved TEP combustion chemical kinetic model. Reaction rates of seven molecular elimination reactions in TEP sub-mechanism were updated using CBS-QB3 quantum chemical theory level. Alternative TEP decomposition pathway via H-abstraction, radical decomposition and recombination reactions are added. The model was used to predict CO time histories during TEP pyrolysis and oxidation within 1400-1700 K and near 1.4 atm. The experimental data were adapted from our recent shock tube study of TEP combustion[51]. The predicted CO profiles using the proposed model are in better agreement with the experiments. The model is also used to simulate shock tube ignition delay time data[65] and fair agreement was obtained for rich ($\phi = 2$) mixture. However, for lean and stoichiometric cases deviation from the experiments were larger. Reaction path and ROP analyses showed that the H-abstraction pathway

plays an important role only at low temperature while at high temperatures, the molecular elimination pathway remains predominant. The molecular elimination reactions are very fast compared to any H-abstraction reactions at high temperature, hence most of the TEP decomposition proceeds via this pathway. The newly calculated reaction rates, discussions on results of sensitivity and reaction path analysis presented in this Chapter will be critical in development of more comprehensive detailed mechanism for TEP combustion.

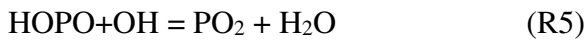
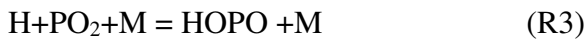
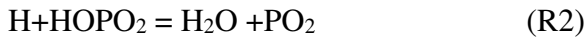
CHAPTER 5: CO TIME-HISTORIES MEASUREMENTS DURING DMMP PYROLYSIS AND OXIDATION IN SHOCK TUBE

5.1 Introduction

Montreal protocol in 1990s prohibited the use of halons as fire suppressants due to their damaging effect on ozone layer[1]. Since then, phosphorous containing compounds such as dimethyl methyl phosphonate (DMMP) and tri-methyl phosphate (TMP) have been identified as replacements of halons in fire suppressants. When used in gas-phase as dopants, these organo-phosphorous compounds (OPCs) interfere with normal combustion reactions to effectively reduce flame speed of hydrogen and hydrocarbon fuels[2]. OPCs are also used as chemical warfare agents (CWA) for example Sarin, GB and VX. Structure of DMMP is similar to that of nerve agent Sarin, GB and hence used as simulant to study combustion behavior of the toxic nerve agent. The most effective way to destroy chemical weapons is by thermal means, i.e. incineration in an enclosed reactor or by utilizing tailored explosives. It is important to understand combustion chemistry of these compounds to be able to accurately predict their performance as fire suppressants and CW simulants.

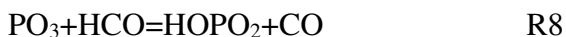
Most of the past studies on DMMP combustion have been focused on its influence as an additive in transformation, structure and propagation of hydrogen and hydrocarbon flames[2, 28, 30, 47, 66-68]. DMMP when used as an additive, changes the concentration of the most reactive radicals (H, O and OH) in the flame thereby producing promoting or retarding effects. Due to large hydrocarbon moiety of DMMP, it has been found that at fuel lean conditions addition of DMMP increases the burning velocity[30]. While at stoichiometric and rich conditions, DMMP is known to be very effective in suppressing flames, about 4 to 6 times more effective than bromine – a

common halon fire suppressant[2, 30]. Twarowski investigated the inhibition effect of phosphorous containing compounds (described by reactions R1-R5) by studying the reactions of phosphine addition to water[69]. Smaller phosphorus species PO₂, HOPO and HOPO₂ formed because of DMMP breakdown provide an alternative pathway for recombination of H and O atoms thereby reducing their concentration in the reaction zone. These reactions are chain terminating reactions and play an important role in driving the radicals to their equilibrium values[28, 30, 68]. However, in fuel lean conditions, large hydrocarbon moiety of DMMP causes concentration of H and OH radicals in flame to increase and hence there is little effect of the alternative radical combination pathway[30] responsible for producing the inhibition effects.



Werner and Cool[70] developed the first kinetic model for the decomposition of DMMP in a hydrogen/oxygen flame. They created a 19 step mechanism which was based on Twarowski[69] mechanism for small phosphorus reactions, ab-initio estimates of thermochemistry calculation and experimental data obtained from laser-ionization mass spectrometry. Korobeinichev et al[47] added nine reactions and several intermediates to include 18 species and 41 reactions. The same group (Korobeinichev et al 2004[27] and Jayaweera et al 2005[28]) further updated the model with more accurate ab-initio thermochemistry estimation of small phosphorous species and reaction rate of one of the important inhibition reactions (R2). The model was validated

using species concentration profiles and laminar burning velocities for phosphorous doped premixed propane/air flame at different equivalence ratios. More recently, Babushok et al[30] employed GriMech3.0[71] and Jayaweera et al[28] mechanism along with three additional phosphorous reactions (R6 - R8) to describe DMMP combustion in lean propane flames. A more comprehensive model was independently developed by Glaude et al[72] in the early 2000s for DMMP and tri-methyl phosphate (TMP) decomposition, that attempted to account for all possible DMMP reaction pathways with 41 phosphorus species and 202 phosphorus reactions.



As understood from the literature review, kinetic mechanism development and validation for DMMP has been focused on premixed flame experiments to investigate the effects of DMMP doping in hydrocarbon (CH_4 and C_3H_8) and H_2 flames. Recently, Mathieu et al[73] measured ignition delay times of DMMP in a shock tube. DMMP in O_2 and Ar mixtures (fuel lean conditions) and DMMP doped in H_2 , CH_4 and C_2H_4 mixtures were investigated near 1.5atm and $T = 1055\text{-}2010\text{K}$. The experimental results were compared with model prediction using Babushok 2016[30] and Jayaweera 2005[28] mechanisms and the need for significant improvement in both the models was identified. The authors stressed the importance of more experimental data such as species time histories of intermediate products in further improving and tuning of the kinetic models. A mechanism incorporating detailed chemistry which includes unimolecular decomposition of DMMP in pyrolytic conditions along with radical interactions and reactions with O and OH at fuel lean conditions is critical to accurately predict its destruction process. In addition, it is necessary

to validate the kinetic model using high fidelity experimental data acquired at a range of equivalence ratios and temperature conditions. Once an accurate model of simulant such as DMMP has been developed using theoretical and experimental techniques, the model can be extrapolated to predict combustion behavior of CW simulants.

In present work, we utilized laser absorption spectroscopy to measure intermediate CO concentration time histories behind reflected shock waves during pyrolysis and oxidation (lean, stoichiometric and rich conditions) of DMMP. Since CO is the major intermediate during DMMP combustion, the experiments data provide an important kinetic target for model validation. Experimental results were compared with model predictions using Babushok[30] mechanism and a tentative kinetic model (based on AramcoMech2.0 and LLNL OPC incineration mechanism) which was recently developed by our group and validated for triethyl phosphate combustion[51]. Further analysis on the results of sensitivity analysis and reaction pathways of DMMP decomposition is provided and future work on DMMP kinetic model improvement is discussed.

5.2 Experimental methods

5.2.1 Fuel/oxidizer Mixture Preparation

Research grade DMMP (> 97% pure; Acros Organics) and gases (O₂, Ar > 99.999% purity; nexAir) were used to prepare the test gas mixtures. The mixtures were prepared monometrically and the method is similar to that described in our previous work on low vapor pressure compounds[51]. DMMP has a low vapor pressure of ~0.8Torr at 25°C[23] and tend to condense and adhere on the surface of the mixing tank and transfer lines. To prevent condensation, the mixing facility and transfer lines were heated to 100°C. The inside surface of the stainless-steel

mixing tank (volume = 0.33m³) is Teflon coated to make it chemically inert. The entire mixing system was well insulated to avoid cold spots that can allow fuel condensation. Before preparing the test mixture, the tank was evacuated to less than 0.05Torr using a turbomolecular pump (Agilent model V301). Approx. 0.5ml of liquid DMMP was injected into the heated tank using a lure lock gas tight syringe. Partial pressures were measured with 100Torr and 10,000Torr full scale range baratrons (MKS Baratron E27D and 628D). A magnetically driven stirrer was used to ensure homogeneity of the mixtures. The mixtures were allowed to mix for at least 2h prior to experiments.

At 100°C, the vapor pressure of DMMP increases to ~50Torr[23]. To minimize fuel condensation, the partial pressure of DMMP was always kept less than 25% of its saturation vapor pressure at respective temperatures. To verify that our mixture is homogenous, we measured absorbance of the test mixture at different pressures in a shock tube using a CO₂ gas laser (Access laser) tuned at 1050.433cm⁻¹. DMMP has a strong and broad absorption feature centered near this wavelength[45]. The measured absorbance was plotted against concentration-pathlength ‘burden’ [mol/m³ * m] as shown in Figure 5-1. The straight line shows that our mixture is homogenous, while the slope of the line gives the absorption cross section [m²/mol] of DMMP at 80°C (temperature, T1 of the shock tube), as calculated using Beer’s law (Eq. 1). Details of the laser diagnostic setup utilizing the CO₂ gas laser to measure OPC concentration is provided in our previous work[4, 51].

$$\alpha_{\nu} = -\ln\left(\frac{I}{I_0}\right)_{\nu} = n_i \sigma_i(\nu, T, P_{tot})L = \sigma_i(\nu, T, P_{tot}) \frac{P_{tot}}{RT} \chi_i L \quad (1)$$

In Eq. 1, α_{ν} is the absorbance at frequency ν ; I and I_0 are the measured intensities of laser power in test gas mixture and in vacuum respectively; n_i [mol/m³] is the concentration of absorbing

species ‘ i ’; σ [m²/mol] is the cross section; P_i [Pa] is the partial pressure of the absorbing species; L [m] is the length of the shock tube; R_u [J/mol-K] is the universal gas constant; T [K] is the temperature; X_i is the mole fraction of absorbing species and P_{tot} [Pa] is the total pressure of the mixture.

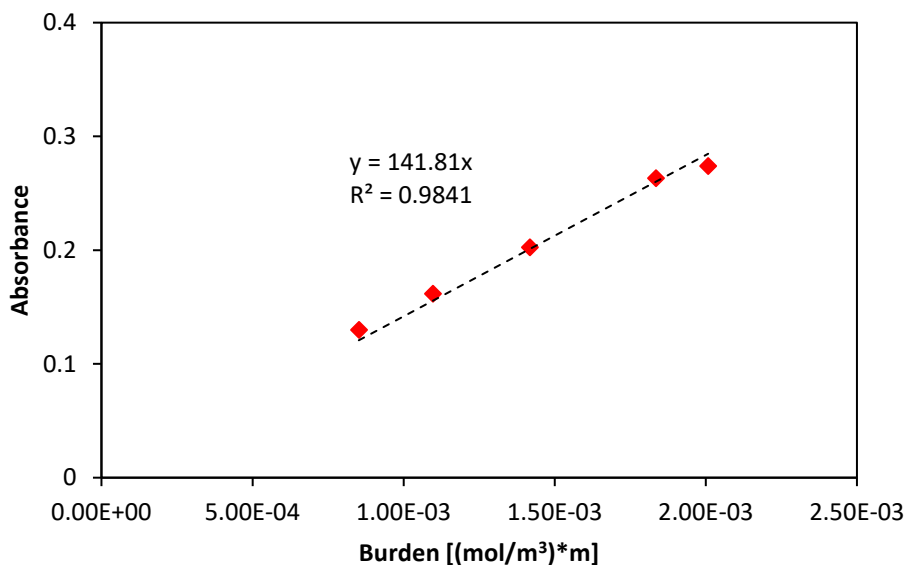


Figure 5-1: Plot of measured absorbance vs concentration-pathlength ‘burden’ of 0.1% DMMP/Ar mixture showing a linear trend

5.2.2 Shock tube experiments

DMMP pyrolysis and oxidation experiments were performed using high purity, stainless steel, and heated shock tube at University of Central Florida. The details of the shock tube can be found in our previous work[5]. The driven section of the shock tube was uniformly heated to 80°C (pre-shock temperature T_1) using custom made heating jackets supplied from Brisk Heat and PID temperature controllers. Ultra-high purity helium (99.999% pure) was used as a driver gas and polycarbonate diaphragms (0.127mm thick), placed between the driven and the driver sections, yielded upon bursting pressures (P_5) of ~1.7atm behind the reflected shock wave. Incident shock

velocities were measured using five piezoelectric pressure transducers (5KHz frequency response) spaced along the last 1.4m of the shock tube and connected to four time-interval counters (Agilent 53220A, 0.1ns time resolution). The measured incident shock velocities were linearly extrapolated to obtain the reflected shock velocity at the end wall. Pressure and temperature behind reflected shock wave (P5 and T5) were calculated using the measured shock velocity and pre-shock temperature and pressure (T1, P1) in normal-shock relations assuming vibrationally equilibrated gases behind both the incident and reflected shocks. Thermochemical data of DMMP for the calculation was taken from Neupane et. al. 2018[51]. Pressure, P5, was also monitored using Kistler 603B1 – a piezoelectric pressure transducer placed in the shock tube side wall at a distance of 2cm from the end-wall.

Before each experiment, the driven section was evacuated to an ultimate pressure of less than $5.0E-5$ Torr using combination of roughing pumps (Agilent DS102) and a turbo molecular pump (Agilent model V301). A rotary vane pump (Agilent DS102) was used to rough the driver section of the shock tube. The shock tube was filled with $P1 = 50-80$ Torr of test mixture to obtain the desired temperature T5 ranging within 1200-1900K. The shock tube configuration and use of driver inserts allowed us to obtain a constant P5 behind the reflection shock region for test times of ~ 2.5 ms. Table 5-1 lists the experimental conditions for DMMP pyrolysis and oxidation carried out in the present work. Uncertainties in T5 and P5 were estimated to be less than 2.0% and 1.5 % respectively. Equivalence ratios (ϕ) for DMMP/O₂/Ar mixtures were determined assuming H₂O, CO₂ and HOPO₂ as products.

Table 5-1: Experiments conditions (Pressures and Temperatures) during pyrolysis and oxidation of DMMP

Pyrolysis		$\phi = 0.23$		$\phi = 0.5$		$\phi = 1$		$\phi = 2$	
P5 [atm]	T5 [K]	P5 [atm]	T5 [K]	P5 [atm]	T5 [K]	P5 [atm]	T5 [K]	P5 [atm]	T5 [K]
1.67	1449	1.66	1335	1.76	1352	1.63	1690	1.59	1686
1.67	1545	1.60	1389	1.80	1370	1.70	1535	1.65	1557
1.66	1619	1.67	1526	1.695	1502	1.88	1452	1.71	1419
				1.587	1681	1.88	1353	1.777	1366

5.2.3 Laser absorption spectroscopy to measure CO concentration

Intermediate CO concentration formed during pyrolysis and oxidation of DMMP were measured using a continuous wave distributed feedback quantum cascade laser (CW-DFB QCL) operating near 4.886 μm to probe the P (23) transition line of CO (Figure 5-2). A 50/50 beam splitter was used to split the laser light into two beams: reference (I_{ref}) and transmitted (I_{tr}). The reference beam was used to monitor laser power fluctuations during the experiments. Transmitted beam was directed through the test section via two sapphire windows. A narrow band pass filter was used downstream of the shock tube to filter out emissions from hot gasses. The beam was then collected in a thermoelectrically cooled MCT (HgCdTe) Vigo Systems PVI-2TE-5.0 photovoltaic detector using a focusing mirror.

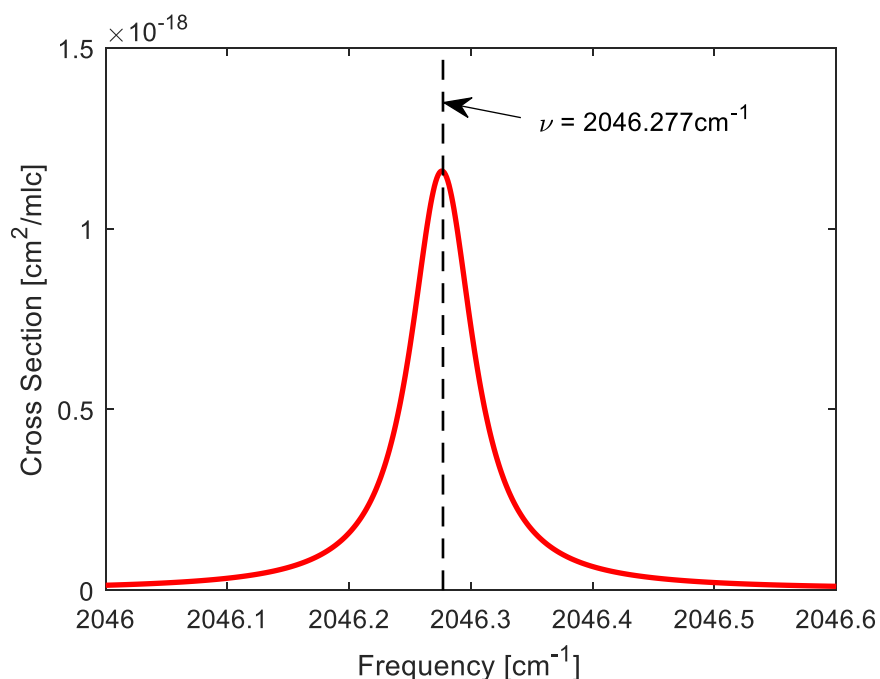


Figure 5-2: Absorption cross section of CO near 4.88 μm and at 1500K and 1.7 atm simulated using HITRAN database[39].

Bristol spectrometer was used to monitor the frequency of the laser beam during the experiment. The Beer-Lambert law (Eq. 1) was used to calculate CO concentration (X_i) from the measured absorbance time-histories. The CO cross section (σ [m^2/mol]) at T_5 and P_5 were modeled using spectroscopic parameters (line broadening and line strength) from HITRAN database[39] assuming self-broadening and fitting a Voigt line shape profile. The CO cross sections at the chosen wavelength and within the temperature and pressure range of our interest were also measured in shock tube experiments performed with pure CO and Ar. The measured values agreed with HITRAN simulation results within $\pm 5\%$.

Experimental pressure traces obtained during pyrolysis and oxidation of DMMP were almost constant (example Figure 5-3) and hence a constant pressure gas dynamic model was used in

Chemkin-Pro for all simulations. Major combustion products formed during the process include hydrocarbons species such as CO, CO₂, CH₄, C₂H₄ and H₂O and small phosphorous species such as HOPO₂, HOPO, CH₃OPO₂ and CH₃PO₂. Within our experiment conditions (T= 1300 – 1700 K and P ≈ 1.7 atm), except for CO, other major combustion products do not have absorption features near 4.9μm, thus allowing for interference free measurement of CO concentration. The uncertainty in measured CO mole fraction is estimated to be 5.5% (due to combined uncertainty in spectroscopic parameters: P5, T5, path length and CO cross section) or ±50ppm (experimental uncertainty due to noise in the measured absorbance signal), whichever is greater.

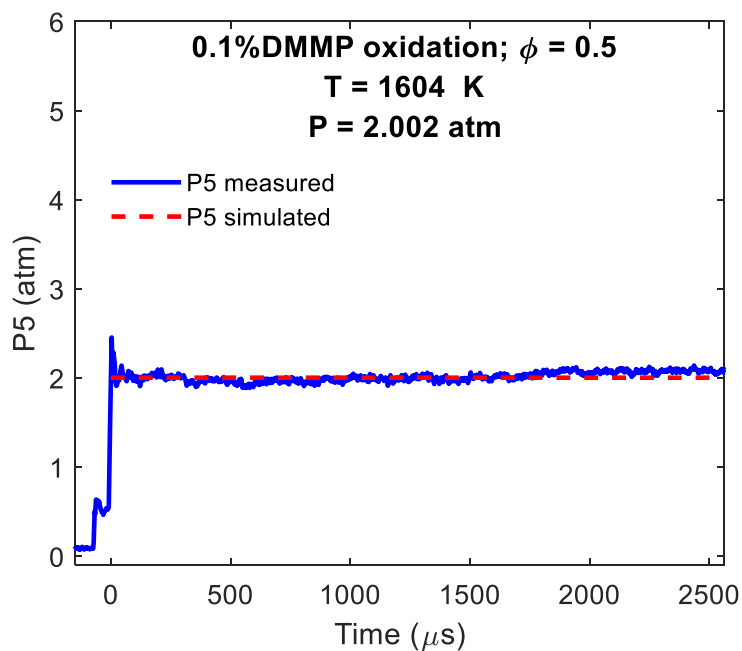


Figure 5-3: Measured pressure, P5 vs simulated pressure in Chemkin-Pro

5.3 Results and discussions

5.3.1 DMMP pyrolysis: CO concentration time-histories

The measured CO concentration time histories during 0.1% DMMP pyrolysis behind reflected shock waves at three temperatures: 1449K, 1545K and 1619K are shown in Figure 5-4. Rate of CO production and the concentration of CO yield at the end of 2.5ms increased with increase in temperature. CO yield at the end of the test time at 2.5ms during pyrolysis of 0.1% DMMP are 0.035%, 0.055% and 0.087% at 1449, 1545 and 1619K respectively. At all three temperatures, there is sharp increase of CO early on during the pyrolysis process after which the rate of production decreases for some time and then finally achieves a steady and slow rate of increase in CO concentration until the end of the test time at ~2.5ms.

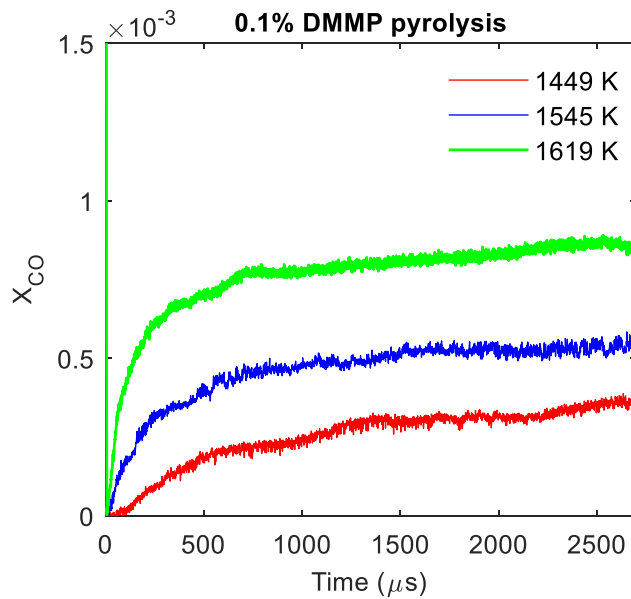
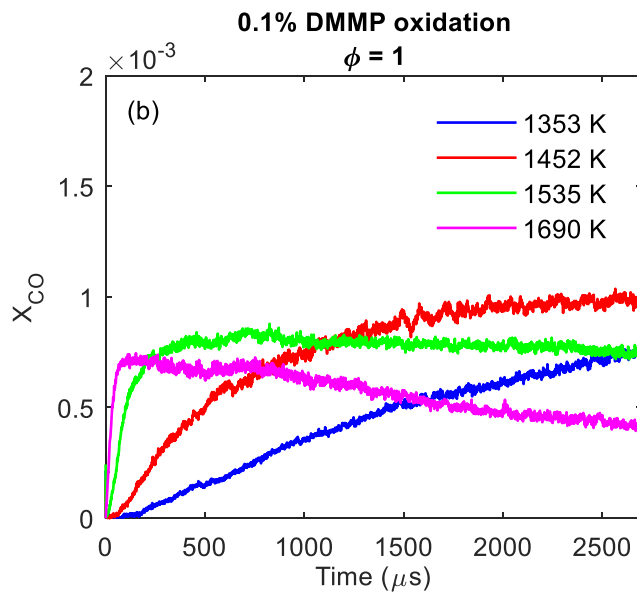
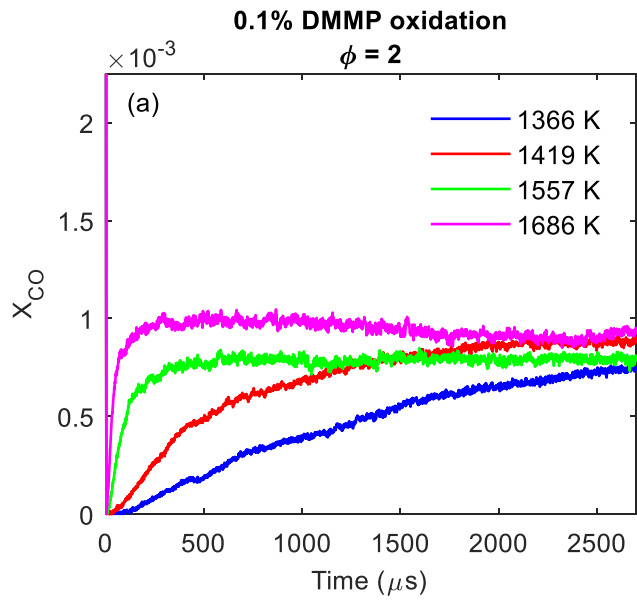


Figure 5-4: CO formed during pyrolysis of 0.1% DMMP at the three temperatures indicated in the figure. $P \sim 1.7$ atm.

5.3.2 DMMP oxidation: CO concentration time-histories

Plots of CO time-histories during DMMP oxidation at different temperatures and equivalence ratios are shown in Figure 5-5 (a – d). For fuel rich ($\Phi=2$, Fig. 5a) DMMP oxidation at lower temperatures (1366 K and 1419 K), CO is still being produced at the end of the shock tube test-time (2.5ms). The rate of formation of CO at these temperatures is higher in the beginning of the oxidation process and then decreases to a slower formation rate after $\sim 500\mu\text{s}$. Similar trends are observed at stoichiometric ($\Phi=1$) and lean conditions ($\Phi=0.5, 0.25$) and at lower temperatures (Figure 5-5b-d). At higher temperatures (Figure 5-5a, 1686K and 1557K), CO forms quickly and reaches a peak value within $500\mu\text{s}$, after which it slightly decreases as CO starts to get consumed. Again, a similar trend is observed at higher temperatures in stoichiometric and lean oxidation of DMMP (Figure 5-5b-d). However, at similar temperatures the rate of consumption of CO after reaching the peak value is faster as the mixture becomes leaner (decreasing equivalence ratio). For example, see 1686K ($\phi = 2$) and 1690K ($\phi = 1$) in Figure 5-5 - a and b, respectively. This can be attributed to higher concentration of O_2 in the mixture which allows for faster conversion of CO into CO_2 .



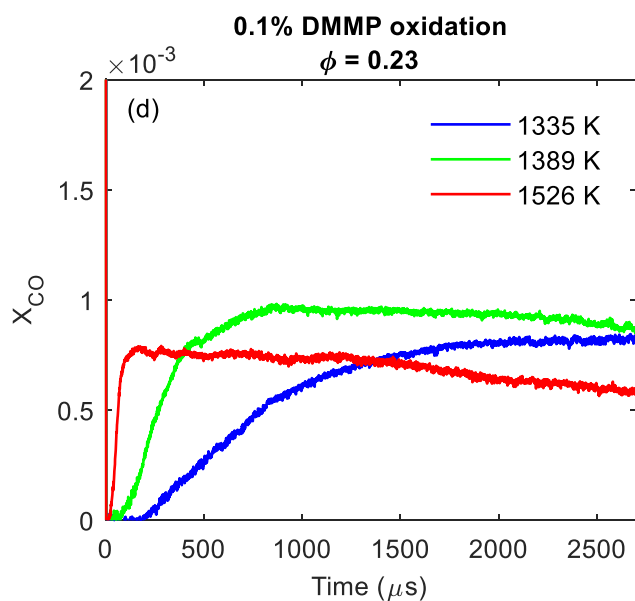
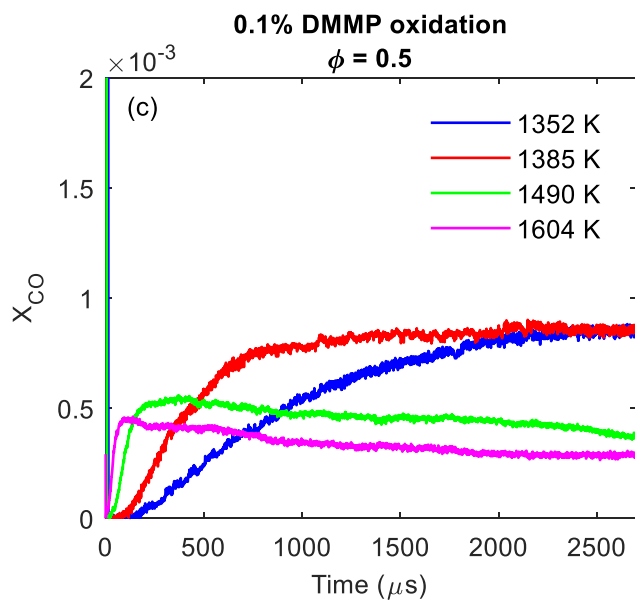


Figure 5-5: CO formed during oxidation of 0.1% DMMP at different equivalence ratios.

5.3.3 Comparison with model predictions

A 0-D closed homogeneous reactor with constant pressure assumption in ANSYS Chemkin Pro software was used to simulate experimental conditions and predict CO yield during pyrolysis

and oxidation of DMMP and was then compared with experimental results. ‘Babushok 2016’ ‘Aramco2.0+LLNL’ mechanisms were used for the kinetic calculations. ‘Aramco2.0+LLNL’ mechanism was put together in our previous study[51] on combustion of tri-ethyl phosphate which is also an organo-phosphorus compound. The model is based on AramcoMech2.0 and LLNL OPC incineration mechanism for phosphorous chemistry. The model also consists of updated thermochemical data of 48 phosphorous containing species (including DMMP and its derivatives) which was based on a recently proposed group values of phosphorous species[41] and theoretical calculations. DMMP and smaller phosphorous reactions in this mechanism are the same as the LLNL incineration mechanism. Babushok 2016 mechanism[30] is based on GriMech3.0 and Jayaweera et al[28] mechanisms along with three additional phosphorous reactions (R6-R8) and was validated using flame speed data of DMMP combustion in lean propane flames.

Figure 5-6 to 5-10 show the comparison of experiment and simulation results using both kinetic models. For high temperature (1619K) pyrolysis case (Fig. 6c), both the models provide a good prediction of CO yield. While at low temperature (1449K) pyrolysis condition (Fig 6a) both the models are underpredicting the initial CO formation rate. For oxidation (Figs 7-10), both the models fail to predict CO yield satisfactorily. In Figure 5-7(a-b), lower temperature (1366K and 1419K) fuel rich oxidation of DMMP, the Aramco2.0+LLNL model provides fair agreement with the experiment data while the CO yield predicted by Babushok mechanism is significantly lower. On the other hand, at 1452 K and $\phi=1$ (Fig. 8b), Babushok mechanism provides better agreement with experiments CO yield. At higher temperature cases ($T>1500\text{K}$) for lean, stoichiometric and rich conditions, both the models are over predicting CO yield as compared to experiment results with Babushok 2016 mechanism being closer to the experiments. From these results of DMMP

oxidation, it can be concluded that Babushok mechanism is likely to underpredict CO yield at lower temperatures (1350-1420K) and over predict at higher temperature (>1502K). Except for low temperature rich conditions (Fig. 7: 1366K and 1419K), Aramco2.0+LLNL mechanism is over predicting CO yield significantly in all oxidation cases.

Note that Babushok mechanism has additional three reactions involving CO and smaller phosphorous species (R6-R8) that are not included in LLNL's phosphorous chemistry. These reactions were added to 'Aramco+LLNL' mechanism, however they did not produce any significant change in the predicted CO yield. It is also clear from the results that both the mechanisms do not sufficiently describe combustion process of DMMP. The reaction rates of major reactions in DMMP breakdown pathways are same in both the mechanisms, so the differences in CO prediction from the two mechanisms can be attributed to a different hydrocarbon chemistry and thermochemistry of phosphorous species.

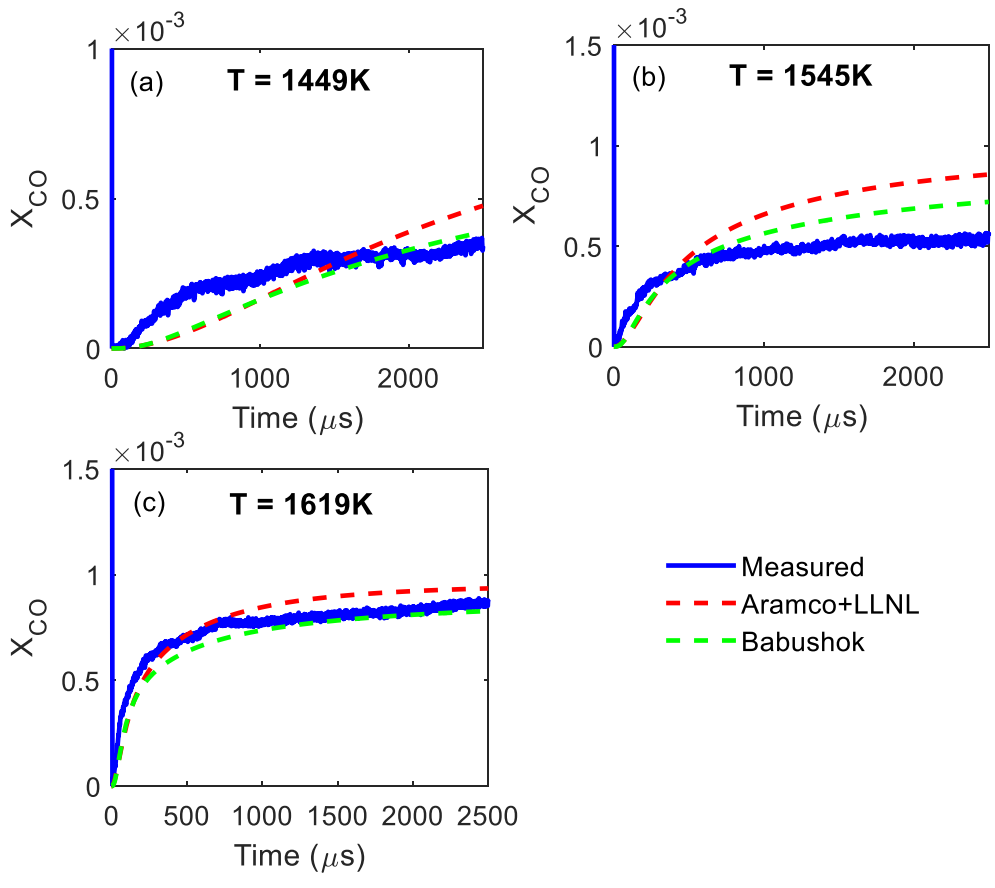


Figure 5-6: Experiments vs. models: CO yield during pyrolysis of 0.1% DMMP pyrolysis

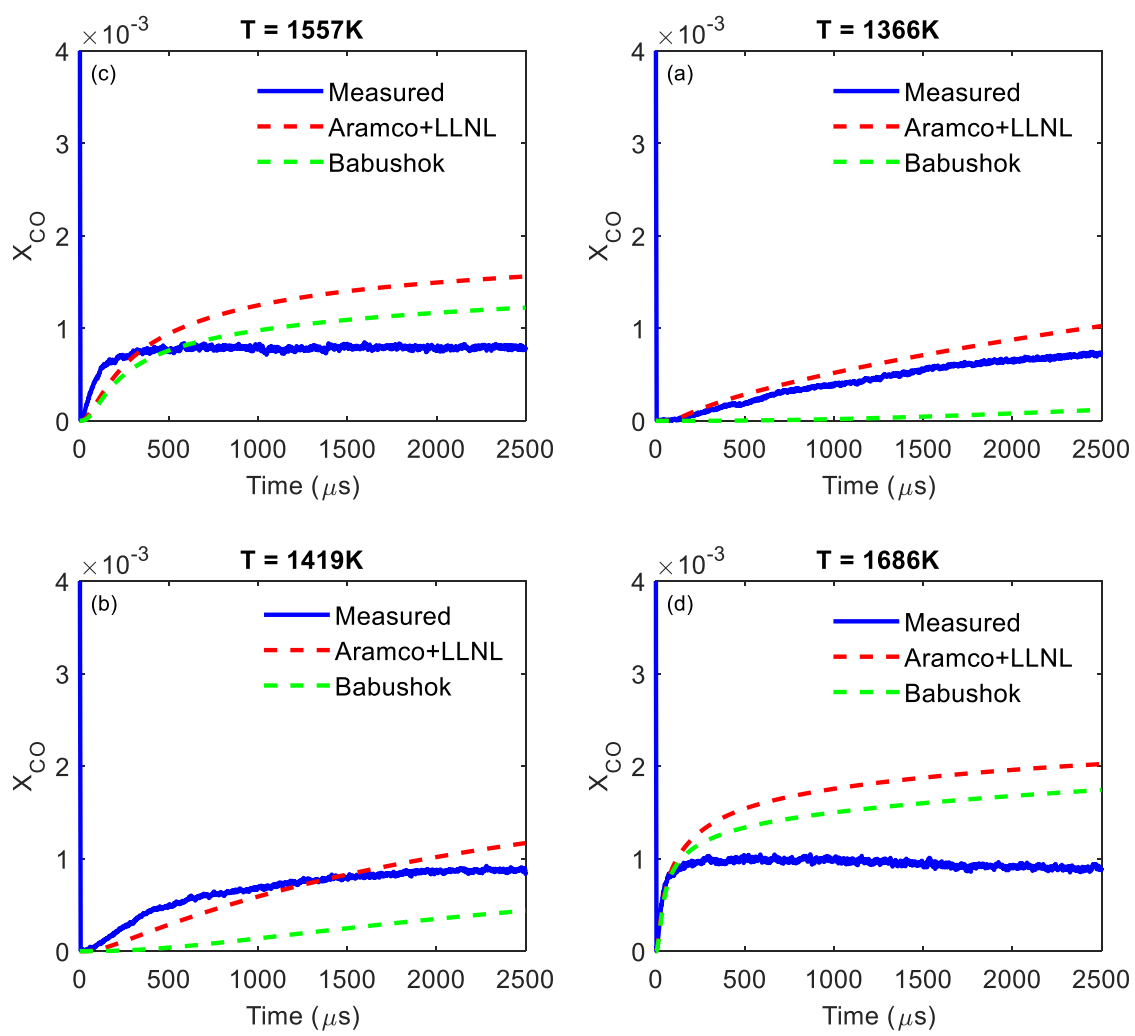


Figure 5-7: Experiments vs. models: CO yield during oxidation of DMMP $\phi=2$

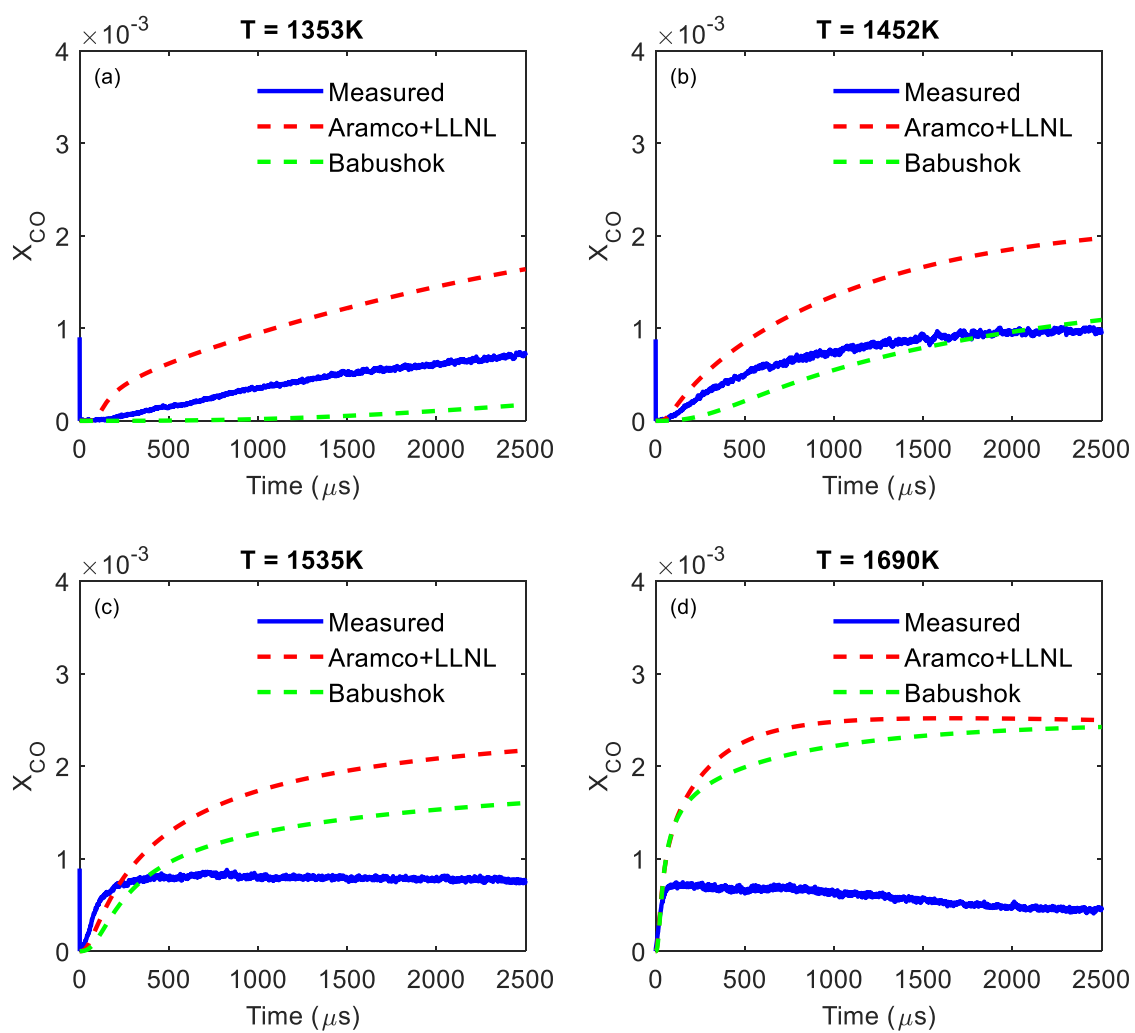


Figure 5-8: Experiments vs. models: CO yield during oxidation of DMMP $\phi=1$

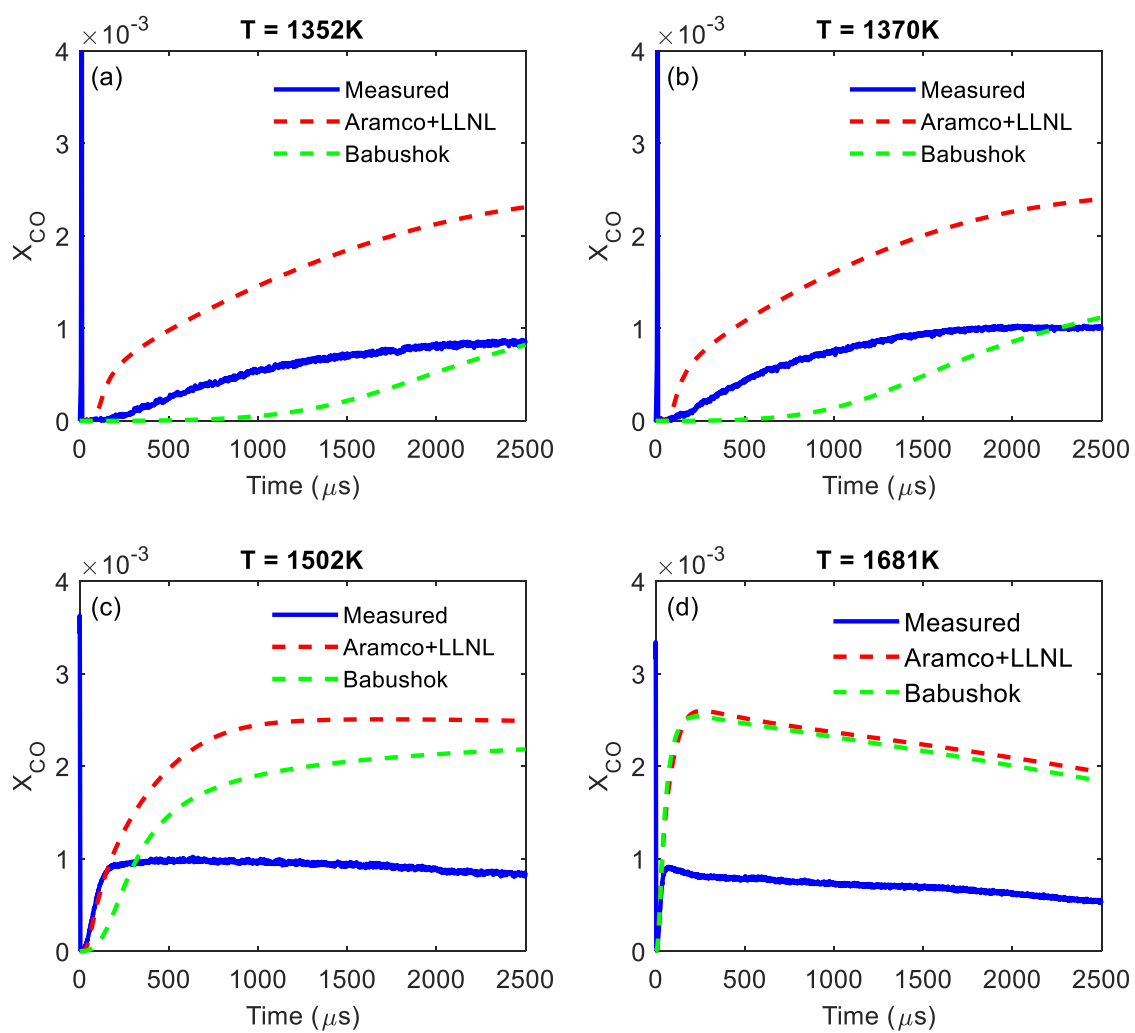


Figure 5-9: Experiments vs. models: CO yield during oxidation of DMMP $\phi=0.5$

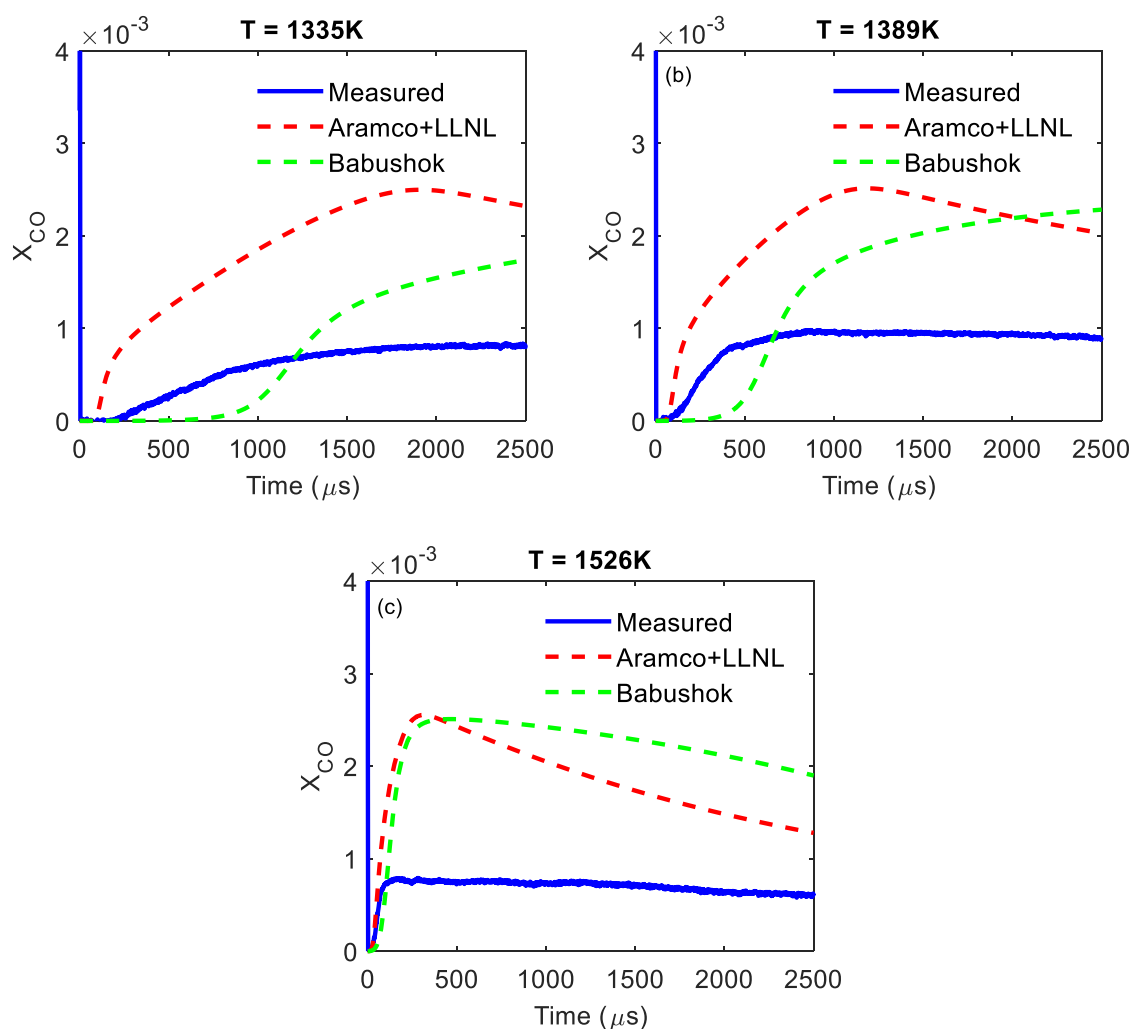


Figure 5-10: Experiments vs. models: CO yield during oxidation of DMMP $\phi=0.23$

5.3.4 Sensitivity and reaction path analysis:

To further understand the performance of kinetic model at different temperatures and equivalence ratios, a detailed sensitivity and rate of production (ROP) analysis were carried out, the results of which are discussed in this section. ‘Aramco+LLNL’ mechanism and ANSYS Chemkin-Pro 0-D closed homogenous constant pressure reactor were used for the analysis. The top 10 sensitive reactions contributing to CO production/consumption during the first 500 μs of

oxidation and pyrolysis of DMMP were identified. The sensitivity coefficient (S) for i^{th} reaction rate (k_i) for a species is defined in Equation 2.

$$S(X_{\text{species}}, k_i, t) = \left(\frac{d X_{\text{species}}(t)}{d k_i} \right) \left(\frac{k_i}{X_{\text{species}}(t)} \right) \quad \text{Eq. 2}$$

Important phosphorous reactions from the results of sensitivity analysis of 0.1% DMMP pyrolysis at 1405K (low temperature case) and 1619K (high temperature case) are shown in Figure 5-11. Solid and dashed lines represent high and low temperature cases, respectively. In both cases, the most sensitive phosphorous reaction is R86. This is a bond fission reaction in which the CH_3 group attached directly to the P atom of DMMP breaks to form CH_3 and $\text{PO}[\text{OME}]_2$ radicals as products. This is the major pathway via which DMMP decomposition takes place during DMMP pyrolysis as shown in DMMP ROP analysis in Figure 5-12. Note that sensitivity of this reaction to CO formation at a high temperature (1619K) quickly peaks and then decreases to attain a negative sensitivity after 200 μs of the pyrolysis reaction. Negative sensitivity coefficient means CO yield decreases with an increase in reaction rate of the reaction. Reactions, R103 and R104 are two pathways of decomposition of the $\text{PO}[\text{OME}]_2$ radical (formed via R86) and have equal but opposite sensitivity coefficients to CO concentration yield. Besides these reactions, reaction R81 was also among the top 10 sensitive reactions, however its sensitivity coefficient quickly peaks and then decreases to zero (not shown in the plot) within 1 μs . Changing the rate of this reaction by up-to one order of magnitude did not affect the predicted CO yield. At 1619K, an additional phosphorous reaction R107 (not shown in the figure) was also among the top 10 sensitive reactions. From these results, it can be concluded that more accurate kinetic parameters of R86 optimized for wide range of temperature can significantly contribute to model improvement in case of DMMP pyrolysis.

$\text{POME[OME]}_2 = \text{CH}_2\text{O} + \text{P[OH]ME[OME]}$	R81
$\text{POME[OME][OCH}_2\text{]} + \text{H} = \text{POME[OME]}_2$	R83
$\text{POME[OME]}_2 = \text{PO[OME]}_2 + \text{CH}_3$	R86
$\text{PO[OME]}_2 = \text{CH}_3\text{OPO}_2 + \text{CH}_3$	R103
$\text{PO[OME]}_2 = \text{CH}_3\text{OPO} + \text{CH}_3\text{O}$	R104
$\text{POME[OME]OCH}_2 = \text{POME[OME]} + \text{CH}_2\text{O}$	R107

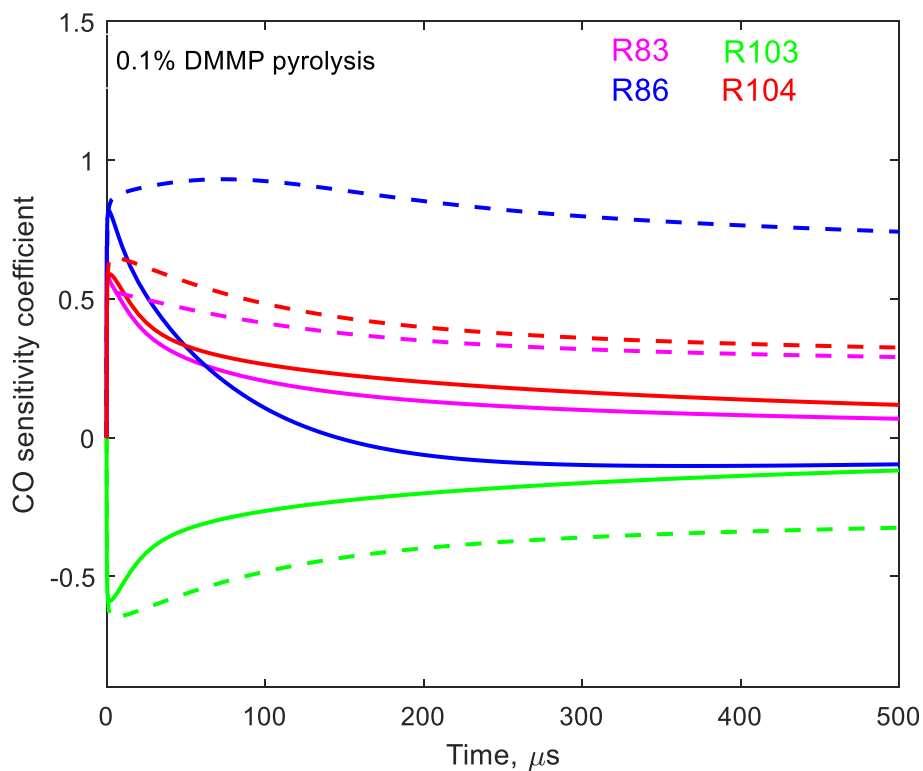


Figure 5-11: Sensitivity analysis on CO concentration yield during 0.1%DMMP pyrolysis 1405K (dashed lines) and 1619K (solid lines) showing top phosphorous reactions

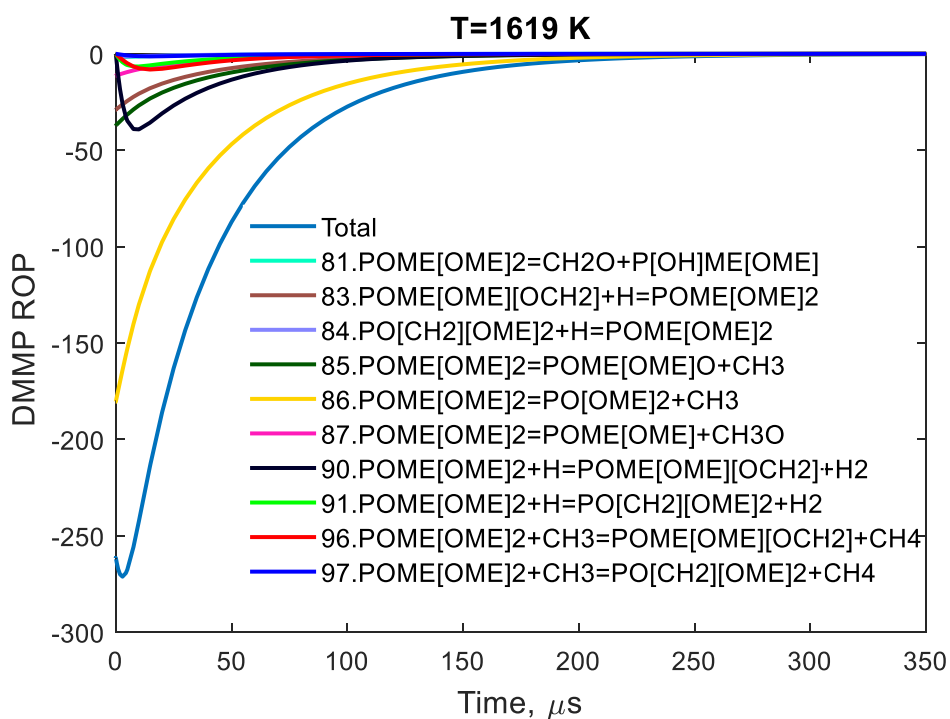


Figure 5-12: ROP analysis on DMMP during its pyrolysis at 1619K

Similarly, sensitivity analysis was carried out for CO yield during DMMP oxidation at $\Phi=0.5$ and $T=1352\text{K}$ (low temperature case) and 1604K (high temperature case) and the results are shown in Figure 5-13. At low temperature (solid lines), H-abstractions reactions of DMMP by O and OH radicals, R92 and R94, show higher sensitivities to CO yield whereas for the high temperature oxidation case, these reactions were not among the top 10 sensitive reactions. Reaction R92 showed maximum sensitivity coefficient for the low temperature oxidation case. Other reactions that were found to be important in oxidation of DMMP are the same as pyrolysis and include reactions R86, R103 and R104. Two additional reactions involving CH_3OPO (R38 and R183) were also among the important reactions for both low and high temperature DMMP

oxidation. Radical recombination reaction, R83, was sensitive only in the high temperature oxidation case.

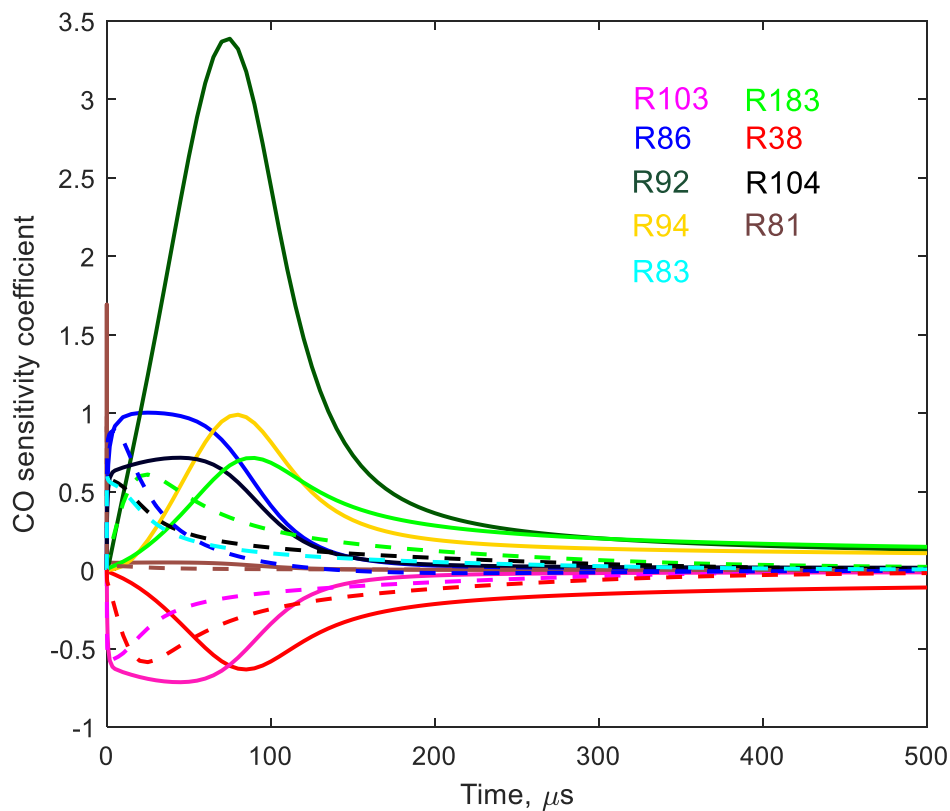


Figure 5-13: Sensitivity analysis on CO concentration yield during 0.1% DMMP oxidation at $\Phi=0.5$ and 1352K (solid lines) and 1604K (dashed lines) showing top phosphorous reactions

For high temperature oxidation case, initial rate of formation of CO agrees well with the experiments (Figs. 7d, 8c-d, 9c-d, 10c). However, the models proceed to overpredict CO yield by up to a factor of 2. Note that the sensitivity result in Figure 5-13 shows the top reaction in the first 500 μ s after the start of oxidation reaction. The sensitivity coefficient of the identified reactions peak and then decrease within the first 200 μ s and after which CO yield has very low sensitivities to these reactions. Thus, additional sensitivity analysis for CO yield during DMMP oxidation at 1602K was carried out to understand reactions that contribute to CO formation/consumption during the latter stage of DMMP oxidation (after 1.5ms). The top 10 reactions are shown in Figure 5-14.

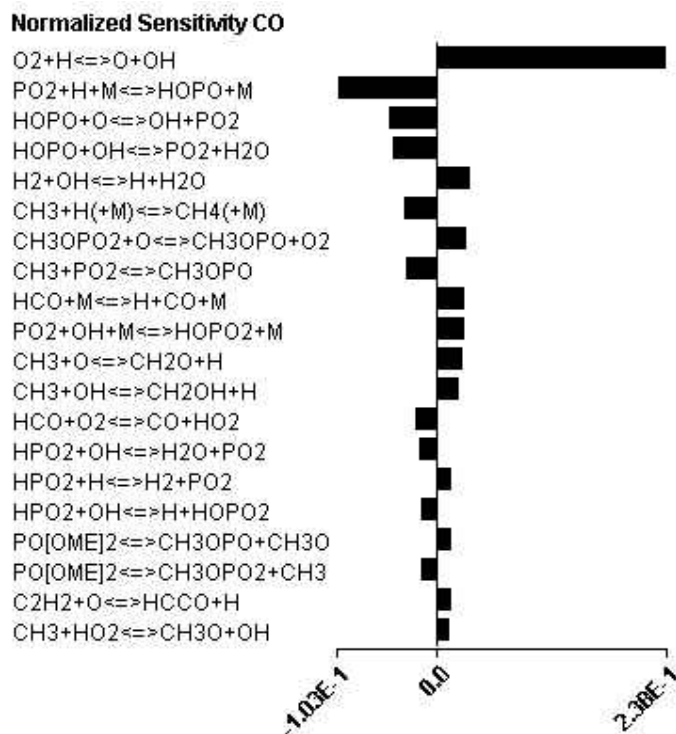


Figure 5-14: Sensitivity analysis on CO concentration yield during 0.1%DMMP oxidation at $\Phi=0.5$ at 1.5ms

During the first 500 μ s, the most sensitive reactions are the initial DMMP decomposition reactions as seen in Fig. 13. The sensitivity analysis result (Fig 14) at 1.5ms after the oxidation reaction (when 100% of DMMP has been consumed), indicates smaller phosphorous reactions R3, R5 and R9 as the most sensitive ones.



Rates of these reactions were increased by an order of magnitude to understand their effect on CO yield. This resulted in a significant decrease in CO yield during oxidation, while their effect on the CO yield during pyrolysis was negligible. Proper optimization of reaction rates of these reactions is suggested for future kinetics study of DMMP oxidation. In addition, further investigation into missing reactions involving hydrocarbon and smaller phosphorous species is also recommended. For low temperature oxidation cases, H-abstraction reactions of DMMP by O and OH (R92 and R94) should be investigated.

5.4 Conclusions

Concentration time histories measurements of CO were performed for DMMP pyrolysis and oxidation at temperatures of 1300-1700K, pressures of 1.5-2.0 atm, and $\Phi=0.25, 0.5, 1$ and 2. Comparisons were made with two kinetic models: Babushok 2016 and Aramco2.0+LLNL model. Babushok mechanism is based on Twarowski[69] and Jayaweera et al[28] phosphorous chemistry and GriMech2.0[71]. Aramco2.0+LLNL mechanism has hydrocarbon chemistry from AramcoMech2.0 and phosphorous chemistry from LLNL's OPC incineration mechanism along with recently updated thermochemical data of phosphorous species. Both models exhibited fair agreement for the high temperature pyrolysis (1619K) case. For low temperature pyrolysis

(1445K), both the models underpredicted the rate of CO production. For oxidation, performance of both models were not satisfactory in terms of CO prediction. At high temperatures (>1500K), the models overpredicted CO yield significantly. At low temperatures (1330-1420K), Babushok model underpredicted CO yield and formation rates while LLNL+Aramco model exhibited fair agreement at rich conditions. Sensitivity analysis indicates that for low temperature oxidation (1300-1450 K), accurate rate parameter of H-abstraction reactions of DMMP by O and OH radicals (R92 and R94) are needed for accurate prediction of CO yield. For higher temperature oxidation cases, reaction of smaller phosphorous species PO_2 and HOPO with H and OH radicals should be investigated along with addition of reaction pathways involving reactions of hydrocarbons with phosphorous species. Further experiments targeting phosphorous species such as PO_2 and HOPO will provide an important validation target for the DMMP oxidation mechanism. Lower temperature predictions of CO concentration during DMMP pyrolysis could be improved by high level theoretical calculations or direct experimental measurements of rate of reaction R86 which involves bond fission of DMMP to form $\text{PO}[\text{OME}]_2$ and CH_3 radicals.

CHAPTER 6: SUMMARY

The main objective of this dissertation is to develop improved kinetic model of organo phosphorous simulants and this goal has been achieved via various experimental and computational studies. First, absorption cross sections of five organo phosphorous simulants were measured in mid IR region ($650 - 3500 \text{ cm}^{-1}$) using FTIR. To the best of our knowledge, this is the first quantitative absorption spectra of OPC compounds reported in literature. The IR lines were concentrated in regions $650 - 1500 \text{ cm}^{-1}$ and $2800 - 3100 \text{ cm}^{-1}$ (low and high frequency regions). The most prominent line was located within $995.1 - 1058.7 \text{ cm}^{-1}$ and the peak cross section varied from $83.5 \text{ m}^2/\text{mol}$ (DEMP) to $343.15 \text{ m}^2/\text{mol}$ (TEP). Lines in high frequency region were relatively weaker. The cross section and lines position data reported here are critical in development of quantitative absorption diagnostic schemes for detection of CW simulants during combustion.

This study also provides the first CO time histories measured using laser absorption spectroscopy during pyrolysis and oxidation of two chemical warfare simulants – tri-ethyl phosphate (TEP) and dimethyl methyl phosphonate (DMMP) behind reflected shock waves. New improved model for TEP was proposed in the current study which uses $\text{C}_0\text{-C}_2$ hydrocarbon chemistry from AramcoMech2.0 and phosphorous chemistry from the LLNL mechanism, along with updated thermochemical data from current work for phosphorous containing species. In addition, reaction rates of seven molecular elimination reactions in TEP sub-mechanism were updated using CBS-QB3 quantum chemical theory level. Alternative TEP decomposition pathway via H-abstraction, radical decomposition and recombination reactions are added. The predicted CO yield during TEP pyrolysis and oxidation using improved kinetic model is much better, Reaction path and rate of production analyses revealed that the H-abstraction pathway plays an

important role only at low temperatures while at high temperatures (>1200K), the molecular elimination pathway remains predominant. The molecular elimination reactions are very fast compared to any H-abstraction reactions at high temperature, hence most to the TEP decomposition proceeds via this pathway. The newly calculated reactions rates, discussions on results of sensitivity and reaction path analysis critical in development of more comprehensive detailed mechanism for TEP combustion.

For DMMP, comparisons of experiments results were made with two kinetic models: Babushok 2016 and Aramco2.0+LLNL model. Babushok mechanism is based on Twarowski [69] and Jayaweera et al [28] phosphorous chemistry and GriMech2.0 [71]. Aramco2.0+LLNL mechanism has hydrocarbon chemistry from AramcoMech2.0 and phosphorous chemistry from LLNL's OPC incineration mechanism along with recently updated thermochemical data of phosphorous species. Both models exhibited fair agreement for high temperature pyrolysis (1619 K) case. For low temperature pyrolysis (1445 K), both the models underpredicted rate of CO production. For oxidation, performance of both the models were not satisfactory in terms of CO prediction. Sensitivity analysis revealed that for low temperature oxidation (1300-1450K), accurate rate parameter of H-abstraction reactions of DMMP by O and OH radicals are needed for accurate prediction of CO yield. For higher temperature oxidation cases, reaction of smaller phosphorous species PO_2 and HOPO with H and OH radicals should be investigated along with addition of reaction pathways involving reactions of hydrocarbons with phosphorous species.

Future work on simulants chemical kinetics study should involve targeting new phosphorous species such as PO_2 and HOPO in shock tube experiments. This will provide important validation target for both DMMP and TEP oxidation mechanisms. In addition,

experiments characterizing effects of environmental variable (CO_2 , H_2O , NO_x) on chemical kinetics of these compounds will provide important information relevant to real word scenarios of agent defeat operations. Further experiments covering wider range of pressures, equivalence ratios and OPCs will be useful for model validation and improvement.

APPENDIX A

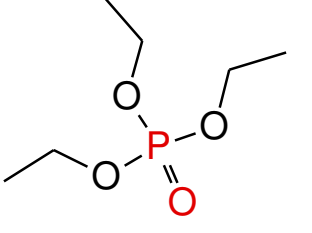
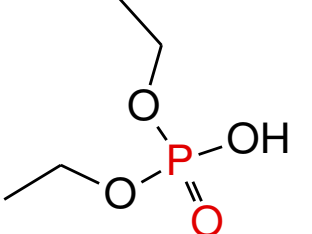
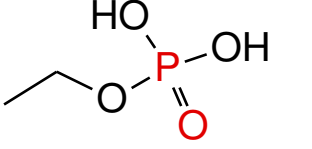
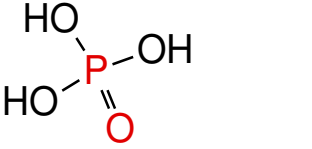
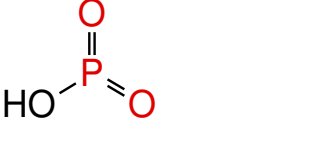
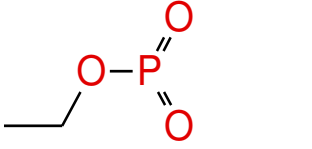
THERMODYNAMIC PROPERTIES OF PHOSPHOROUS SPECIES FROM CBS-QB3 CALCULATION

Species	ΔH_f kcal.mol ⁻¹	S cal.mol ⁻¹ .K ⁻¹	Cp cal/mol.K						
			300K	400K	500K	600K	800K	1000K	1500K
po[h][oh]	-60.17	63.96	9.24	10.82	12.09	13.08	14.53	15.57	17.24
po[oh]2	-154.98	70.66	14.72	17.15	18.87	20.08	21.68	22.75	24.54
ch3po2	-118.09	74.74	15.05	17.90	20.35	22.39	25.48	27.70	31.09
po[oh]me	-106.07	74.72	18.08	21.48	24.23	26.41	29.66	32.04	35.86
po[oh][ome]	-152.49	82.47	21.04	24.75	27.89	30.46	34.31	37.07	41.36
po[oh]meo	-155.51	78.57	21.46	25.62	28.87	31.38	35.02	37.60	41.64
p[oh]me[ome]	-124.53	83.41	24.93	30.15	34.64	38.38	44.18	48.49	55.38
pome[ome]	-100.77	84.43	22.73	27.33	31.46	34.95	40.41	44.44	50.74
po[ome]2	-146.99	92.39	25.57	30.57	35.14	39.03	45.09	49.50	56.25
pome[ome]o	-150.76	90.06	26.32	31.62	36.21	40.00	45.80	50.01	56.50
po[ome]2o	-199.01	95.26	29.09	34.74	39.75	43.96	50.38	55.00	61.98
p[oh]3	-185.51	73.73	18.90	21.95	24.05	25.52	27.43	28.76	31.12
p[oh]2[ome]	-179.72	82.53	23.50	27.76	31.25	34.03	38.16	41.17	46.02
DMMP (this study)	-206.79	97.771	32.563	39.567	45.922	51.349	59.85	66.118	75.832
DMMP (Khalifa et. al. 2015)*	-204.55	99.98	34.21	40.87	46.92	52.02	59.84	65.51	74.23

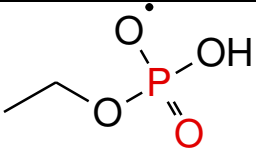
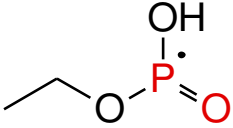
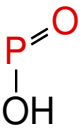
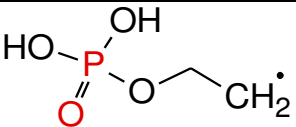
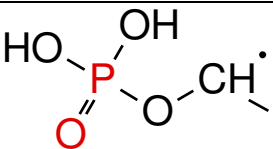
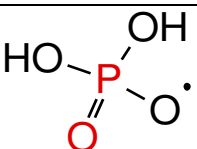
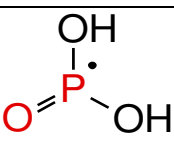
*A. Khalifa, M. Ferrari, R. Fournet, B. Sirjean, L. Verdier, P. Glaude, The Journal of Physical Chemistry A, 119 (2015)

APPENDIX B

SPECIES DICTIONARY

Species name	Structure
PO[OET]3 (TEP)	
PO[OH][OET]2	
PO[OH]2[OET]	
PO[OH]3	
HOPO2	
C2H5OPO2	

PO[OET]2[OsC2H4]	
PO[OET]2[OpC2H4]	
PO[OET]2O	
PO[OET]2	
pDEP	
sDEP	

PO[OH][OET]O	
PO[OH][OET]	
HOPO	
PO[OH]2[OpC2H4]	
PO[OH]2[OsC2H4]	
PO[OH]2O	
PO[OH]2	

LIST OF REFERENCES

1. Gann, R.G.J.F.t., *Guidance for advanced fire suppression in aircraft*. 2008. **44**(3): p. 263-282.
2. Bouvet, N., et al., *A comparison of the gas-phase fire retardant action of DMMP and Br₂ in co-flow diffusion flame extinguishment*. *Combustion and Flame*, 2016. **169**: p. 340-348.
3. Denison, M.K., et al., *Detailed computational modeling of military incinerators*. 2001, REACTION ENGINEERING INTERNATIONAL SALT LAKE CITY UT.
4. Loparo, Z.E., et al. *Time-Resolved Measurements of Intermediate Concentrations in Fuel-Rich n-Heptane Oxidation Behind Reflected Shock Waves*. in *ASME Turbo Expo 2017: Turbomachinery Technical Conference and Exposition*. 2017. American Society of Mechanical Engineers.
5. Koroglu, B., et al., *Shock tube ignition delay times and methane time-histories measurements during excess CO₂ diluted oxy-methane combustion*. *Combustion and flame*, 2016. **164**: p. 152-163.
6. Ren, W., D.F. Davidson, and R.K. Hanson, *IR laser absorption diagnostic for C₂H₄ in shock tube kinetics studies*. *International Journal of Chemical Kinetics*, 2012. **44**(6): p. 423-432.
7. Rusu, C.N. and J.T. Yates, *Adsorption and decomposition of dimethyl methylphosphonate on TiO₂*. *The Journal of Physical Chemistry B*, 2000. **104**(51): p. 12292-12298.
8. Mitchell, M.B., V. Sheinker, and E.A. Mintz, *Adsorption and decomposition of dimethyl methylphosphonate on metal oxides*. *The Journal of Physical Chemistry B*, 1997. **101**(51): p. 11192-11203.
9. Kim, C.S., R.J. Lad, and C.P. Tripp, *Interaction of organophosphorous compounds with TiO₂ and WO₃ surfaces probed by vibrational spectroscopy*. *Sensors and Actuators B: Chemical*, 2001. **76**(1): p. 442-448.
10. Mawhinney, D.B., et al., *Adsorption studies by transmission IR spectroscopy: a new method for opaque materials*. *Langmuir*, 1999. **15**(13): p. 4617-4621.
11. Pyun, S.H., et al., *Interference-free mid-IR laser absorption detection of methane*. *Measurement Science and Technology*, 2011. **22**(2): p. 025303.
12. Sharpe, S.W., et al., *Gas-phase databases for quantitative infrared spectroscopy*. *Applied spectroscopy*, 2004. **58**(12): p. 1452-1461.

13. Smirnova, I., et al., *Gas-phase synchrotron FTIR spectroscopy of weakly volatile alkyl phosphonate and alkyl phosphate compounds: vibrational and conformational analysis in the terahertz/far-IR spectral domain*. The Journal of Physical Chemistry B, 2010. **114**(50): p. 16936-16947.
14. Cuisset, A., et al., *Gas-phase vibrational spectroscopy and ab initio study of organophosphorous compounds: Discrimination between species and conformers*. The Journal of Physical Chemistry B, 2008. **112**(39): p. 12516-12525.
15. Reva, I., A. Simão, and R. Fausto, *Conformational properties of trimethyl phosphate monomer*. Chemical physics letters, 2005. **406**(1): p. 126-136.
16. Mäkie, P., et al., *Adsorption of Trimethyl Phosphate on Maghemite, Hematite, and Goethite Nanoparticles*. The Journal of Physical Chemistry A, 2011. **115**(32): p. 8948-8959.
17. Mott, A.J. and P. Rez, *Calculated infrared spectra of nerve agents and simulants*. Spectrochim Acta A Mol Biomol Spectrosc, 2012. **91**: p. 256-60.
18. Wilmsmeyer, A.R., et al., *Infrared Spectra and Binding Energies of Chemical Warfare Nerve Agent Simulants on the Surface of Amorphous Silica*. The Journal of Physical Chemistry C, 2013. **117**(30): p. 15685-15697.
19. Phillips, M.C., M.S. Taubman, and J. Kriesel. *Use of external cavity quantum cascade laser compliance voltage in real-time trace gas sensing of multiple chemicals*. in *Quantum Sensing and Nanophotonic Devices XII*. 2015. International Society for Optics and Photonics.
20. Köroğlu, B., et al., *Measurements of Propionaldehyde Infrared Cross-Sections and Band Strengths*. Journal of Quantitative Spectroscopy and Radiative Transfer, 2015. **152**: p. 107-113.
21. Smith, B.C., *Fundamentals of Fourier transform infrared spectroscopy*. 2011: CRC press.
22. TRCVP, *Vapor Pressure Database, Version 2.2P* T.A.M.U. Thermodynamic Research Center, College Station, TX, Editor.
23. Butrow, A.B., J.H. Buchanan, and D.E. Tevault, *Vapor pressure of organophosphorus nerve agent simulant compounds*. Journal of Chemical & Engineering Data, 2009. **54**(6): p. 1876-1883.
24. Brozena, A., et al., *Vapor pressure of triethyl and tri-n-propyl phosphates and diethyl malonate*. Journal of Chemical & Engineering Data, 2014. **59**(8): p. 2649-2659.
25. Sharpe, S.W., et al. *Quantitative infrared spectra of vapor phase chemical agents*. in *Chemical and Biological Sensing IV*. 2003. International Society for Optics and Photonics.

26. Shmakov, A.G., et al., *Effect of CO₂ addition on the structure of premixed fuel-rich CH₄/O₂/N₂ and C₃H₈/O₂/N₂ flames stabilized on a flat burner at atmospheric pressure.* Energy & Fuels, 2016. **30**(3): p. 2395-2406.
27. Korobeinichev, O.P., et al., *Flame inhibition by phosphorus-containing compounds in lean and rich propane flames.* Proceedings of the Combustion Institute, 2005. **30**(2): p. 2353-2360.
28. Jayaweera, T.M., et al., *Flame inhibition by phosphorus-containing compounds over a range of equivalence ratios.* Combustion and Flame, 2005. **140**(1): p. 103-115.
29. Korobeinichev, O.P., et al., *Mechanism of inhibition of hydrogen/oxygen flames of various compositions by trimethyl phosphite.* Kinetics and Catalysis, 2010. **51**(2): p. 154-161.
30. Babushok, V.I., et al., *Influence of hydrocarbon moiety of DMMP on flame propagation in lean mixtures.* Combustion and Flame, 2016. **171**: p. 168-172.
31. Zegers, E. and E. Fisher, *Gas-phase pyrolysis of diethyl methylphosphonate.* Combustion science and technology, 1996. **116**(1-6): p. 69-89.
32. Zegers, E.J.P. and E.M. Fisher, *Gas-Phase Pyrolysis of Diisopropyl Methylphosphonate.* Combustion and Flame, 1998. **115**(1-2): p. 230-240.
33. Zegers, E. and E. Fisher, *Pyrolysis of triethyl phosphite.* Combustion science and technology, 1998. **138**(1-6): p. 85-103.
34. Glaude, P., et al., *Detailed chemical kinetic reaction mechanisms for incineration of organophosphorus and fluoroorganophosphorus compounds.* Proceedings of the Combustion Institute, 2002. **29**(2): p. 2469-2476.
35. Glaude, P., et al., *Kinetic study of the combustion of organophosphorus compounds.* Proceedings of the Combustion Institute, 2000. **28**(2): p. 1749-1756.
36. Aly, Y., D. Dalton, and S. Peiris, *2015 Chemical-Agent Simulants Workshop Report.* 2016, Defense Threat Reduction Agency Fort Belvoir, United States.
37. ANSYS Chemkin-Pro. 2017, <http://www.ansys.com/products/fluids/ansys-chemkin-pro>: San Diego, CA.
38. Li, Y., et al., *The oxidation of 2-butene: A high pressure ignition delay, kinetic modeling study and reactivity comparison with isobutene and 1-butene.* Proceedings of the Combustion Institute, 2017. **36**(1): p. 403-411.
39. Gordon, I.E., et al., *The HITRAN2016 molecular spectroscopic database.* Journal of Quantitative Spectroscopy and Radiative Transfer, 2017. **203**(Supplement C): p. 3-69.

40. Ritter, E.R., *THERM: A computer code for estimating thermodynamic properties for species important to combustion and reaction modeling*. Journal of chemical information and computer sciences, 1991. **31**(3): p. 400-408.
41. Khalifa, A., et al., *Quantum chemical study of the thermochemical properties of organophosphorous compounds*. The Journal of Physical Chemistry A, 2015. **119**(42): p. 10527-10539.
42. Benson, S.W., *Thermochemical kinetics*. 1976: Wiley.
43. Hahn, D.K., K.S. Raghuveer, and J.V. Ortiz, *Computational Tests of Models for Kinetic Parameters of Unimolecular Reactions of Organophosphorus and Organosulfur Compounds*. The Journal of Physical Chemistry A, 2011. **115**(49): p. 14143-14152.
44. O'Neal, H. and S. Benson, *A Method for estimating the Arrhenius A factors for four- and six-center unimolecular reactions*. The Journal of Physical Chemistry, 1967. **71**(9): p. 2903-2921.
45. Neupane, S., R. Peale, and S. Vasu, *Infrared absorption cross sections of several organophosphorous chemical-weapon simulants*. Journal of Molecular Spectroscopy, 2019. **355**: p. 59-65.
46. Neupane, S., et al. *MHz-Rate Measurements of Time-Resolved Species Concentrations in Shock Heated Chemical Weapon Simulants*. in *2018 IEEE Research and Applications of Photonics In Defense Conference (RAPID)*. 2018.
47. Korobeinichev, O.P., et al., *The chemistry of the destruction of organophosphorus compounds in flames - III: The destruction of DMMP and TMP in a flame of hydrogen and oxygen*. Combustion and Flame, 2000. **121**(4): p. 593-609.
48. Korobeinichev, O.P., A.A. Chernov, and T.A. Bolshova, *The chemistry of the destruction of organophosphorus compounds in flames—IV: destruction of DIMP in a flame of H₂ + O₂ + Ar*. Combustion and Flame, 2000. **123**(3): p. 412-420.
49. Korobeinichev, O.P., V.M. Shvartsberg, and A.A. Chernov, *The destruction chemistry of organophosphorus compounds in flames—II: structure of a hydrogen–oxygen flame doped with trimethyl phosphate*. Combustion and Flame, 1999. **118**(4): p. 727-732.
50. Korobeinichev, O.P., et al., *The destruction chemistry of organophosphorus compounds in flames—I: quantitative determination of final phosphorus-containing species in hydrogen-oxygen flames*. Combustion and Flame, 1999. **118**(4): p. 718-726.
51. Neupane, S., et al., *Shock Tube/Laser Absorption and Kinetic Modeling Study of Triethyl Phosphate Combustion*. The Journal of Physical Chemistry A, 2018. **122**(15): p. 3829-3836.

52. Zhou, C.-W., et al., *An experimental and chemical kinetic modeling study of 1,3-butadiene combustion: Ignition delay time and laminar flame speed measurements*. Combustion and Flame, 2018. **197**: p. 423-438.
53. Zegers, E.J.P. and E.M. Fisher, *Pyrolysis of Triethyl Phosphate*. Combustion Science and Technology, 1998. **138**(1-6): p. 85-103.
54. Zegers, E.J.P. and E.M. Fisher, *Gas-Phase Pyrolysis of Diethyl Methylphosphonate*. Combustion Science and Technology, 1996. **116-117**(1-6): p. 69-89.
55. Glaude, P.A., et al., *Detailed chemical kinetic reaction mechanisms for incineration of organophosphorus and fluoroorganophosphorus compounds*. Proceedings of the Combustion Institute, 2002. **29**(2): p. 2469-2476.
56. Frisch, M.J.T., G. W.; Schlegel, H. B.; Scuseria, G. E.; Robb, M. A.; Cheeseman, J. R.; Scalmani, G.; Barone, V.; Mennucci, B.; Petersson, G. A.; et al. , *Gaussian 09, Rev. D.01*. 2009, Gaussian, Inc.: Wallingford CT.
57. Montgomery, J.A., et al., *A complete basis set model chemistry. VI. Use of density functional geometries and frequencies*. Journal of Chemical Physics, 1999. **110**(6): p. 2822-2827.
58. Gonzalez, C. and H.B. Schlegel, *AN IMPROVED ALGORITHM FOR REACTION-PATH FOLLOWING*. Journal of Chemical Physics, 1989. **90**(4): p. 2154-2161.
59. S. Sharma, G.R.M., R. West, M. R. Harper, C. F. Goldsmith, J. W. Allen and W. H. Green, *CanTherm v1.0 opensource software package*. 2010.
60. Petersson, G.A., et al., *Calibration and comparison of the Gaussian-2, complete basis set, and density functional methods for computational thermochemistry*. The Journal of chemical physics, 1998. **109**(24): p. 10570-10579.
61. Eckart, C., *The penetration of a potential barrier by electrons*. Physical Review, 1930. **35**(11): p. 1303.
62. Neupane, S., et al., *Theoretical Calculation of Reaction Rates and Combustion Kinetic Modeling Study of Tri-Ethyl Phosphate (TEP)*. 2019.
63. Dean, A.M. and J.W. Bozzelli, *Combustion chemistry of nitrogen*, in *Gas-phase combustion chemistry*. 2000, Springer. p. 125-341.
64. Rahman, K.A., et al., *Femtosecond, two-photon, laser-induced fluorescence (TP-LIF) measurement of CO in high-pressure flames*. 2018. **57**(20): p. 5666-5671.

65. Mathieu, O., W. Kulatilaka, and E. Petersen, *Shock-tube studies of Sarin surrogates*. Shock Waves, 2018: p. 1-9.
66. Bouvet, N., et al., *Experimental and numerical investigation of the gas-phase effectiveness of phosphorus compounds*. Fire and Materials, 2016. **40**(5): p. 683-696.
67. Korobeinichev, O.P., et al. *Experimental Study And Modeling Of Inhibition Effect Of Dimethyl Methylphosphonate On Burning Velocity Of Stoichiometric Propane/Air Mixtures At Atmospheric Pressure*. in *Proceedings of The Fourth Asia-Pacific Conference on Combustion*. 2003.
68. Korobeinichev, O.P., V.M. Shvartsberg, and A.G. Shmakov, *The chemistry of combustion of organophosphorus compounds*. Russian Chemical Reviews, 2007. **76**(11): p. 1094.
69. Twarowski, A.J.C. and flame, *The influence of phosphorus oxides and acids on the rate of H+ OH recombination*. 1993. **94**(1-2): p. 91-107.
70. Werner, J.H. and T.A. Cool, *Kinetic model for the decomposition of DMMP in a hydrogen/oxygen flame*. Combustion and Flame, 1999. **117**(1-2): p. 78-98.
71. Smith, G., et al., *GRI-Mech 3.0, 2000*.
72. Glaude, P.A., et al., *Kinetic study of the combustion of organophosphorus compounds*. Proceedings of the Combustion Institute, 2000. **28**: p. 1749-1756.
73. Mathieu, O., et al., *Experimental and modeling study on the effects of dimethyl methylphosphonate (DMMP) addition on H₂, CH₄, and C₂H₄ ignition*. 2018. **191**: p. 320-334.